METHANE AND CARBON DIOXIDE ADSORPTION ON Al-BASED AND Zr-BASED MOFs: EFFECTS OF AMINO-FUNCTIONALIZATION

Orawee Lamoonkit

A Thesis Submitted in Partial Fulfilment of the Requirements
for the Degree of Master of Science
The Petroleum and Petrochemical College, Chulalongkorn University
in Academic Partnership with
The University of Michigan, The University of Oklahoma,
Case Western Reserve University, and Institut Français du Pétrole
2018

บทคัดย่อและแฟ้มข้อมูลฉบับเต็มของวิทยานิพนธ์ตั้งแต่ปีการศึกษา 2554 ที่ให้บริการในคลังปัญญาจุฬาฯ (CUIR)
เป็นแฟ้มข้อมูลของนิสิตเจ้าของวิทยานิพนธ์ที่ส่งผ่านทางบัณฑิตวิทยาลัย
The abstract and full text of theses from the academic year 2011 in Chulalongkorn University Intellectual Repository(CUIR)
are the thesis authors' files submitted through the Graduate School.

Thesis Title:	Methane and Carbon Dioxide Adsorption on Al-based and Zr-based MOFs: Effects of Amino-Functionalization
By:	Orawee Lamoonkit
Program:	Petrochemical Technology
Thesis Advisors:	Prof. Pramoch Rangsunvigit
	Dr. Santi Kulpratipunja
	Prof. Boonyarach Kitiyanan
	Dr. Chalita Ratanatawanate

Accepted by The Petroleum and Petrochemical College, Chulalongkorn University, in partial fulfilment of the requirements for the Degree of Master of Science.

..... College Dean
(Prof. Suwabun Chirachanchai)

Thesis Committee:

.....	.....
(Prof. Pramoch Rangsunvigit)	(Dr. Santi Kulpratipunja)
.....	.....
(Prof. Boonyarach Kitiyanan)	(Dr. Chalita Ratanatawanate)
.....	.....
(Prof. Thirasak Rirksomboon)	(Assoc. Prof. Vissanu Meeyoo)

ABSTRACT

6071009063: Petrochemical Technology Program

Orawee Lamoonkit: Methane and Carbon Dioxide Adsorption on Al-based and Zr-based MOFs: Effects of Amino-Functionalization.

Thesis Advisors: Prof. Pramoch Rangsunvigit, Dr. Santi Kulpratipunja, Prof. Boonyarach Kitiyanan Dr. Chalita Ratanatawanate 99 pp.

Keywords: Adsorbed natural gas/ Methane adsorption/ Metal organic frameworks/ Amino group

For natural gas storage, adsorbed natural gas (ANG) technology has attracted great attention. There is a wide range of porous materials for ANG, but the most promising porous adsorbents for natural gas are metal organic frameworks (MOFs). This study examined adsorption of carbon dioxide and methane gases on aluminium (Al) based MOFs and zirconium (Zr) based MOFs including MIL-53(Al), MIL-53(Al)-NH_2, UiO-66, UiO-66-NH_2 25%, UiO-66-NH_2 50%, UiO-66-NH_2 75%, and UiO-66-NH_2. Experiments were carried out in a static system at 33^oC and pressures up to 100 psi. Characterization and structural analysis of the adsorbents were investigated by Fourier transform infrared spectroscopy (FTIR), x-ray diffraction (XRD), scanning electron microscopy (SEM), and N_2 adsorption/ desorption. The effects of amino functionalization on MIL-53(Al) and UiO-66 were discussed. The results showed that increasing the pressure led to the increase in methane and carbon dioxide adsorption. Moreover, the addition of amino functional group decreased the surface area and micropore volume but did not affect the crystalline structure. MIL-53(Al) and UiO-66-NH_2 displayed similar methane and carbon dioxide uptake, which was higher than the others. It seems that the high surface area and the effect of amino group on UiO-66-NH_2 contributed to the high methane and carbon dioxide adsorption. Furthermore, the carbon dioxide uptake was higher than the methane uptake, approximately two times due to its electrophile, which resulted in preferential adsorption toward carbon dioxide.

บทคัดย่อ

อรวี ละมูนกิจ: การดูดซับมีเทนและคาร์บอนไดออกไซด์บนวัสดุโครงข่ายโลหะอะลูมิเนียมและเซอร์โคเนียม: ผลของหมู่ฟังก์ชั่นของกรดอะมิโน (Methane and Carbon Dioxide Adsorption on Al-Based and Zr-Based MOFs: Effects of Amino-Functionalization) อ. ที่ปรึกษา: ศ. ดร. ปราโมช รังสรรค์วิจิตร ดร. สันติ กุลประทีปัญญา ศ. ดร. บุนยรัชต์ กิติยานันท์ และ ดร. ชลิตา รัตนเทวะเนตร 99 หน้า

Adsorbed Natural Gas (ANG) เป็นเทคโนโลยีที่ได้รับความสนใจสำหรับการกักเก็บก๊าซธรรมชาติเป็นอย่างมาก โดยใช้วัสดุรูพรุนเพราะความสามารถในการกักเก็บก๊าซ ถึงแม้ว่าจะมีวัสดุรูพรุนหลายชนิดสำหรับการกักเก็บก๊าซธรรมชาติ แต่ตัวดูดซับโครงข่ายโลหะอินทรีย์ (MOFs) เป็นตัวดูดซับทางเลือกที่มีคุณสมบัติที่ดีสำหรับการกักเก็บก๊าซธรรมชาติ งานวิจัยนี้เป็นการศึกษาการดูดซับก๊าซมีเทนและก๊าซคาร์บอนไดออกไซด์บน อะลูมิเนียม (Al) และ เซอร์โคเนียม (Zr) บน MOFs ประกอบไปด้วย MIL-53 (Al), MIL-53(Al)-NH_2, UiO-66, UiO-66-NH_2 25%, UiO-66-NH_2 50%, UiO-66-NH_2 75% และ UiO-66-NH_2 ที่อุณหภูมิ 33 องศาเซลเซียส และความดันถึง 100 ปอนด์ต่อตารางนิ้ว การวิเคราะห์โครงสร้างของตัวดูดซับตรวจสอบโดย ฟูเรียทรานสฟอร์มอินฟาเรดสเปกโตรสโคปี (FTIR) เอกซ์เรย์ดิฟแฟรกชัน(XRD) กล้องจุลทรรศน์อิเล็กตรอนแบบส่องกราด (SEM) และวิเคราะห์คุณลักษณะพื้นที่ผิว (N_2 adsorption/desorption) นอกจากนี้ยังศึกษาผลของการเพิ่มหมู่ฟังก์ชันอะมิโน (-NH_2) บน MIL-53 (Al) และ UiO-66 จากการทดลองพบว่า ปริมาณการดูดซับก๊าซมีเทนและคาร์บอนไดออกไซด์เพิ่มขึ้นเมื่อความดันเพิ่มขึ้น นอกจากนี้การเพิ่มของหมู่ฟังก์ชันอะมิโนทำให้พื้นที่ผิวลดลง แต่ไม่ส่งผลกระทบต่อโครงสร้างผลึก ตัวดูดซับ MIL-53 (Al) และ UiO-66-NH_2 สามารถดูดซับก๊าซมีเทนและคาร์บอนไดออกไซด์ได้ใกล้เคียงกันและสามารถดูดกก๊าซทั้งสองชนิดได้มากกว่าตัวดูดซับอื่นๆ เนื่องจากการมีพื้นที่ผิวสูงและการมีกลุ่มอะมิโนของ UiO-66-NH_2 มีผลช่วยให้การดูดซับมีเทนและคาร์บอนไดออกไซด์สูงขึ้น นอกจากนี้การดูดซับก๊าซคาร์บอนไดออกไซด์สูงกว่าการดูดซับก๊าซมีเทนประมาณสองเท่า เนื่องจากอิเล็กโทรไฟล์ของคาร์บอนไดออกไซด์ ส่งผลให้เกิดแรงระหว่างโมเลกุลตัวคาร์บอนไดออกไซด์กับตัวดูดซับเพิ่มขึ้น

GRAPHICAL ABSTRACT

6071009063: Petrochemical Technology Program

Orawee Lamoonkit: Methane and Carbon Dioxide Adsorption on Al-based and Zr-based MOFs: Effects of Amino-Functionalization.

Thesis Advisors: Prof. Pramoch Rangsunvigit, Dr. Santi Kulpratipunja, Prof. Boonyarach Kitiyanan Dr. Chalita Ratanatawanate 99 pp.

Keywords: Adsorbed natural gas/ Methane adsorption/ Metal organic frameworks/ Amino group

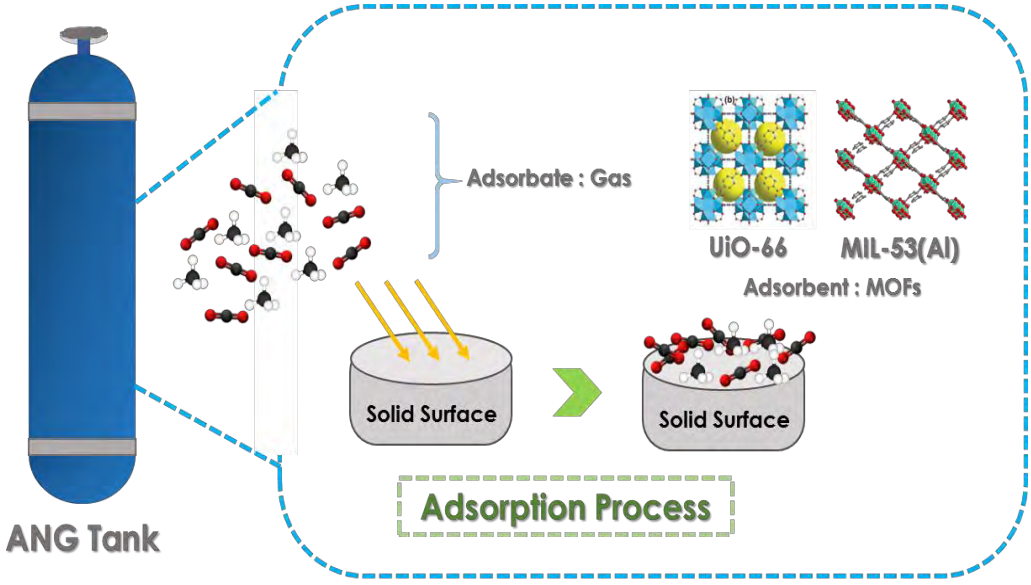

ACKNOWLEDGEMENTS

I would like to take this chance to my very great appreciation to my advisor, Prof. Pramoch Rangsunvigit, for his helpful suggestions, discussions, supervision from the very early stage of this research. He also provided me unflinching encouragement, patience, and support in various ways throughout my graduate thesis.

I would also like to thank my co-advisors, Dr. Santi Kulprathipanja and Prof. Boonyarach Kitiyanan for their advices, guidances, and willingness to share their bright thoughts and experience with me, which were very helpful for shaping up my ideas and research.

I would like to offer my special thanks to another co-advisor Dr. Chalita Ratanatawanate (NANOTEC, Thailand) for supporting all the adsorbents synthesis and giving precious recommendation throughout this thesis work.

I would like to thank Prof. Thirasak Rirksomboon and Assoc. Prof. Vissanu Meeyoo for kindly serving on my thesis committee. Their suggestions are certainly important and helpful for completion of this thesis.

This thesis work is funded by The 90th Anniversary of Chulalongkorn University Fund and Grant for International Integration: Chula Research Scholar, Ratchadapiseksomphot Endowment Fund, Chulalongkorn University, Thailand; The Petroleum and Petrochemical College; and the Center of Excellence on Petrochemical and Materials Technology, Thailand.

I would like to thank the entire faculty and staff at The Petroleum and Petrochemical College, Chulalongkorn University for their kind assistance and cooperation.

Most importantly, all the success things in my life always receive the love, encouragement, and support from my family.

TABLE OF CONTENTS

		PAGE
Title Page		i
Abstract (in English)		iii
Abstract (in Thai)		iv
Graphical Abstract		v
Acknowledgements		vi
Table of Contents		vii
List of Tables		ix
List of Figures		x
CHAPTER		
I	**INTRODUCTION**	1
II	**THEORETICAL BACKGROUND AND LITERATURE REVIEWS**	4
	2.1 Natural Gas	5
	2.2 Natural Gas Vehicles (NGVs)	7
	2.3 Natural Gas Storage Methods	8
	2.3.1 Compressed Natural Gas (CNG)	8
	2.3.2 Liquefied Natural Gas (LNG)	9
	2.3.3 Adsorbed Natural Gas (ANG)	10
	2.4 Adsorption and Desorption	12
	2.5 Adsorption Isotherms	15
	2.5.1 IUPAC Classification of Adsorption Isotherms	15
	2.5.2 Measurement of Adsorption Isotherms	18
	2.6 Adsorbents	20
	2.6.1 Activated Carbon	21
	2.6.2 Metal Organic Frameworks (MOFs)	23
	2.7 Literature Reviews	26

CHAPTER **PAGE**

III	**EXPERIMENTAL**	40
	3.1 Materials and Equipment	40
	3.1.1 Chemicals	40
	3.1.2 Materials	40
	3.2 Equipment	41
	3.3 Methodology	41
	3.2.1 Adsorbent Synthesis	41
	3.2.2 Adsorbent Characterization	45
	3.2.3 Adsorbent Measurement	46
	3.2.4 Gas Adsorption Calculation	47
	3.2.5 Modelling of Adsorption Isotherms	50
IV	**RESULTS AND DISCUSSION**	52
	4.1 Adsorbent Characterization	52
	4.1.1 N_2 Adsorption-Desorption Isotherms	52
	4.1.2 Fourier Transform Infrared Spectroscopy	56
	4.1.3 Scanning Electron Microscopy	59
	4.1.4 X-ray Diffraction Analysis	61
	4.2 Equilibrium Adsorption of Methane	63
	4.3 Equilibrium Adsorption of Carbon Dioxide	69
	4.4 Comparative Adsorption of Methane and Carbon Dioxide	76
V	**CONCLUSIONS AND RECOMMENDATIONS**	78
	5.1 Conclusions	78
	5.2 Recommendations	78
	REFERENCES	79

CHAPTER **PAGE**

APPENDICES

Appendix A Dubinin-Astakhov (DA) pore size distribution 85

Appendix B Methane Adsorption on Different Adsorbents at 33 °C 88

Appendix C Carbon Dioxide Adsorption on Different Adsorbents at 33°C 92

Appendix D Methane and Carbon Dioxide Adsorption on Different Adsorbents VS BET Surface area (m^2/g) at 33°C 96

Appendix E Methane and Carbon Dioxide Adsorption on Different Adsorbents VS Micropore Volume (cm^3/g) at 33°C 97

CURRICULUM VITAE 98

LIST OF TABLES

TABLE		PAGE
2.1	Chemical composition of natural gas	4
2.2	Comparing the greenhouse gas (GHG) emissions of several fossil fuels	5
2.3	Geometric properties of the five Zr-Based MOFs considered in the qualitative comparison	31
2.4	BET surface area	31
2.5	Porous structure of MIL-125(Ti), NH_2-MIL-125(Ti) and MIX-MIL-125(Ti) samples	34
2.6	Density and porosity measurements summary	38
4.1	Physical properties of adsorbents	55

LIST OF FIGURES

FIGURE		PAGE
2.1	World natural gas consumption in trillion cubic metre (tcm) unit, 2012-2040.	6
2.2	Comparison of the methane adsorption capacity of an adsorbent filled tank (ANG) and an empty tank pressurized up to 4 MPa.	11
2.3	Representation of the adsorption process of a gas on a solid surface for a given pressure and temperature.	13
2.4	Adsorption and desorption process.	14
2.5	The IUPAC classification of adsorption isotherms for gas/solid equilibria.	16
2.6	New classification of adsorption isotherms.	18
2.7	Experimental setup for volumetric measurement of pure gas adsorption equilibrium.	19
2.8	Schematic diagram of the gravimetric apparatus.	20
2.9	Pelleted, granular, and powder activated carbon.	23
2.10	Simple framework connections of metal nodes and organic linkers for the construction of MOFs in a cubic topology.	24
2.11	Example of the coordination geometry between (A) metal ions and (B) organic linkers used.	24
2.12	Schematic illustration of the UiO-66(Zr) structure. Left (a,c): octahedral cage; right (b,d): tetrahedral cages. Hydrogen atoms on the organic linkers were omitted for clarity. The large green spheres represent the void regions inside the cages.	25
2.13	Labeling of MIL-53(Al)'s crystallographic structure.	26

FIGURE **PAGE**

2.14 Variation of methane adsorption capacity with BET surface area, at a pressure of 500 psi and temperature of 298 K. 27

2.15 Variation of methane adsorption capacity with pressure at two different temperatures. 28

2.16 Adsorption isotherms (a) and adsorption enthalpy (b) of CO_2 and CH_4 at 302 K on the nanoporous carbon based on pyrogallol-formaldehyde. 29

2.17 Depiction of the fcu topology which is shared by UiO-66, DUT-52, and UiO-67. Also the inorganic brick is common between these materials, which differ only in the organic linker. Zirconium atoms are shown in cyan, oxygen atoms in red, carbon atoms in grey, and hydrogen atoms in white. 30

2.18 CO_2 adsorption on UiO-66-NO_2, UiO-66-NO_2-NH_2, UiO-66-NH_2-NO_2 and UiO-66-NH_2 samples at 273 K. 32

2.19 CH_4 adsorption on UiO-66-NO_2, UiO-66-NO_2-NH_2, UiO-66-NH_2-NO_2 and UiO-66-NH_2 samples at 273 K. 33

2.20 CO_2 adsorption on MIL-125(Ti), NH_2-MIL-125(Ti) and MIX-MIL-125(Ti) at 298 K. 34

2.21 CH_4 adsorption on MIL-125(Ti), NH_2-MIL-125(Ti) and MIX-MIL-125(Ti) at 298 K. 35

2.22 Selectivities of CO_2/CH_4 at varying pressures and 298 K 36

2.23 A decomposition of the volumetric storage for comparing the relative contributions of the excess adsorption (solid square), the intra-granular porosity (solid circles), and the inter-granular porosity (open circles). 37

FIGURE **PAGE**

2.24 A comparison of the contributions to the total volumetric storage (X symbols) from the excess adsorption (square symbols), intra-granular porosity (solid circles), and intergranular porosity (open cycles) for the maximally densified materials. 39

3.1 Schematic of the experimental set-up for the equilibrium adsorption of carbon dioxide. 46

3.2 Schematic of the experimental set-up for the equilibrium adsorption of methane. 47

4.1 N_2 adsorption-desorption isotherms of Zr-based MOFs at -196°C. 53

4.2 N_2 adsorption-desorption isotherms of Al-based MOFs at -196 °C. 54

4.3 Fourier transform infrared spectroscopy of UiO-66, UiO-66-NH_2 25%, UiO-66-NH_2 50%, UiO-66-NH_2 75% and UiO-66-NH_2. 57

4.4 Fourier transform infrared spectroscopy of MIL-53(Al) and MIL-53(Al)-NH_2. 58

4.5 Scanning electron micrographs of (a) UiO-66, (b) UiO-66-NH_2 25%, (c) UiO-66-NH_2 50%, (d) UiO-66-NH_2 75% and (e) UiO-66-NH_2. 59

4.6 Scanning electron micrographs of (a) MIL-53(Al) and (b) MIL-53(Al)-NH_2. 60

4.7 X-ray diffraction (XRD) patterns of UiO-66, UiO-66-NH_2 25%, UiO-66-NH_2 50%, UiO-66-NH_2 75% and UiO-66-NH_2. 61

4.8 X-ray diffraction (XRD) patterns of MIL-53(Al) and MIL-53(Al)-NH_2. 61

FIGURE **PAGE**

4.9	Methane adsorption on UiO-66, UiO-66-NH_2 25%, UiO-66-NH_2 50%, UiO-66-NH_2 75% and UiO-66-NH_2 at 33 ^oC.	63
4.10	Methane adsorption on UiO-66, UiO-66-NH_2, MIL-53(Al) and MIL-53(Al)-NH_2 at 33 ^oC.	64
4.11	Structure of (a) UiO-66 and (b) MIL-53(Al).	65
4.12	Equilibrium isotherm modelling for methane adsorption on UiO-66 at 33 ^oC.	66
4.13	Equilibrium isotherm modelling for methane adsorption on UiO-66-NH_2 25% at 33 ^oC.	66
4.14	Equilibrium isotherm modelling for methane adsorption on UiO-66-NH_2 50% at 33 ^oC.	67
4.15	Equilibrium isotherm modelling for methane adsorption on UiO-66-NH_2 75% at 33 ^oC.	67
4.16	Equilibrium isotherm modelling for methane adsorption on UiO-66-NH_2 at 33 ^oC.	68
4.17	Equilibrium isotherm modelling for methane adsorption on MIL-53(Al) at 33 ^oC.	68
4.18	Equilibrium isotherm modelling for methane adsorption on MIL-53(Al)-NH_2 at 33 ^oC.	69
4.19	Carbon dioxide adsorption on UiO-66, UiO-66-NH_2 25%, UiO-66-NH_2 50%, UiO-66-NH_2 75%, and UiO-66-NH_2 at 33 ^oC.	70
4.20	Carbon dioxide adsorption on UiO-66, UiO-66-NH_2, MIL-53(Al), and MIL-53(Al)-NH_2 at 33 ^oC.	71
4.21	Equilibrium isotherm modelling for carbon dioxide adsorption on UiO-66 at 33 ^oC.	72

FIGURE **PAGE**

4.22	Equilibrium isotherm modelling for carbon dioxide adsorption on UiO-66-NH_2 25% at 33 ºC.	73
4.23	Equilibrium isotherm modelling for carbon dioxide adsorption on UiO-66-NH_2 50% at 33 ºC.	73
4.24	Equilibrium isotherm modelling for carbon dioxide adsorption on UiO-66-NH_2 75% at 33 ºC.	74
4.25	Equilibrium isotherm modelling for carbon dioxide adsorption on UiO-66-NH_2 at 33 ºC.	74
4.26	Equilibrium isotherm modelling for carbon dioxide adsorption on MIL-53(Al) at 33 ºC.	75
4.27	Equilibrium isotherm modelling for carbon dioxide adsorption on MIL-53(Al)-NH_2 at 33 ºC.	75
4.28	Adsorption of methane and carbon dioxide on UiO-66, UiO-66-NH_2 25%, UiO-66-NH_2 50%, UiO-66-NH_2 75%, UiO-66-NH_2, MIL-53(Al), and MIL-53(Al)-NH_2 at 100 psi and 33 °C.	76

CHAPTER I
INTRODUCTION

Instability in the fossil-fuel and oil markets, and increasingly in environmental concerns have attracted great attention around the globe. Fossil sources are limited and their refinement and combustion contribute substantially to global warming. Consequently, research toward alternative transportation fuels have increasingly increased.

The need for alternative energy sources with lower emissions to replace the current petroleum-derived fuels has gained much the attention. Hydrogen and natural gas are two of the alternative fuels that have common characteristics of being gaseous at room temperature and have high heating value (Blanco *et al*., 2016). Natural gas has been touted as importance of a transition to a cleaner and more saver energy in the future. It consists mainly of methane, which has the maximum H to C ratio than any other hydrocarbon-based fuels, thus resulting lower release of carbon monoxide and carbon dioxide per unit of energy generation due to its combustion (Shan *et al*., 2017). Furthermore, it results lower SO_x and NO_x emissions, making it a significantly cleaner fuel than gasoline and diesel (Middleton and Eccles, 2013).

Natural gas has many uses in industry, transportation, and households. For the transportation, natural gas is commonly required in its liquid form, the fact that introduces difficulties for its transportation and storage. The most challenging for using natural gas as a transportation fuel is its limited driving distance because of the comparatively low volumetric energy storage density. There are three main methods for natural gas transportation, which are compressed natural gas (CNG), liquefied natural gas (LNG), and adsorbed natural gas (ANG).

Currently available technologies for natural gas storage include CNG that stores natural gas as supercritical fluid at room temperature and 200-300 bar. The use of CNG is limited to costly multi-stage gas compressors, which consume high energy and require large and thick metal fuel tanks (Mason *et al*., 2014). LNG is achieved at -162^{o}C close to atmospheric pressure and limited to the difficulties in handling a cryogenic fuel (Chen *et al*., 2004). As an alternative to LNG and CNG, ANG has been considered as a promising strategy to overcome the above issues, which involve in

storing methane under convenient temperature and pressure in light-weight fuel tanks (Yeon *et al*., 2010).

In ANG method, the maximum gas storage density becomes the ultimate requirement, in order to store the volume of gas per volume of storage vessel. Depending on the characteristics of adsorbents, the volumetric adsorption capacity will be different so does the volumetric energy density (Lozano-Castello *et al*., 2002). Many absorbents have been evaluated for gas storage. They include zeolites, activated carbon, and metal organic frameworks (MOFs), which have high specific surface area, pore size and high packing density to contain gas molecules.

Several articles reported that zeolites with limited structure display a relatively low methane storage capacity (Lozano-Castello *et al*., 2002). It also has the extremely hydrophilic properties that can enhance interactions with water rather than methane, thus minimizing their storage capacity for natural gas. Activated carbon with its high porosity, surface area, which can avoid packing-related loss of efficiency. Nonetheless, activated carbon still has limitations in pore size distribution, accessible surface area, and surface functionalization (Zheng *et al*., 2018). MOFs, with solid crystalline structure and high-density, can improve methane storage because of their high porosity, tunable pores, and various factors of functional group (Li *et al*., 2016). An important reason for the use of these kinds of materials is the elevated adsorptive potential in the micropores.

Recently, zirconium-based MOFs (Zr-based MOFs) and aluminium-based MOFs (Al-based MOFs) have stable properties (Nawrocki *et al*., 1993) making it attractive in the synthesis of MOFs. Modification and application of Zr-MOFs and Al-based MOFs have been studied by some researchers. For example, the synthesis of organic ligand with different length of this framework could be controlled to get UiO-66, UiO-67, and UiO-68 (Cavka *et al*., 2008). Kandiah *et al*. (2010) synthesized Zr-MOF (UiO-66) with different functional groups by using different linker ligands, such as nitroterephthalic acid (BDC-N_2O), and bromoterephthalic acid (BDC-Br_2) (Kandiah *et al*., 2010). Silva *et al*. (2010) used UiO-66 and UiO-66-NH_2 as photocatalysts for hydrogen generation, while Vermmortele *et al*. (2011) selected UiO-66-NH_2 (amino-UiO-66) for the cross-aldol condensation. Moreover, Binh *et al*. (2015) used MIL-53(Al) for gas separation in mixed matrix membrane. However, a

few investigations have been reported in Zr-based MOFs and Al-based MOFs application for methane and carbon dioxide adsorption.

In this work, comparison of adsorption capacity of methane and carbon dioxide, which are main components in natural gas, was observed at moderate pressure and room temperature, using Zr-based MOFs and Al-based MOFs. UiO-66, amino-functionalized UiO-66, MIL-53(Al), and amino-functionalized MIL-53(Al) were selected as absorbents due to their high thermal stability, chemical stability, and abundant pores. In addition, the characterization of absorbents was analyzed with Fourier-transform infrared spectroscopy (FTIR), scanning electron microscope (SEM), and x-ray powder diffraction (XRD).

CHAPTER II
THEORETICAL BACKGROUND AND LITERATURE REVIEWS

2.1 Natural Gas

Natural gas is one type of fossil fuel that is abundant in the world. It is reliable, efficient, and safe than other fossil fuels. It is often called 'natural gas' because it is a naturally occurring hydrocarbon. It is colorless and odorless in its pure form. The composition of natural gas varies depending on a number of factors like the origin, location of deposit and geological structure. Natural gas is a mixture of lightweight alkanes including methane (CH_4), ethane (C_2H_6), propane (C_3H_8), n-butane and isobutane (C_4H_{10}), and pentanes (C_5H_{12}) (www.uniongas.com). The C_3, C_4, and C_5 hydrocarbons are removed before the gas is sold. The commercial natural gas supplied to the customer is therefore primarily a mixture of methane and ethane. The propane and butanes removed from natural gas are usually liquefied under pressure and sold as LPGs. The chemical composition of natural gas is given in Table 2.1.

Table 2.1 Chemical composition of natural gas (www.uniongas.com)

Component	Typical Analysis (mole %)	Range (mole %)
Methane	93.9	87.0 - 97.0
Ethane	4.2	1.5 - 9.0
Propane	0.3	0.1 - 1.5
iso-Butane	0.03	0.01 - 0.3
normal-Butane	0.03	0.01 - 0.3
iso-Pentane	0.01	trace - 0.04
normal-Pentane	0.01	trace - 0.04
Hexanes plus	0.01	trace - 0.06

Table 2.1 (Continued) Chemical composition of natural gas (www.uniongas.com)

Component	Typical Analysis (mole %)	Range (mole %)
Nitrogen	1.0	0.2 - 5.5
Carbon Dioxide	0.5	0.05 - 1.0
Oxygen	0.01	trace - 0.1
Hydrogen	trace	trace - 0.02

Table 2.2 Comparing the greenhouse gas (GHG) emissions of several fossil fuels (EIA - Natural Gas Issues and Trends 1998)

Pollutant (pounds per billion btu of energy input)	Natural Gas	Oil	Coal
Carbon dioxide	117,000	164,000	208,000
Carbon monoxide	40	33	208
Nitrogen oxides	92	448	457
Sulfur dioxide	1	1,122	2,591
Particulates	7	84	2,744
Mercury	0.000	0.007	0.016

The main products of combustion of natural gas are carbon dioxide and water vapor. The combustion of natural gas releases very small amounts of nitrogen oxides, sulfur dioxide, carbon dioxide, carbon monoxide, other reactive hydrocarbons and virtually no particulate matter. Coal and oil are composed of more complex molecules, and when they combusted, they release higher levels of harmful emissions such as nitrogen oxides and sulfur dioxide and also release ash particles

into the environment (www.eia.gov). Summarizing the different chemical emissions of competition fuels as shows in Table 2.2.

Natural gas supplies 22% of the energy used worldwide, and makes up nearly a quarter of electricity generation, as well as playing an important role as a feedstock for industry. Natural gas is a versatile fuel and its growth is linked in part to its environmental benefits relative to other fossil fuels, particularly for air quality as well as greenhouse gas emissions. Moreover, global demand for natural gas is forecasted to increase at an average 1.6% from 2012 to 2040 in the International Energy Outlook (IEO) 2016, reference case. Figure 2.1 shows consumption of natural gas increases in every IEO region, with demand in nations outside the Organization for Economic Cooperation and Development (non-OECD) increasing more than twice as fast as in the OECD (www.eia.gov).

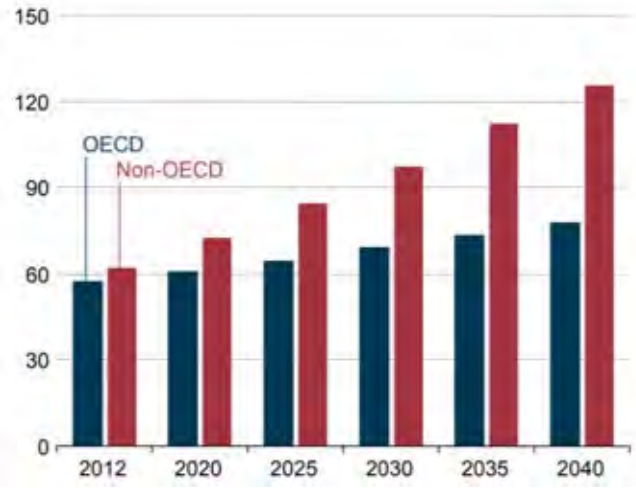

Figure 2.1 World natural gas consumption in trillion cubic metre (tcm) unit , 2012-2040 (www.eia.gov).

2.2 Natural Gas Vehicles (NGVs)

Natural gas vehicles (NGVs) are great ways for long distance, centrally fueled fleets. In many cases, compressed natural gas (CNG) can provide adequate range for the required vehicle application. For vehicles that travel long distances, liquefied natural gas (LNG) is a good choice. The advantages of natural gas as a transportation fuel include its domestic availability, widespread distribution infrastructure, and reduced greenhouse gas emissions compared to conventional gasoline and diesel fuels. Furthermore, the horsepower, acceleration, and cruise speed of NGVs are equal to the equivalent conventional vehicles. Also, compared with conventional diesel and gasoline vehicles, NGVs offer other air-quality benefits (Kavalov, 2011). Although natural gas has many benefits for using in transportation vehicles, there are also some limitations. The mileage of NGVs is generally less than that of comparable diesel or gasoline vehicles because of the comparative lower energy density of natural gas. Additional storage tanks can increase distance, but the extra weight may displace cargo capacity. The ensuring problem is how to store enough fuel aboard the vehicle, in order to secure an acceptable driving range. On volumetric basis, 1 cubic meter of natural gas roughly corresponds to 1.0 liter of gasoline or 1.1 liter of diesel (Kavalov, 2011).

There are three types of NGVs:

Dedicated : These vehicles are designed to run only on natural gas.

Bi-fuel : These vehicles have two separate fueling systems that enable them to run on either natural gas or gasoline.

Dual-fuel : These vehicles have fuel systems that run on natural gas but use diesel fuel for ignition assistance. This configuration is traditionally limited to heavy-duty vehicles.

Light-duty vehicles are typically equipped with dedicated or bi-fuel systems, while heavy-duty vehicles use dedicated or dual-fuel systems. CNG vehicles store natural gas in tanks where it remains in the gaseous state. More fuel can be stored onboard a vehicle using LNG because the fuel is stored as a liquid, therefore making its energy density greater than that of CNG (Solar *et al*., 2010).

2.3 Natural Gas Storage Methods

The transportation and storage of natural gas or methane has been one of the barriers to natural gas utilization. The low density of natural gas makes it difficult to transport and store because methane (the major composition of natural gas) in its gaseous form has density of 15.4 g/m^3 at standard temperature and pressure compared to gasoline, which has a density of 744,000 g/m^3 (Curran *et al*., 2014). The options for natural gas transport or storage are in the form of compressed natural gas (CNG), liquefied natural gas (LNG) and adsorbed natural gas (ANG).

2.3.1 Compressed Natural Gas (CNG)

Typically, CNG used as a transportation fuel for light-duty vehicle applications, CNG is natural gas stored at high pressure. The increased pressure allows large volumes of gas to be contained and transported within a given unit of space. The density of CNG can be reduced by refrigeration, and this allows for greater transportation volume. Though compression and decompression equipment may be cheaper and more economical for smaller unit sizes, the transportation of CNG generally requires over 200 bars of pressure and 25 °C of temperature. The investment into and the operating costs of CNG carriers are the downside of CNG transportation. The volumetric energy density of CNG is about 8.8 MJ/l (one fourth that of gasoline). Thus, with all efficiencies being equal, a CNG vehicle requires a tank 4 times the size of a gasoline tank for the same driving range (Demirbas, 2002).

2.3.1.1 Advantages of compressed natural gas

a. Lead fouling of spark plug is eliminated because absence of any lead or benzene content.

b. Low maintenance cost compared to other fuel-powered vehicles.

c. CNG fuel system are sealed, which prevents any spill or evaporation losses.

d. Due to its high auto ignition temperature (540 ^{o}C) and narrow range (5-15 %) of flammability, it is less likely to auto-ignite on hot surface.

e. Compared to other commercial fuels like gasoline, diesel emits significantly less pollutant such as carbon dioxide, hydrocarbon, carbon monoxide, nitrogen oxide, sulfur oxide, and particulate matter.

2.3.1.2 Drawbacks of compressed natural gas

Compared to conventional gasoline powered vehicles, compressed natural gas vehicles require greater amount of space.

2.3.2 Liquefied Natural Gas (LNG)

In this method, natural gas is liquefied under pressure of 10-20 bar at -162 ^{o}C. LNG is suitable for heavy-duty vehicle applications. And LNG also requires the use of complex and expensive liquefactions equipment, thermo like tanks, and significant energy consumption (25-35% of original energy gas content) for the liquefaction and degasification. The density of LNG is roughly 0.41-0.5 kg/L, depending on temperature, pressure, and composition. In its liquid state, LNG is not explosive and cannot burn. For LNG to burn, it must first vaporize, then mix with air in the proper proportions (the flammable range is 5-15%), and then be ignited. Modern LNG storage tanks are typically the full containment type, which is a double-wall construction with a reinforced concrete outer wall and a high-nickel steel inner tank, with extremely efficient insulation between the walls. LNG must be kept cold to remain a liquid, independent of pressure. LNG is transported in specially designed ships with double hulls protecting the cargo systems from damage or leaks. Transportation and supply are an important aspect of the gas business, since LNG reserves are normally quite distant from consumer markets (Demirbas, 2010).

The advantage of LNG is that it offers an energy density comparable to gasoline and diesel fuel, extending range, and reducing refueling frequency. However, LNG also has some drawbacks because of large tanks. LNG transportation requires large and expensive infrastructure and hard to maintenance. Using in long term storage is also difficult for LNG, as significant losses occur due to warming up and boiling off too fast because the LNG increases inevitably the temperature within the tank, the pressure rises and could result in a dangerous situation. Moreover, the filling of the tank must be required an expert on cryogenic liquids handling (Solar *et al*., 2010).

2.3.3 Adsorbed Natural Gas (ANG)

Adsorbed natural gas (ANG) systems has been considered as a promising strategy to overcome the above-mentioned problems of CNG and competitive to gasoline or diesel fuel, the cost and space of its storage and refueling systems must be reduced dramatically. Application of a physical adsorption phenomenon in the solid media as adsorbent is one way to solve this problem. ANG technology based on natural gas adsorption in porous materials at relatively low pressures 3.5-4 MPa and at room temperature, which is above vapour-liquid critical temperature of -83.15 ºC of methane, is a challenge to the liquid fuel application. This pressure system is obtainable by single-stage compression, allowing natural gas stored in the tank at the same amount of high-pressure storage container. Using lower vessel pressures offers two main benefits. Firstly, it allows good design flexibility in tank configuration and placement. Secondly, it reduces the cost to compress natural gas to high pressures (Vasiliev *et al.,* 2000).

The performance of ANG technology not only relates to the amount of methane adsorbed to store but also depends on the amount of methane can be delivered to an engine. Delivery capacity is indicated as the volume of gas discharge per volume of storage tank. In practical, delivery capacity is more important than the amount of methane storage due to it indicates the driving range of natural gas vehicles (NGVs). Thus, maximization of methane adsorption and low limiting delivery capacity are two key functions that define the delivery capacity. The delivery capacity or working capacities of adsorbents also associate with thermal effects from adsorption and desorption. Adsorption prefers condition at low temperature adsorbent bed due to exothermic process. On the other hand, desorption prefers condition at high temperature adsorbent bed due to endothermic process (Shen *et al*., 2015). For instead, when the releasing of heat during adsorption is not efficiently dispersed or offset, there are over heat in adsorbent bed, which results in less methane adsorbed at that pressure. Similarly, when the heat from adsorption cannot recycle during discharge, the temperature of adsorbent bed is not high enough resulting in more methane maintained in adsorbents at low pressure. These factors significantly decrease the working of adsorbent. Thus, it is necessary to improve strategy for reducing losses in working capacity as less as possible (Li *et al*., 2016).

In addition, the total storage capacity is always greater than the delivery capacity by around 15-30% (Shen *et al*., 2015).

Figure 2.2 presents the methane adsorption capacity of an adsorbent filled tank (ANG) and an empty tank pressurized up to 4 MPa. It can be observed that the methane adsorption capacity of the adsorbent filled tank is much higher than the empty tank. That happens when the adsorbed phase has a greater density than the gas phase in equilibrium with it. Consequently, there is an enhancement in a storage system of fixed volume because a greater amount of gas is adsorbed compared to the volume of gas displaced by the adsorbent volume (Lozano-Castelló *et al.*, 2002).

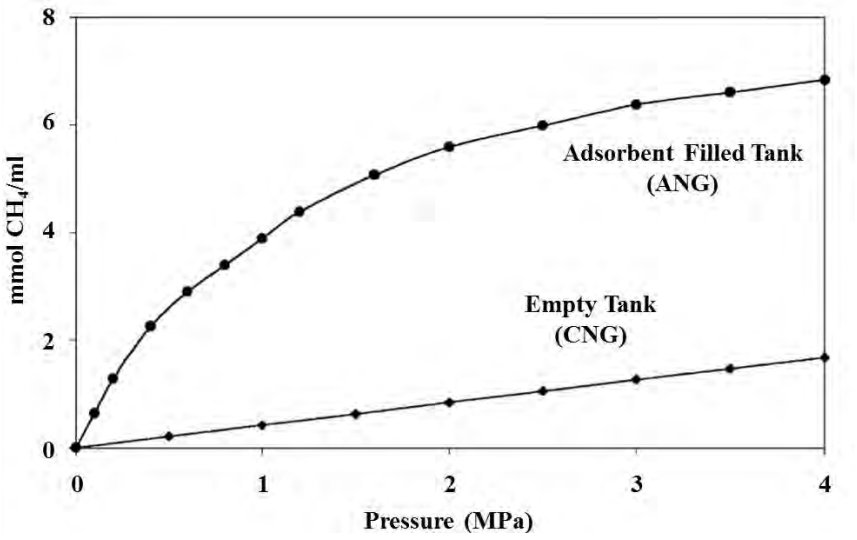

Figure 2.2 Comparison of the methane adsorption capacity of an adsorbent filled tank (ANG) and an empty tank pressurized up to 4 MPa (Lozano-Castelló *et al.*, 2002).

The search for a suitable porous material, in terms of further improving ANG storage volumetric energy density and lowering the adsorbent cost to the end use, is currently an active area of research. It can be seen that a lot of work has been, and is being, carried out mainly on three classes of microporous solids: zeolites, activated carbons and metal organic frameworks. Moreover, novel adsorbents, such as organic gels have been explored for the adsorption of methane.

The good adsorbents, presenting the highest ANG energy densities, and thus it shows the highest storage capacities (Lozano-Castelló *et al.*, 2002).

2.4 Adsorption and Desorption

Adsorption is a capability of all solid substances to attract to their surfaces molecules of gases or solutions, with which they are in contact. Solids that are used to adsorb gases or dissolved substances are called adsorbents, and the adsorbed molecules are usually referred to collectively as the adsorbate. Adsorption refers to the collecting of molecules by the external surface or internal surface (walls of capillaries or crevices) of solids or by the surface of liquids as shown in Figure 2.3. Adsorption can be either physical or chemical in nature. Physical adsorption resembles the condensation of gases to liquids and depends on the physical, or van der Waals, force of attraction between the solid adsorbent and the adsorbate molecules. There is no chemical specificity in physical adsorption, any gas tending to be adsorbed on any solid if the temperature is sufficiently low or the pressure of the gas sufficiently high. In chemical adsorption, gases are held to a solid surface by chemical forces that are specific for each surface and each gas. Chemical adsorption occurs usually at higher temperatures than those at which physical adsorption occurs. Furthermore, chemical adsorption is ordinarily a slower process than physical adsorption and, like most chemical reactions, frequently involves energy of activation (www.chemistrylearning.com).

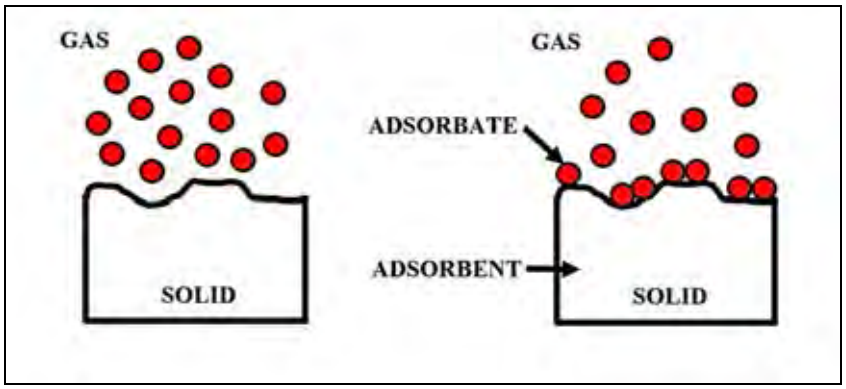

Figure 2.3 Representation of the adsorption process of a gas on a solid surface for a given pressure and temperature (Solar *et al*., 2010).

Moreover, adsorption is a spontaneous process. For reaction or process to be spontaneous, there must be decreases in free energy of the system. The result is Gibbs free energy of the system must have negative value. Therefore, for a reaction to be spontaneous heat energy has to be negative. From these conditions, adsorption process is an exothermic reaction. Adsorption isotherms depend on of the type, concentration and distribution of adsorption sites, pore structure of adsorbent, adsorptive and experimental conditions. In this work, the adsorption of methane and carbon dioxide on MOFs are studied. Actually, gases are favorable adsorbed on polar adsorbate that adsorption starts on the polar sites (Fletcher *et al*., 2006).

Besides, various studies have concluded that the features required by an adsorbent to be adequate for the ANG process are (Solar *et al*., 2010):

a) High adsorption capacity.

b) High adsorption/desorption relations.

c) Micropore sizes of approximate 0.8 nm (bigger than the sizes of two molecules of methane) to facilitate the gas release at room temperature.

d) High packaging density to ensure that the storage capacity and the energetic density are high.

e) Low adsorption heat and high specific heat to minimize the temperature variation in the tank through the adsorption and desorption processes.

f) Suitable properties for the mass transference.

g) Being extremely hydrophobic.

h) Being inexpensive.

While desorption is the reverse process of adsorption see in Figure 2.4. Desorption is a phenomenon whereby an adsorbed substance is released from or through an adsorbent. This occurs in a system being in the state of sorption equilibrium between bulk phase (fluid, i.e. gas or liquid solution) and an adsorbing surface. When the concentration or pressure of substance in the bulk phase is lowered, some of the adsorbed substance changes to the bulk state. Moreover, the adsorption phenomenon involves an increment of the gas density in the neighborhood of the contact surface, and since the process is spontaneous, the change in the free energy of Gibbs is less than zero. Given that the entropy change is also below zero (a decrease in the degree of freedom of the gas molecules during the process), the enthalpy change is lower than zero. Thus, the process is exothermic. In contrast, the desorption phenomenon is endothermic (Solar *et al*., 2010).

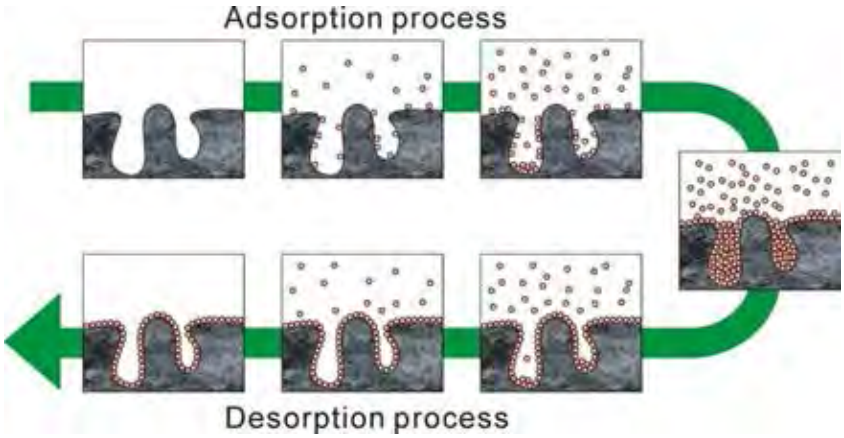

Figure 2.4 Adsorption and desorption process (www.olenitec.com).

2.5 Adsorption Isotherms

Adsorption isotherms are critical in optimizing the use of adsorbents, and are important for the description of how adsorbate will interact with an adsorbent. It is usually described to determine the amount of adsorbate on the adsorbent as a function of its pressure (if adsorbent is gas) or concentration (if adsorbent is liquid) at constant temperature. In case of gas-solid adsorption, when a gas comes into contact with a solid surface, molecules of the gas will adsorb to the surface in quantities that are a function of their partial pressure in the solid. The measurement of the amount of gas adsorbed over a range of partial pressures at a single temperature results in a graph known as an adsorption isotherm. Adsorption isotherm in physical chemistry is generally expressed as concentration of adsorbed phase (or amount of gas adsorbed) per unit mass of adsorbent. It is a function of both pressure and temperature, besides the nature of the gas. The data may be represented as isotherms, V (P), at constant T, isobars, V (T) at constant P, or isosteres, P (T) at constant V. Among them, isotherms are the closest one to direct experiments. Measurements of pure component isotherms can easily be conducted and are generally available for adsorption design study. Meanwhile, the investigation of multi-component isotherms often hit a difficulty since the experimental data over design ranges of pressure, temperature, and composition are impractically measurable. Therefore, many literature models are available to predict the mixture behaviors from pure component isotherm data (Jeong *et al*., 2007).

2.5.1 IUPAC Classification of Adsorption Isotherms

Most analysis of adsorption equilibria begins with classification of the isotherms. This classification is important in theoretical modeling of adsorption phenomena. It also is important for practical reasons. As an illustration, consider surface area measurements using the BET method. There are international standards and a number of commercial devices for using this method in different applications. However, according to the IUPAC manual, the first step is to identify the isotherm type and hence the nature of the adsorption process. The modern version of IUPAC classification scheme is based on an earlier classification by Brunauer which had five

types of isotherms. It has six types of isotherms for gas/solid equilibria as shown in Figure 2.5 (Donohue and Aranovich, 1998).

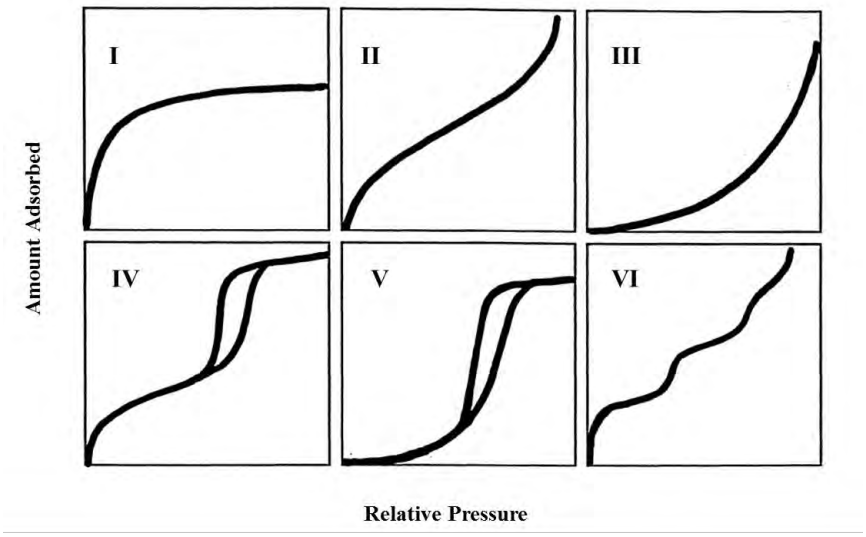

Figure 2.5 The IUPAC classification of adsorption isotherms for gas/solid equilibria (Donohue and Aranovich, 1998).

Type I isotherm approaches a limiting value and usually is used to describe adsorption on microporous adsorbents. Types II and III describe adsorption on macroporous adsorbents with strong and weak adsorbate-adsorbent interactions, respectively. Types IV and V are given by monolayer and multilayer adsorption plus capillary condensation. Type VI was not included in the Brunauer classification, it illustrates that the adsorption isotherms can have one or more steps (Donohue and Aranovich, 1998).

The classification of pores, according to their size, which is recommended by IUPAC, is described below (Solar *et al*., 2010):

a) Pores with widths exceeding about 50 nm or 500 Å are called macropores.

b) Pores with widths not exceeding about 2 nm or 20 Å are called micropores.

c) Pores with widths between 2 nm (20 Å) and 50 nm (500 Å) are called mesopores.

However, the current IUPAC classification has two deficiencies: it is incomplete and it gives the incorrect impression that adsorption isotherms are always monotonic functions of pressure. Though not stated explicitly in the IUPAC publications, the IUPAC classification is limited to condensable vapors, but many important gas/solid systems fall outside this classification (for example, nitrogen, oxygen, fluorine, hydrogen, carbon dioxide, carbon monoxide, nitric oxide, methane, ethylene, and some freons at a room temperature). Moreover, this restriction is ambiguous because gases can be non-condensable in the bulk, but condensable in pores of an adsorbent. In 1998, Donohue and Aranovich presented a comprehensive analysis of adsorption behavior that is based on experimental results, molecular simulations, and lattice theory concepts proposed by Ono and Kondo in 1960. Figure 2.6 shows a new classification of adsorption isotherms. While general, the classification shown in Figure 2.6 is meant to be qualitative and does not show all possible details. In this classification (Donohue and Aranovich, 1998):

a) Type I shows adsorption isotherms on microporous adsorbents for subcritical, near critical and supercritical conditions. At supercritical conditions, the isotherm is not monotonic.

b) Types II and III give adsorption isotherms on macroporous adsorbents with strong and weak affinities, respectively. For low temperatures, these Types have steps, but increasing temperature transforms them into the smooth monotonic curves, which are like those in Types II and III of the IUPAC classification. However, near the critical temperature, these isotherms change dramatically to non-monotonic behavior showing sharp maxima, and further increase in temperature leads to isotherms with smooth maxima.

c) Types IV and V characterize mesoporous adsorbents with strong and weak affinities, respectively. For lower temperatures, they show adsorption hysteresis. Supercritical isotherms for mesoporous adsorbents, which are predicted by lattice theory and the logic of this classification scheme, are also included.

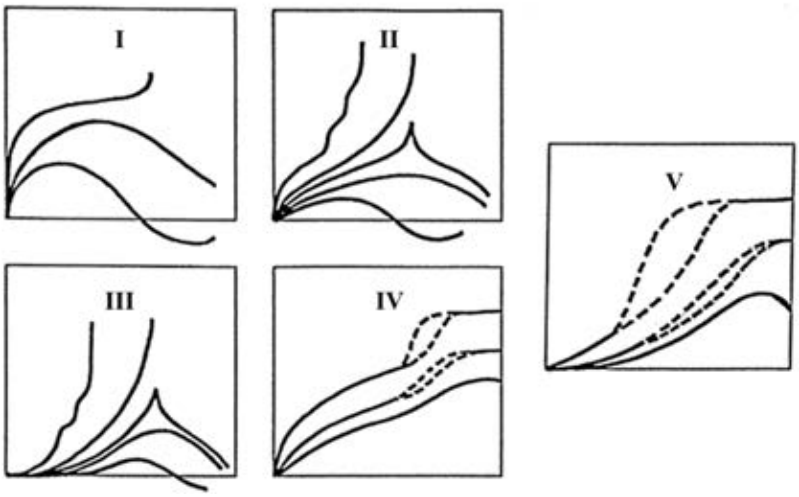

Figure 2.6 New classification of adsorption isotherms (Donohue and Aranovich, 1998)

2.5.2 IUPAC Measurement of Adsorption Isotherms

Adsorption measurement is to determine the adsorption characteristics of adsorbent-adsorbate pair, including isotherm, kinetics, and heat of adsorption data. All these parameters are key variables for simulation and modeling of any adsorption process. Currently available adsorption measurement techniques or facilities can be basically classified into three types, i.e. volumetric, gravimetric, and gas flow (Kumar, 2011).

2.5.2.1 Gas flow technique

This approach, firstly proposed by Nelsen and Eggertsen, was a variant of gas chromatography. It used helium as carrier gas and a gas flow meter was used to determine the partial pressure of the adsorbate. The adsorbed volume was determined from the peak area in the adsorption/desorption chart recorded by a potentiometer over a period. This apparatus is simple, cheap and easy to handle, and no vacuum is required, and available gas chromatographers can be also modified for this approach. However, the measurement of the adsorbed amount is indirect and the method does not claim high accuracy. The method is usually applied for fast single point determinations of the specific surface area. Multipoint measurements of isotherms become complicated (Kumar, 2011).

2.5.2.2 Gas adsorption volumetric technique

In this technique, a given amount of adsorptive gas is expanded into a vessel, which includes a sorbent sample, and which initially has been evacuated upon expansion, the adsorptive gas is partly adsorbed on the (external and internal) surface of the sorbent material, partly remaining as gas phase around the sorbent. By a mass balance, the amount of gas being adsorbed can be calculated if the void volume of the sorbent, i.e. the volume, which cannot be penetrated by the adsorptive gas molecules, is known at least approximately. The line diagram of volumetric setup is shown in Figure 2.7 (Kumar, 2011).

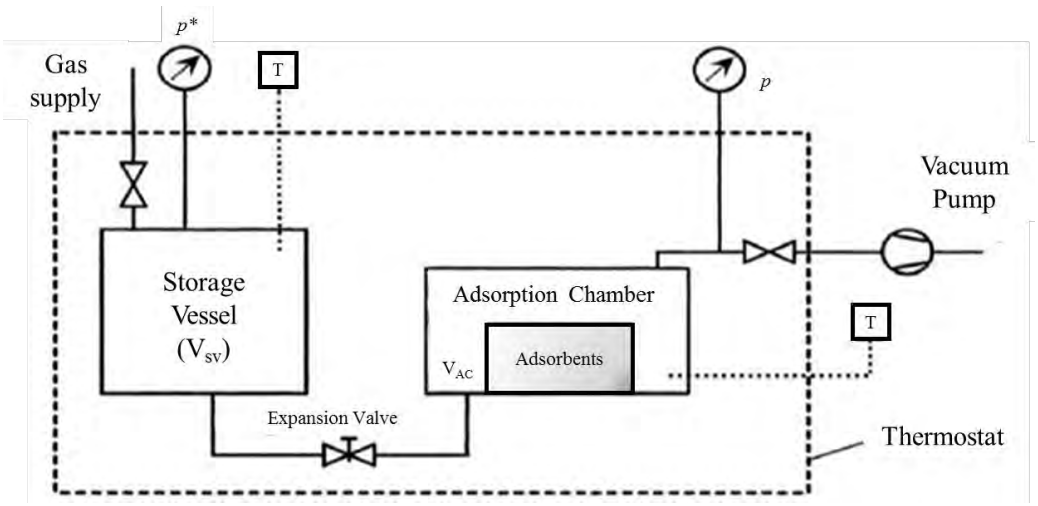

Figure 2.7 Experimental setup for volumetric measurement of pure gas adsorption equilibrium (Kumar, 2011).

2.5.2.3 Gas adsorption volumetric technique

In gravimetric method, the weight change of the adsorbent sample in the gravity field due to adsorption from the gas phase is recorded. Various types of sensitive microbalance have been developed for this purpose. A continuous-flow gravimetric technique coupled with wavelet rectification allows for higher precision, especially in the near-critical region. The line diagram of gravimetric apparatus is shown in Figure 2.8 (Kumar, 2011).

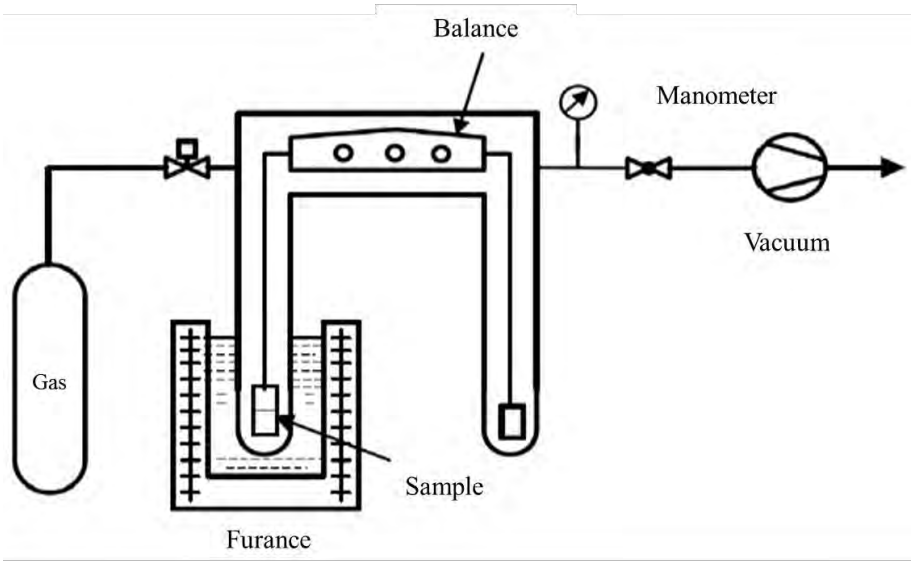

Figure 2.8 Schematic diagram of the gravimetric apparatus (Kumar, 2011).

2.6 Adsorbents

The process of storing methane through porous material is an important role for ANG technology. Typically, the porous adsorbents that have been studied in the previous research for methane adsorption are normally microporous: zeolites, activated carbons, porous organic polymer networks, and metal-organic frameworks (MOFs) (Shen *et al*., 2015). The good properties of adsorbents for natural gas storage are high microporous material with high packing density but minimizing macrospore and mesopore volume. But zeolites have limitation for methane adsorption because of their extremely hydrophilic, relatively low surface area (<1,000 m^2/g) leading to low methane adsorption capacity (Li *et al*., 2016). Activated carbon also has high packing density but difficult to tune pore shapes and sizes that has limited the utility. The adsorption capacity performance is measured at standard condition, which is the volume of adsorbed natural gas per volume of storage (V/V).

2.6.1 Activated Carbon

Activated carbon in its broadest sense is a term that includes a wide range of amorphous carbonaceous materials that exhibit a high degree of porosity and an extended inter-particulate surface area. They are obtained by combustion, partial combustion, or thermal decomposition of variety of carbonaceous substances such as coal, coconut shells, and wood. Activated carbons have been obtained in granular and powdered forms. They are now also being prepared in spherical, fibrous, and cloth forms for some applications. The granular form has a large internal surface area and small pores, and the finely divided powdered form is associated with lager pore diameters and a smaller internal surface area. Carbon cloth and fibrous activated carbon have a large surface area and contain a comparatively higher percentage of larger pores (Bansal and Goyal, 2005).

Carbon is the major constituent of activated carbons and is present to the extent of 85 to 95 percent. In addition, activated carbons contain other elements such as hydrogen, nitrogen, sulfur, and oxygen. These heteroatoms are derived from the source raw material or become associated with the carbon during activation and other preparation procedures. The elemental composition of typical activated carbon is 88 percent carbon, 0.5 percent nitrogen, 1 percent sulfur, and 6 to 7 percent oxygen, with the balance representing inorganic ash constituents. The oxygen content of activated carbon, however, may vary between 1 and 20 percent, depending upon the source raw material and the history of preparation, which includes activation and subsequent treatments. The most widely used activated carbon adsorbents have a specific surface area on the order of 800 to 1,500 m^2/g and pore volume on the order of 0.20 to 0.60 cm^3/g. The pore volume, however, has been found to be as large as 1 cm^3/g in many cases. The surface area in activated carbons is predominantly contained in micropores that have effective diameters smaller than 2 mm (Bansal and Goyal, 2005).

The major parameters of adsorbent for methane adsorption are porous structure and pore morphology. Because methane are more favourable to fill in micropores than in macropores and mesopores, the amount of micropores need to be maximized (Bagheri and Abedi, 2011). Simulations and experimental studies have indicated that activated carbon with slitshape pores 0.8-1.5 nm is the most suitable

for methane storage. The more micropores lead to the greater amount of methane being adsorbed. However, there are some existence of the mesopores and macropores in structure. These types of micropores also play a part in the methane storage capacities because they allow pass through to the micropores with higher pressure then they improve filling micropores for higher methane uptake (Li *et al*., 2016). There are many advantages of activated carbon as adsorbent from their strong resistance to alkalis and acids, good hydrophobicity, and excellent thermal stability at relatively high temperature. In addition, van der Waals forces is accepted to be an important role in adsorption of activated carbon (Bagheri and Abedi, 2011).

Activated carbons are mainly and almost exclusively prepared by the pyrolysis of carbonaceous raw material at temperatures lower than 1,000 °C. The preparation involves two main steps: carbonization of the raw material at temperatures below 800 °C in an inert atmosphere, and activation of the carbonized product between 950 to 1,000 °C. Thus, all carbonaceous materials can be converted into activated carbons, although the properties of the final product will be different, depending upon the nature of the raw material used, the nature of the activating agent, and the conditions of activation process. During carbonization, most of the non-carbon elements such as oxygen, hydrogen, nitrogen, and sulfur are eliminated as volatile gaseous products by the pyrolytic decomposition of the source raw material. The residual elementary carbon atoms group themselves into stacks, aromatic sheets cross-linked in a random manner. The mutual arrangement of these aromatic sheets is irregular and, therefore, leaves free interstices between the sheets, which may become filled with the tarry matter or the products of decomposition or at least blocked partially by disorganized carbon. These interstices give rise to pores that make activated carbons excellent adsorbents. The char produced after carbonization does not have a high adsorption capacity because of its less developed pore structure. This pore structure is further enhanced during the activation process when the spaces between the aromatic sheets are cleared of various carbonaceous compounds and disorganized carbon. The activation process converts the carbonized char into a form that contains the largest possible number of randomly distributed pores of various shapes and size, giving rise to a product with an extended and extremely high surface area. Activated carbons are produced in three main forms,

which are in granular, pelletized, and powdered forms as shown in Figure 2.9 (Bansal and Goyal, 2005).

Figure 2.9 Pelleted, granular, and powder activated carbon (from left to right) (www.redwhitechem.com).

2.6.2 Metal Organic Frameworks (MOFs)

Recently, metal organic frameworks (MOFs) have attracted a lot of interest for their adsorbent properties, among the wide range of other possible applications, such as drug delivery, catalyst, gas and liquid sorption. MOFs are highly tunable porous materials, where metal or metal-oxo clusters are connected via organic linkers to form three dimensional crystalline porous networks as shown in Figure 2.10 (Kumar *et al*., 2015). Because of their high porosity, high surface areas, large pore volumns, tunable pores, versatile chemistry, and ease of modulating functionalities in pore walls, porous MOFs have been studied and received extensive attention as an emerging class of crystalline materials containers for methane and natural gas storage in recent years. Several thematic reviews in this field have highlighted its rapid development. (Mason *et al*., 2014).

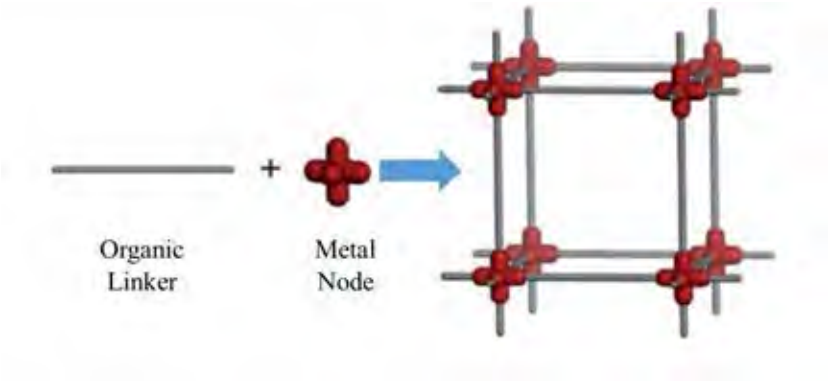

Figure 2.10 Simple framework connections of metal nodes and organic linkers for the construction of MOFs in a cubic topology (Kumar *et al*., 2015).

Different metal ions and organic linkers can be combined to be several species of MOFs. MOFs can be designed with different geometries like tetrahedral, trigonal, bipyramidal square or pyramidal octahedral. Metal ions are commonly Zn^{2+}, Al^{3+}, Ln^{3+}, etc. Organic linkers such as sulfonates, carboxylates, nitrites, phosphates, and amines also play a part in form of MOFs in Figure 2.11 (Kumar *et al*., 2015). Furthermore, coordination bonds have ability to rearrange the construction of MOFs by reversible process throughout polymerization. Thus, MOFs can possess highly formed framework structure.

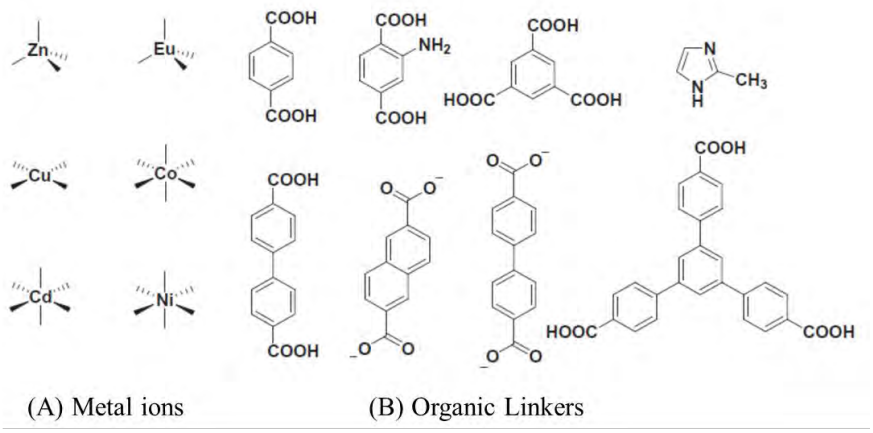

Figure 2.11 Example of the coordination geometry between (A) metal ions and (B) organic linkers used (in MOF synthesis) (Kumar *et al*., 2015).

Compared with porous zeolites, activated carbon materials, covalent organics frameworks (COFs), and porous organic polymers (POPs), the crystallize nature and ordered porosity of MOFs materials were studied for their in-depth structure-property relationships (Li *et al*., 2016). A variety of factors, including open metal sites, pore spaces, pore metrics (pore-size distribution), and framework densities of MOFs, have been demonstrated to greatly influence their methane storage performance.

Among this class of MOFs materials, a Zr-terephthalate based MOFs named UiO-66 (Zr). When UiO is abbreviated from University of Oslo, was selected in this study. It shows an exceptional stability, which allows its use in a wide range of thermal and chemical conditions. The key to its stability lies in the high topological connectivity of the $[Zr_6O_4(OH)_4]^{12+}$ secondary building unit (SBU), inorgnic nodes, which is connected with strong Zr-O bonds to 12 terephthalate (BDC) linkers, ligands. Crystalline structure of UiO-66 is presented in Figure 2.12 (Yang *et al*., 2011).

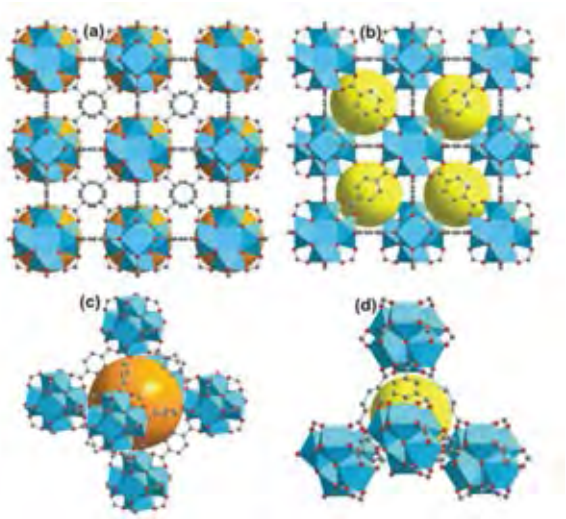

Figure 2.12 Schematic illustration of the UiO-66(Zr) structure. Left (a,c): octahedral cage; right (b,d): tetrahedral cages. Hydrogen atoms on the organic linkers were omitted for clarity. The large green spheres represent the void regions inside the cages (Zr polyhedra: yellow for octahedral cages, blue for tetrahedral cages; C, gray; O, red) (Yang *et al*., 2011).

Moreover, MIL-53 (Al) is the one class of MOFs which was obseved in this study. When MIL abbreviate from Materials of Institutute Lavoisier, was investigated in the experiment. MIL-53 composed with aluminum nitrate as the aluminium source in metal node and 1,4-benzenedicarboxylic acid (H_2-BDC) as the organic ligand. It has micopore volume and reversible structural changes due to the framework interaction with guest molecules which lead to MIL-53 can flexible struture for gas adsorption (Jiao *et al.*, 2017).

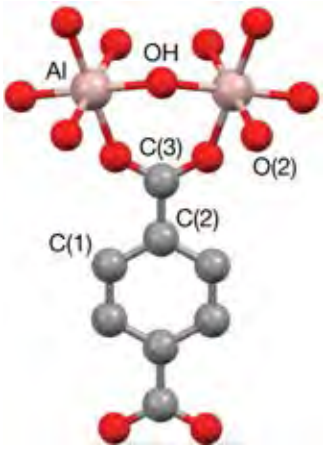

Figure 2.13 Labeling of MIL-53(Al)'s crystallographic structure (Mota *et al.*, 2017).

2.7 Literaure Reviews

In ANG storage, natural gas is adsorbed by a certain high porosity adsorbent material loaded into the storage container. ANG storage operates by enhancing the amount of gas stored when a large portion of gas adsorbs on the adsorbent and markedly improve the storage capacity at lower pressure. It takes place at relatively low pressure compare to CNG, which is around 3.5 MPa, achievable by single-stage compression with porous materials and can provide nearly the same capacity of CNG. Compared to CNG storage, the ANG storage stored 67% of the total amount storable with a vessel without adsorbent due to the storage space taken up by adsorbent mass but at 1/6 of its pressure. In other words, although ANG stores less

total storable amount of natural gas, but its storage pressure is 83% lower than CNG storage (Zakaria and George, 2011)

Bagheri and Abedi (2011) studied methane adsorption capacities on various corn cob based activated carbons at four different pressures (500, 1,000, 1,500 and 2,000 psi) and two different temperatures (298 and 323 K) in an adsorption apparatus. Six activated carbons were prepared at different production method (carbonization, mixing/filtration, solid/solid mixing and three impregnation) with various BET specific surface areas.

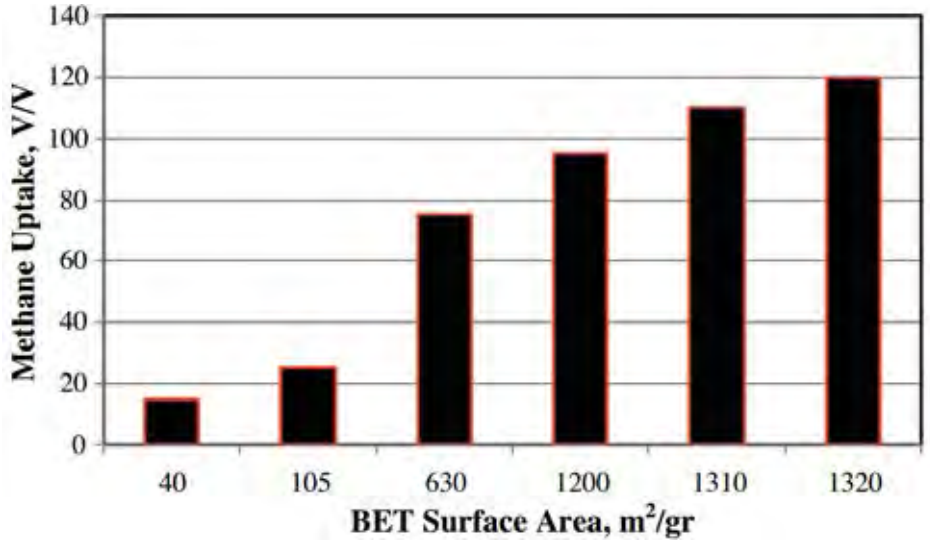

Figure 2.14 Variation of methane adsorption capacity with BET surface area, at a pressure of 500 psi and temperature of 298 K (Bagheri and Abedi, 2011).

As shown in Figure 2.14, the natural gas adsorption capacity depends on the BET specific surface area. It can be seen that the amount of natural gas adsorbed presented a dramatically increase at high BET specific surface area, indicating a higher micropore content. Increasing the BET specific surface area leads to greater natural gas adsorption capacity. This can best be described by the BET specific surface area, because of the creation of more micropores, which effectively increased the adsorption of natural gas. On increasing the pore width, the forces responsible for the adsorption decreased rapidly. Thus, pores larger than 2 nm (mesopores and macropores) are not useful for the enhancement of methane storage. Enhancing the

adsorption storage of methane, the fraction of micropores should be maximized, with no voids or macropore volume (Bagheri and Abedi, 2011).

In this application, the adsorption apparatus has been designed and set up to measure the prepared activated carbon adsorption property. The model is a laboratory volumetric system, in which the adsorption capacity of methane on activated carbon is obtained. The amount of methane adsorbed on the activated carbon was determined by using a volumetric method.

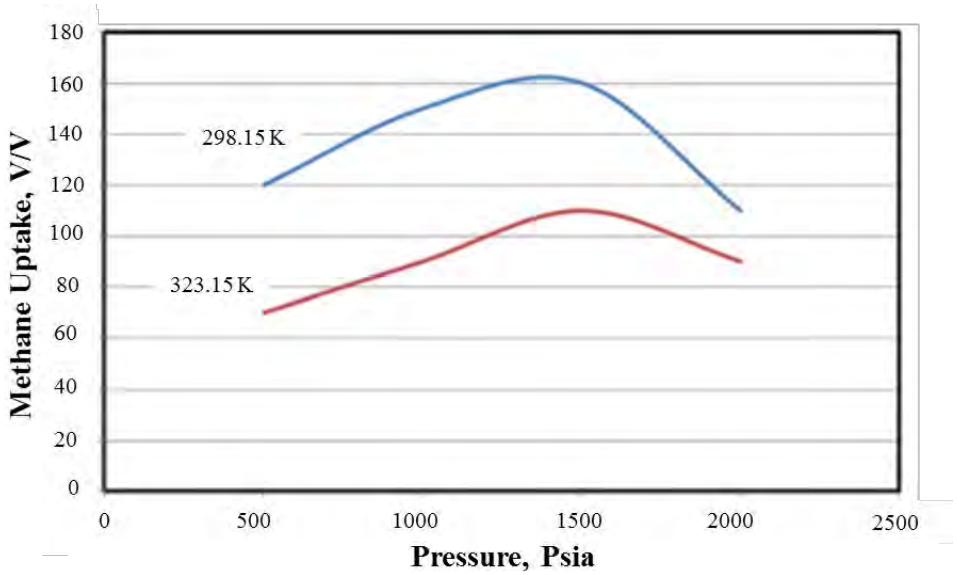

Figure 2.15 Variation of methane adsorption capacity with pressure at two different temperatures (Bagheri and Abedi, 2011).

Figure 2.15 presents the methane adsorption at various pressures and two different temperatures. It can be seen that increase of pressure, increases the amount of gas adsorbed. Therefore, increasing the pressure increases the Van der Waals attraction forces between the gas molecules and adsorbent surface. It is observed that the amount of adsorbed gas decreases in pressures over 1500 psi, which can be attributed to the saturation of the adsorbent bed or the destruction of micropores at high pressures. Because the adsorption is an exothermic process, increasing temperature results in a lower methane storage capacity, thermodynamic reason (Bagheri and Abedi, 2011).

Djeridi *et al*. (2017) reported about nanoporous carbon, which were synthesized by sol-gel method from mixing pyrogallol-formaldehyde with water and $HClO_4$ as catalyst. The adsorbent was pyrolyzed at 1,000 ºC, named PF-1000. Figure 2.16 (a) illustrates the adsorption isotherms for methane and carbon dioxide on PF-1000 at 302 K. The PF-1000 adsorbed carbon dioxide greater than methane. Similarly, heat of adsorption (ΔH_{ads}) of carbon dioxide is higher than heat of adsorption of methane, as illustrated in Figure 2.16 (b). It is interesting to compare the adsorption isotherms of carbon dioxide and methane because the quadrupole moment of carbon dioxide has a significant force, which induces specific interactions with adsorbent molecules (molecular orientation, hydrogen bonding and etc.) while methane has not. In addition, this reason can be explained by temperature of the experiment, 302 K, which is closer to the triple point temperature of carbon dioxide than that of methane. And also, the condition is slightly below the critical temperature of carbon dioxide (304.21 K), while methane is supercritical gas ($T_{c\ (CH4)}$ = 190.53 K). So, adsorption of carbon dioxide in these experimental conditions was favored.

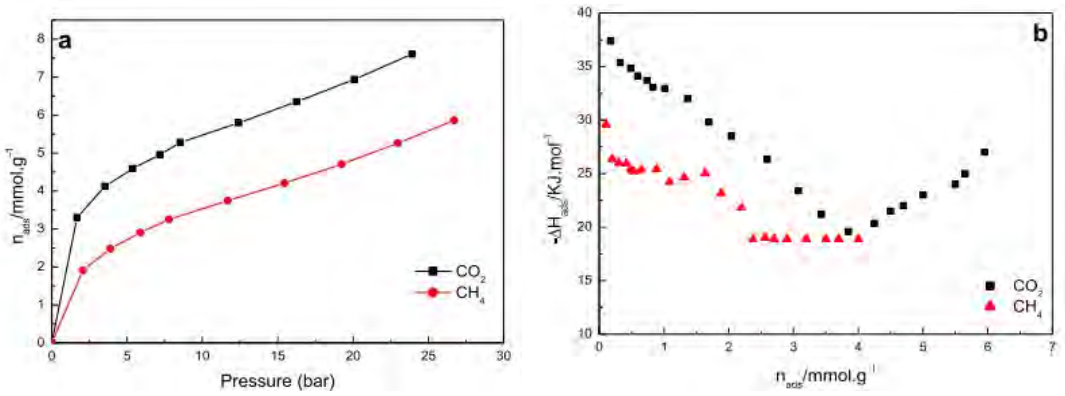

Figure 2.16 Adsorption isotherms (a) and adsorption enthalpy (b) of CO_2 and CH_4 at 302 K on the nanoporous carbon based on pyrogallol-formaldehyde (Djeridi *et al*., 2017).

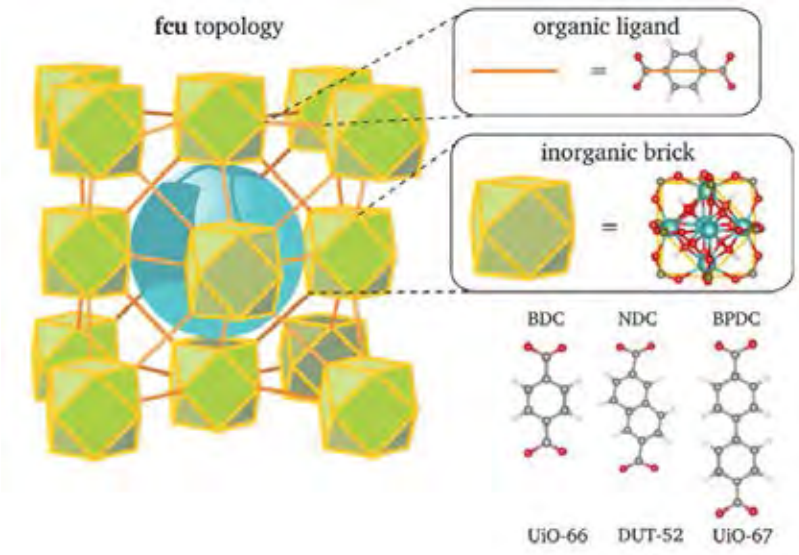

Figure 2.17 Depiction of the fcu topology which is shared by UiO-66, DUT-52, and UiO-67. Also the inorganic brick is common between these materials, which differ only in the organic linker. Zirconium atoms are shown in cyan, oxygen atoms in red, carbon atoms in grey, and hydrogen atoms in white (Vandenbrande *et al*,. 2017).

Vandenbrande *et al*. (2017) studied methane adsorption in the isoreticular, defect-free zirconium-based MOFs including UiO-66, UiO-67, and DUT-52. UiO-66, UiO-67 and DUT-52 are isoreticular, which uses a linker with the same geometry but different lengths. As the result, the crystal structures have the same connectivity (topology) but larger cystal is formed. Comparing different force fields in Zr-based MOFs for high pressure from 30 to 80 bar and room temperature, it was found that the maximum methane gravimetric loading was ordered as UiO-66 < DUT-52 < UiO-67, which was the same ordering as for the surface areas and pore volumes of these materials shown in Table 2.3.

Table 2.3 Geometric properties of the five Zr-Based MOFs considered in the qualitative comparison (Vandenbrande *et al*,. 2017)

	UiO-66	**UiO-67**	**DUT-52**
Density (g cm^{-3})	1.238	0.725	0.955
Pore Volume (cm^3 g^{-1})	0.40	0.87	0.62
Surface Area (m^2 g^{-1})	1,113	2,949	2,040
Small Pore Diameter (Å)	7.3	10.1	8.6
Large pore diameter (Å)	8.8	13.0	9.3

Rada *et al*. (2018) observed the effects of mixing BDC-NO_2 and BDC-NH_2 linkers in the synthesis of Zr-MOFs on their carbon dioxide and methane adsorption by using UiO-66 with single and binary linkers. These adsorbents were synthesized by solvothermal method, solvent exchanging with methanol to activate pore. The adsorption was carried out at 273 K and 0-1,200 KPa.

Table 2.4 BET surface area (Rada *et al*., 2018)

Sample	**BET Surface area (m^2/g)**
UiO-66-NO_2	771
UiO-66-NO_2-NH_2 10%	867
UiO-66-NO_2-NH_2 75%	788
UiO-66-NH_2	1,025
UiO-66-NH_2-NO_2 10%	1,152
UiO-66-NH_2-NO_2 75%	824

The BET surface areas of the samples by the t-plot method are presented in Table 2.4. The surface areas can be increased at 10% loading of a second linker but decreased with 75% loading of the functional linkers to UiO-66-NH_2 or UiO-66-NO_2.

UiO-66-NO_2-NH_2 10% and UiO-66-NH_2-NO_2 10% displayed higher surface areas than single linker functionalized samples, UiO-66-NO_2 and UiO-66-NH_2, respectively. More specifically, BDC-NO2 linker has the least favorable energy of structural assembly because of the electronegative -NO_2 group. Adding few amount of BDC-NH_2 linker enhance the formation of the structure of UiO-66-NO_2 and enhance the specific surface area as showed in UiO-66-NO_2-NH_2. On the other hand, NH_2-linker segregates itself from others because this linker can build hydrogen bonds with BDC-NH_2 itself. Therefore, adding few amount of BDC-NO_2 linker may attenuate the hydrogen bond insides the pores and at the same time enhance the microporosity of the materials, leading to the increase in the specific surface area as observed in UiO-66-NH_2-NO_2 10%.

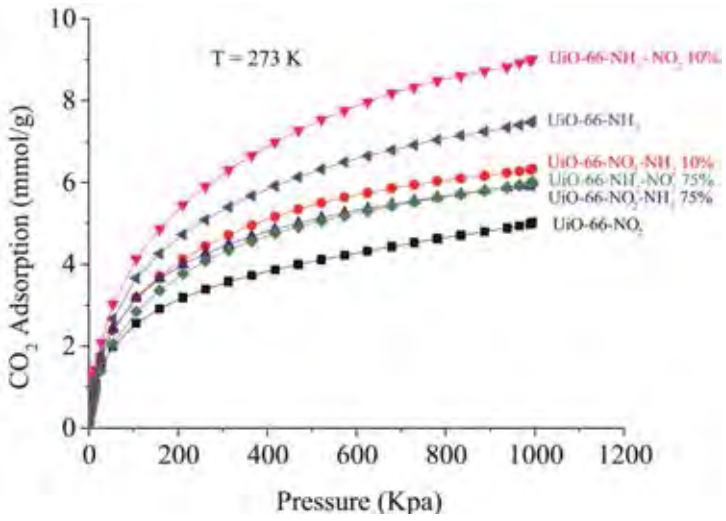

Figure 2.18 CO_2 adsorption on UiO-66-NO_2, UiO-66-NO_2- NH_2, UiO-66-NH_2-NO_2 and UiO-66-NH_2 samples at 273 K (Rada *et al*., 2018).

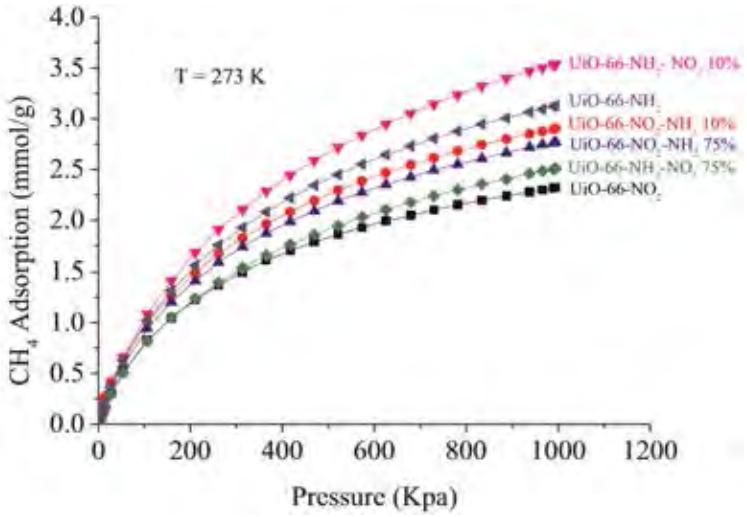

Figure 2.19 CH_4 adsorption on UiO-66-NO_2, UiO-66-NO_2- NH_2, UiO-66-NH_2-NO_2 and UiO-66-NH_2 samples at 273 K (Rada *et al*., 2018).

Figures 2.18 and 2.19 showed methane and carbon dioxide adsorption isotherms on all samples. In general, all samples had selectivity to adsorb carbon dioxide higher than methane because the carbon dioxide molecule had dipole-quadrupole interaction with Lewis sites on the adsorbent surface which creates strong interactions. For single linker on UiO-66, UiO-66-NH_2 showed higher methane and carbon dioxide adsorption than UiO-66-NO_2. Due to the effect of surface area, the higher surface area showed the higher both methane and carbon dioxide adsorption. (Rada *et al*., 2018).

Rada *et al*. (2015) examined adsorption of methane and carbon dioxide gases and carbon dioxide over methane selectivity on titanium based MOFs (Ti-based MOFs) such as MIL-125(Ti), NH2-MIL-125(Ti) and MIX-MIL-125(Ti) at high pressures up to 10 bar and temperature of 298 K. The effects of double linkers in the synthesis process and addition of amino-functionalised linker in the structure on adsorption of carbon dioxide and methane have been investigated.

From the characterization results shown in Table 2.4 that MIX-MIL-125(Ti) gives a twice BET surface area value as MIL-125(Ti), which suggests that a small portion of H_2BDC-NH_2 provides much more connection sites with metals. In terms of micropore portion, MIL-125(Ti), MIX-MIL-125(Ti) and NH_2-MIL-125(Ti) has

51%, 73% and 90% of total pore area, respectively. MIL-125(Ti) has the highest average pore size. Therefore, amino group will reduce pore size of MIL-125(Ti).

Table 2.5 Porous structure of MIL-125(Ti), NH_2-MIL-125(Ti) and MIX-MIL-125(Ti) samples (Rada *et al*., 2015)

Sample	S_{BET} (m^2/g)	Micropore Volume (cm^3/g)	Micropore area% (t-plot method)
MIL-125(Ti)	714	0.16	51.5%
NH_2-MIL-125(Ti)	1,488	0.37	73.2%
MIX-MIL-125(Ti)	1,660	0.57	90.1%

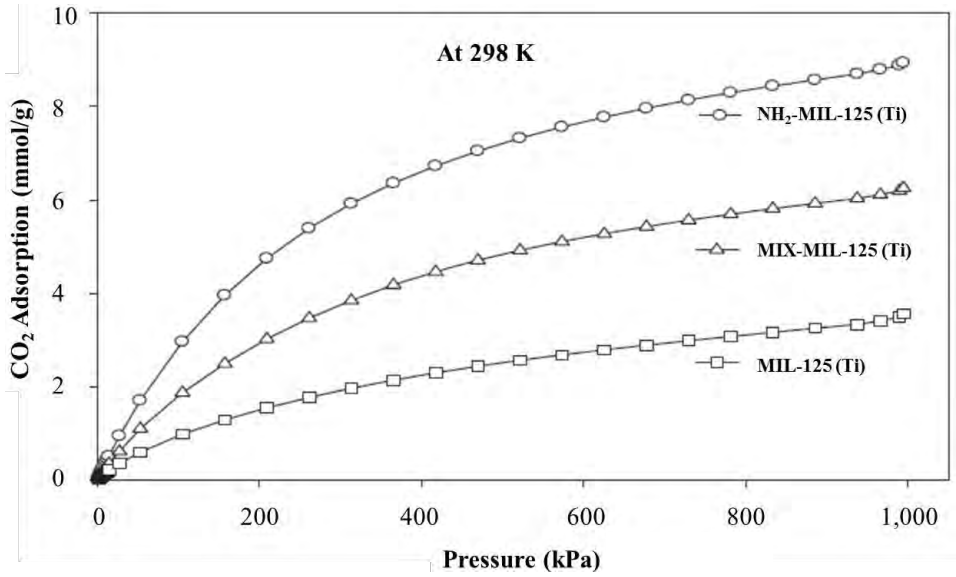

Figure 2.20 CO_2 adsorption on MIL-125(Ti), NH_2-MIL-125(Ti) and MIX-MIL-125(Ti) at 298 K (Rada *et al*., 2015).

Figure 2.20 shows that the highest carbon dioxide uptake was achieved on NH_2-MIL-125(Ti) and followed by MIX-MIL-125(Ti) and MIL-125(Ti). Adding amino-functional group to MIL-125(Ti) using mixed linkers can lead to more surface area and sites for carbon dioxide uptake. Moreover, it is believed that the amino groups also increase the affinity toward carbon dioxide adsorption. Similarly, in

Figure 2.21, NH_2-MIL-125(Ti) presented the highest methane adsorption capacity. In addition, MIX-MIL-125(Ti) sample exhibited higher methane uptake thanMIL-125(Ti). This could be attributed to higher surface area of MIX-MIL-125(Ti) sample which has been gained by using mixed linkers system into the structure of MIL-125(Ti).

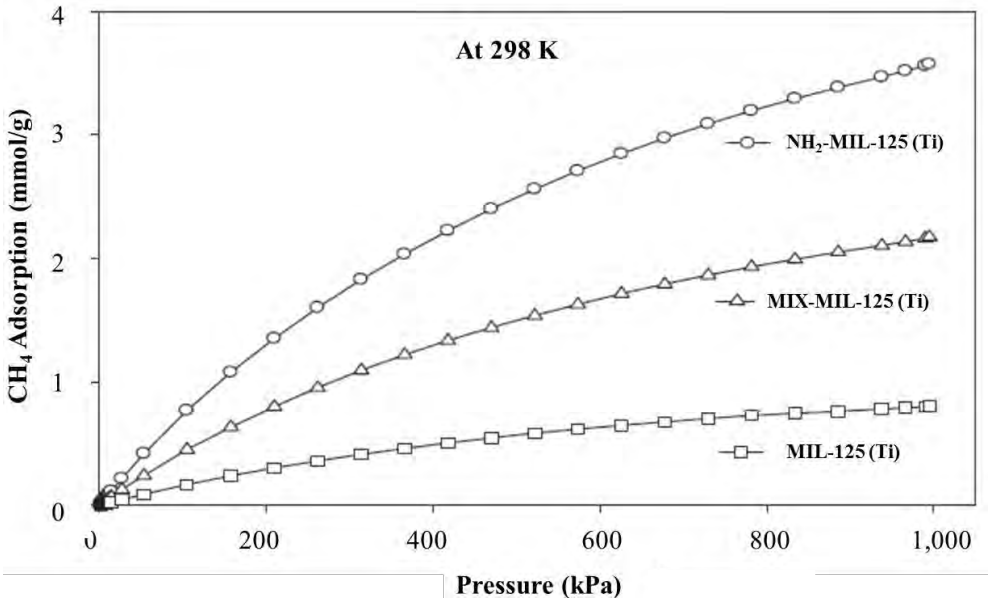

Figure 2.21 CH_4 adsorption on MIL-125(Ti), NH_2-MIL-125(Ti) and MIX-MIL-125(Ti) at 298 K (Rada *et al*., 2015).

Selectivities of carbon dioxide over methane is shown in Figure 2.22. It can be seen that MIL-125(Ti) shown the best selection for carbon dioxide over methane, meanwhile NH_2-MIL-125(Ti) had the lowest separation. Moreover, selectivity of carbon dioxide over methane drops sharply as gas pressure increases. The significant separation of carbon dioxide on all samples occured at pressures lower than 200 kPa. The highest carbon dioxide over methane selectivity in MIL-125(Ti) could be the highest mesopores, which enhanceed the adsorption of carbon dioxide more than methane. Meanwhile, interconnecting pores in microporous materials such as NH_2-MIL-125(Ti) and MIX-MIL-125(Ti) can enhance methane uptake.

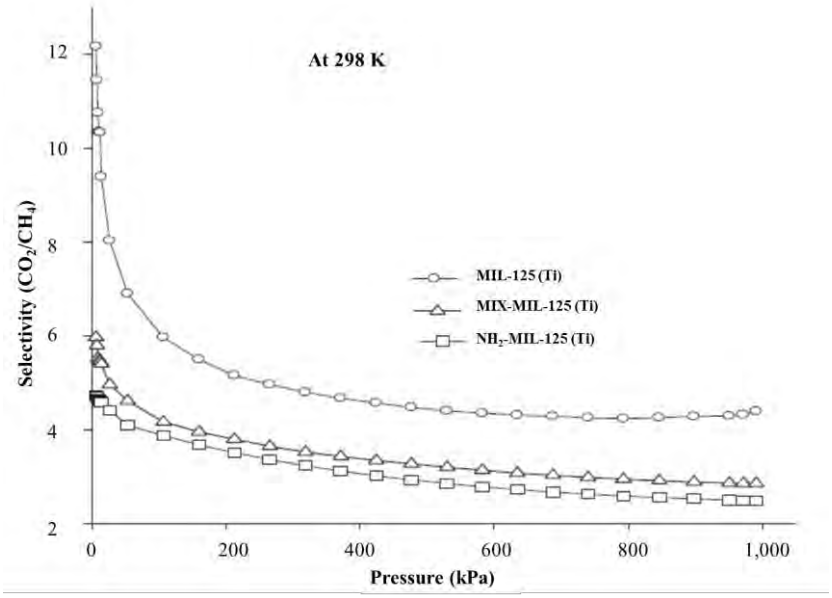

Figure 2.22 Selectivities of CO_2/CH_4 at varying pressures and 298 K (Rada *et al*., 2015).

Beckner and Dailly (2016) studied the comparison of methane storage in two metal organic frameworks ($Cu_3(btc)_2$ and Al(OH) Fumarate) and activated carbon was observed. These adsorbents represent a diverse variety of pore structures and surface chemistries. All materials were in small granular form. The excess adsorption, skeletal density, bulk density, and porosity were disscussed. Volumetric storage capacities are effected by excess adsorption, skeleton density and bulk density but the bulk density is also influenced by inter-granular porosity and intra-granular porosity. Because the skeletal density and excess adsorption are specific properties of the material and are steady with moderate compaction of the powder. Thus, the volumetric storage capacities can be improved by increasing the bulk density. From Figure 2.23, it is a decomposition of the volumetric storage with pressure of different materials. The green line is overall methane density that increases with increasing pressure. At low pressure, the volumetric storage capacity is dominated by excess adsorption. When the pressure increases, the excess adsorption get to the maximum, and finally the volumetric storage density is dominated by the contribution from the inter-granular or intra-granular porosity.

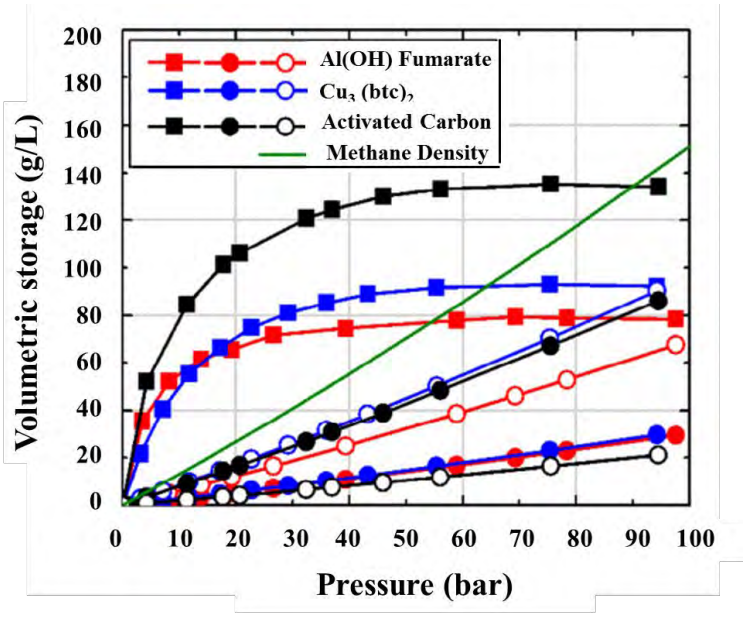

Figure 2.23 A decomposition of the volumetric storage for comparing the relative contributions of the excess adsorption (solid square), the intra-granular porosity (solid circles), and the inter-granular porosity (open circles) (Beckner and Dailly, 2016).

Because of bulk density and skeletal density result in a volumetric storage, adsorbent with high bulk density and high skeletal density lead to high volumetric storage. Therefore**,** activated carbon was expected to be the highest volumetric storage because of high bulk density and high skeletal density from their experiments while Al(OH) Fumulate is only high for bulk density, and $Cu_3(btc)_2$ is only high for skeletal density as shown in Table 2.5. However, when they consider for improving the bulk density. The inter-granular porosity becomes important. The larger inter-granular porosity, the better bulk density can be modified than the based material. The upper limit to the bulk density presents that inter-granular porosity becomes zero and intra-granular porosity becomes larger from densification. From their experiments, it shows that both MOFs have a much larger inter-granular porosity (0.5) than the AC (0.15) indicating that they can be most modified by densification (Beckner and Dailly, 2016).

Table 2.6 Density and porosity measurements summary (Beckner and Dailly, 2016)

Property	Activated Carbon	Al(OH) Fumurate	$Cu_3(btc)_2$
Skeletal density (g/cm^3)	2.2	1.7	2.5
Bulk density (g/cm^3)	0.54	0.57	0.37
Intra-granular pore volume (cm^3/g)	1.13	0.35	0.57
Inter-granular porosity	0.15	0.46	0.64
Intra-granular porosity	0.61	0.20	0.21

From Figure 2.24, slightly change can be seen for the AC, which has the smallest undensified inter-granular porosity. For the Al(OH) Fumarate, there is also only a small change upon maximum densification. This is mostly because Al(OH) Fumurate has a small pore volume. Thus, even though adsorbent is high inter-granular porosity, improvement of bulk density is limited by small pore volume. The $Cu_3(btc)_2$ becomes the most promising for densification. The maximally densified material is approximate to be able to store nearly twice the methane at 50 bar than the undensified material.

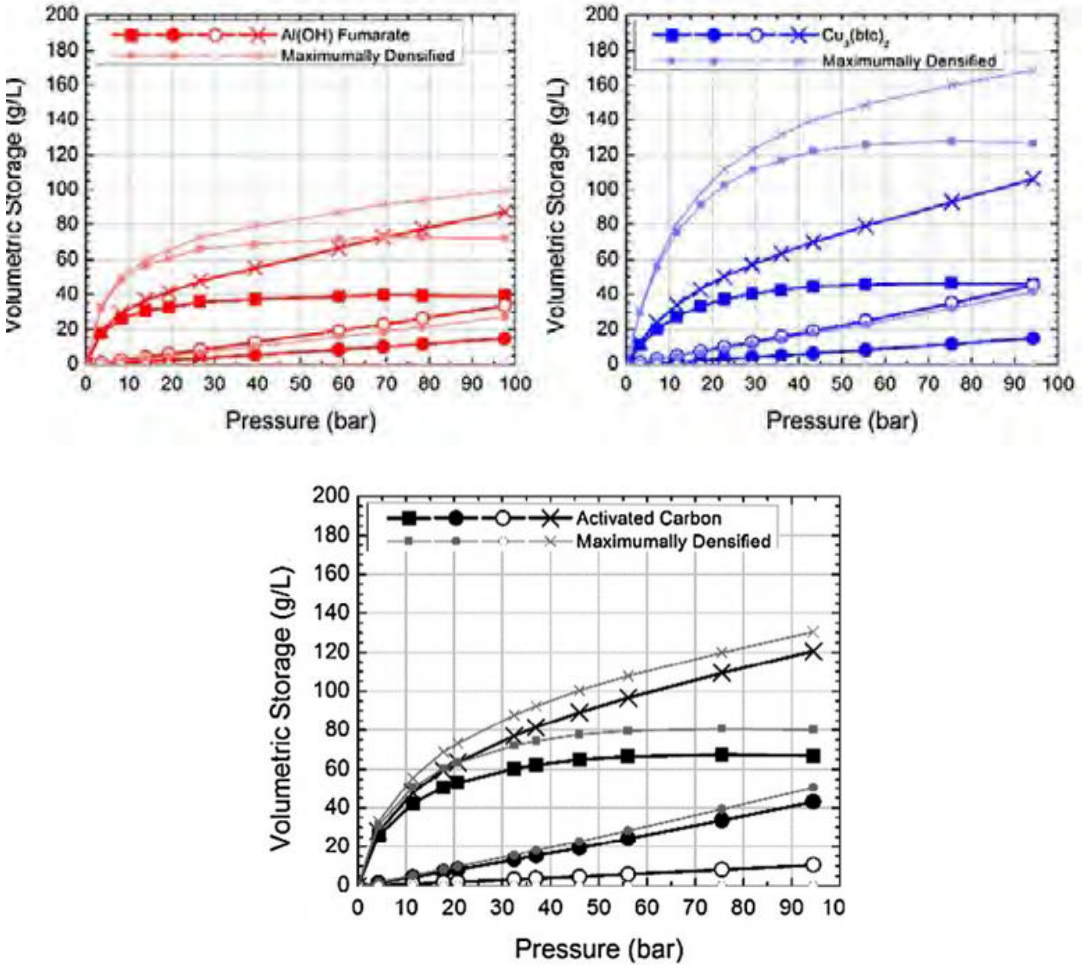

Figure 2.24 A comparison of the contributions to the total volumetric storage (X symbols) from the excess adsorption (square symbols), intra-granular porosity (solid circles), and inter-granular porosity (open cycles) for the maximally densified materials (Beckner and Dailly, 2016).

CHAPTER III
EXPERIMENTAL

3.1 Chemicals and Materials

3.1.1 Chemicals

- Terephthalic acid
- 2-aminoterephthalic acid
- 2-sodiumterephthalate acid
- Zirconium chloride octahydrate
- Aluminium nitrate nanohydrate
- Aluminium chloride hexahydrate
- Acetic acid
- Dimethylformamide (DMF)
- Methanol
- NaOH

3.1.2 Materials

- Fittings and valves
- Mass flow controller
- Vacuum pump
- Data logger
- Thermometer
- UiO-66, UiO-66-NH_2 25%, UiO-66-NH_2 50%, UiO-66-NH_2 75%, and UiO-66-NH_2 (The percent behind of UiO-66-NH_2 indicates the amount of amino linker mixed with UiO-66) (supported by NANOTEC, Thailand)
- MIL-53(Al) and MIL-53(Al)-NH_2 (supported by NANOTEC, Thailand)
- Methane gas (99.99% purity purchased from Labgaz Thailand Co., Ltd.)

- Carbon dioxide gas (99.99% purity purchased from Labgaz Thailand Co., Ltd.)
- Helium gas (99.99% purity purchased from Praxair Inc., Thailand)

3.2 Equipment

- Volumetric apparatus
- Fourier transform infrared spectroscope (FTIR), Nicolet 6700
- Scanning electron microscope (SEM), Hitachi SU8230
- Surface area analyzer (SAA), Quantachrom NovaWin/Autosorb 1-MP
- X-ray diffraction (XRD), Brucker D8 Advance

3.3 Methodology

3.3.1 Adsorbents Synthesis

Several batches of UiO-66, UiO-66-NH_2 25%, UiO-66-NH_2 50%, UiO-66-NH_2 75%, UiO-66-NH_2, MIL-53(Al), and MIL-53(Al)-NH_2 solids were prepared using solvothermal method.

3.3.1.1 UiO-66

- Dissolve zirconium chloride octahydrate (metal) 1,100 mg in 250 ml dimethylformamide (DMF), and terephthalic acid (organic linker, H_2-BDC) 570 mg was dissolved in 250 ml DMF.
- 200 ml acetic acid to the metal solution and stir until a homogeneous solution was obtained.
- Add a linker solution to the metal solution in a closed round-bottom flask and stir for 24 hours at 130 ^oC.
- Cool the solution naturally at room temperature. The sample in liquid solvent was centrifuged and washed with fresh DMF three times to eliminate remaining linker.

- The sample was purified with methanol for 12 hours several times to make sure that the occluded DMF was eliminated.
- Dry in an oven at 80 ºC for three days

3.3.1.2 UiO-66-NH_2 25%

- Dissolve zirconium chloride octahydrate 1,100 mg in 250 ml DMF, and 155 mg 2-amino-terephthalic acid (organic linker, NH_2-BDC) combined with 427 mg terephthalic acid (H_2-BDC) were dissolved in 250 ml DMF.
- 300 ml acetic acid to the metal solution and stir until a homogeneous solution was obtained.
- Add a linker solution to the metal solution in a closed round-bottom flask and stir for 24 hours at 130 ºC.
- Cool the solution naturally at room temperature. The sample in liquid solvent was centrifuged and washed with fresh DMF three times to eliminate remaining linker.
- The sample was purified with methanol for 12 hours several times to make sure that the occluded DMF was eliminated.
- Dry in an oven at 80 ºC for three days

3.3.1.3 UiO-66-NH_2 50%

- Dissolve zirconium chloride octahydrate 1,100 mg in 250 ml DMF, and 310 mg NH_2-BDC combined with 285 mg H_2-BDC were dissolved in 250 ml DMF.
- 300 ml acetic acid to the metal solution and stir until a homogeneous solution was obtained.
- Add a linker solution to the metal solution in a closed round-bottom flask and stir for 24 hours at 130 ºC.
- Cool the solution naturally at room temperature. The sample in liquid solvent was centrifuged and washed with fresh DMF three times to eliminate remaining linker.
- The sample was purified with methanol for 12 hours several times to make sure that the occluded DMF was eliminated.

- Dry in an oven at 80 ºC for three days

3.3.1.4 UiO-66-NH_2 75%

- Dissolve zirconium chloride octahydrate 1,100 mg in 250 ml DMF, and 465 mg NH_2-BDC combined with 145 mg H_2-BDC were dissolved in 250 ml DMF.
- 300 ml acetic acid to the metal solution and stir until a homogeneous solution was obtained.
- Add a linker solution to the metal solution in a closed round-bottom flask and stir for 24 hours at 130 ºC.
- Cool the solution naturally at room temperature. The sample in liquid solvent was centrifuged and washed with fresh DMF three times to eliminate remaining linker.
- The sample was purified with methanol for 12 hours several times to make sure that the occluded DMF was eliminated.
- Dry in an oven at 80 ºC for three days

3.3.1.5 UiO-66-NH_2

- Dissolve zirconium chloride octahydrate 550 mg in 250 ml DMF, and NH_2-BDC 310 mg dissolve in 250 ml DMF.
- 150 ml acetic acid to the metal solution and stir until a homogeneous solution was obtained.
- Add a linker solution to the metal solution in a closed round-bottom flask and stir for 24 hours at 130 ºC.
- Cool the solution naturally at room temperature. The sample in liquid solvent was centrifuged and washed with fresh DMF three times to eliminate remaining linker.
- The sample was purified with methanol for 12 hours several times to make sure that the occluded DMF was eliminated.
- Dry in an oven at 80 ºC for three days

3.3.1.6 MIL-53(Al)

- Dissolve aluminium nitrate nanohydrate (metal) 3,000 mg in 5,760 ml deionized water under stirring at room temperature.

- A clear solution of 8,400 mg 2-sodiumterephthalate acid (Na_2-BDC) mixed with 4,000 mg H_2-BDC in 5,760 ml deionized water was added over aluminuim solution.
- Such addition provoked the immediate appearance of a white precipitate. The mixture was maintaining under stirring at room temperature for 7 days.
- The sample in liquid solvent was centrifuged.
- The white precipitate was washed with distilled water repeatedly and dried at room temperature overnight.
- Dried sample was boiled with fresh DMF at 150^{o}C to treat and remove H_2-BDC filling the pores of the MOF structure.
- Centrifuge and calcine sample at 330^{o}C for 3 days at air atmosphere.

3.3.1.6 MIL-53(Al)-NH_2

- Dissolve aluminium chloride hexahydrate (metal) 500 mg in 2 ml deionized water.
- An aqueous yellow solution was prepared by dissolving in 3 ml of deionized water : 375 mg NH_2-BDC mixed with 179 mg NaOH.
- Add aluminium solution over aqueous yellow solution under sterring, leading to the immediate appearance of yellow solid, which became a gel-like mixture. Stir at room temperature for 1 day.
- The yellow solid was recovered from the mixture by centrifugation and washed it with deionized water several times and dried at room temperature overnight.
- Dried sample was boiled with fresh DMF at 150 ^{o}C to treat and remove NH_2-BDC filling the pores of the MOF structure.
- Centrifuge and calcine sample at 330^{o}C for 3 days at air atmosphere.

3.3.2 Adsorbent Characterization

- The surface area, total pore volume, and pore size distribution of the adsorbents were measured by a Quantachrom/Nova 2000e instrument. The adsorbents were first out gassed to remove the humidity on its surface under vacuum at 200 °C for 12 hours prior to the analysis. After that, nitrogen was purged to adsorb on its surface. The volume-pressure data was used to calculate the Brunauer-Emmett-Teller (BET) surface area, pore volume, and pore size distribution.
- The morphology of the adsorbents was investigated by using the SEM, Hitachi SU8230, with an accelerating voltage of 2 kV. The adsorbents were coated with gold under vacuum condition before observation.
- Fourier transform infrared spectroscopy (FTIR) was used to qualitatively evaluate the chemical structure of the adsorbents. The IR spectra was collected using a Nicolet, 6700 FT-IR spectrometer. The adsorbent samples were grounded into fine powder and mixed with KBr. The mixture was used for the preparation of KBr pellets. The IR spectrum was obtained over a frequency between 400 and 4,000 cm^{-1}.
- X-ray diffraction was used to confirm the crystalline structure of metal organic frameworks. It was carried out with a diffractometer Bruker D8 Advance using Cu Kα radiation (scan range 5° to 45°).
- Nitrogen composition products in adsorbent were analyzed by CHN/O analyser, LECO CHN628, LECO, USA.

3.3.3 Adsorption and Measurement

The schematic of the experimental set-up is shown in Figure 3.1. A pressure transmitter was installed to measure pressure of the system. 0.3 gram of the prepared adsorbent was loaded into the stainless-steel adsorption chamber, which was heated by the furnace in order to reach the adsorption temperatures. He (Ultra high purity, Praxair Inc.) was used as a purge gas in this study. The adsorption was carried out using high purity carbon dioxide gas (99.99%). Effects of adsorption temperature were investigated by heating up to the temperature at room temperature, 33 °C within a pressure range of 0-100 psi. The temperature of the adsorption chamber was adjusted and maintained by an internal temperature sensor.

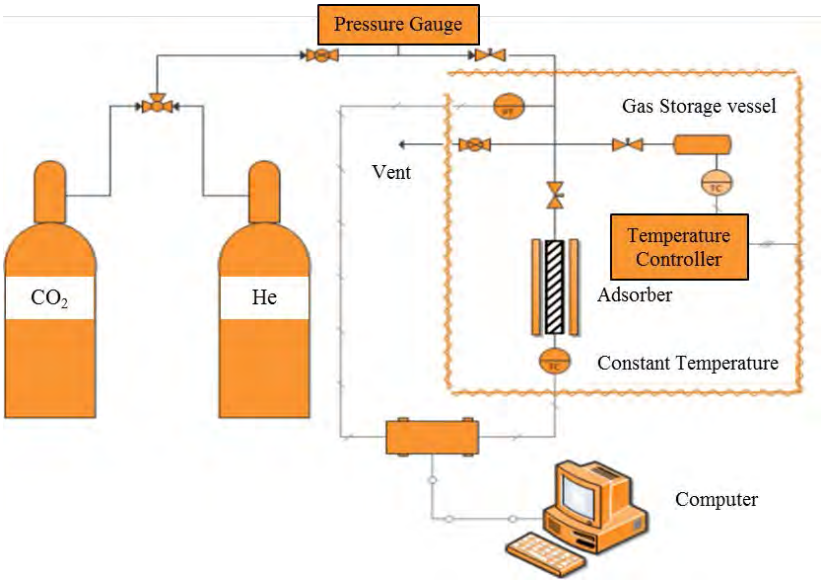

Figure 3.1 Schematic of the experimental set-up for the equilibrium adsorption of carbon dioxide.

The volumetric apparatus was used to study methane adsorption on adsorbents. This apparatus consisted of a sample holder, a vacuum pump, and pressure transducer. Ultra-high purity grade methane (99.99 % purity) was used in the adsorption study. The schematic diagram of volumetric apparatus for this research is shown in Figure 3.1

A gas reservoir was a high pressure stainless steel reactor, and the pressure regulator with 4,000 psig maximum limit was installed to control a gas flow rate into the system. A K-type thermocouple was used for measuring the temperature of gas inside the reactor. The system pressure was measure by pressure transducer in the range of 0 to 3,000 psig with 0.13% error.

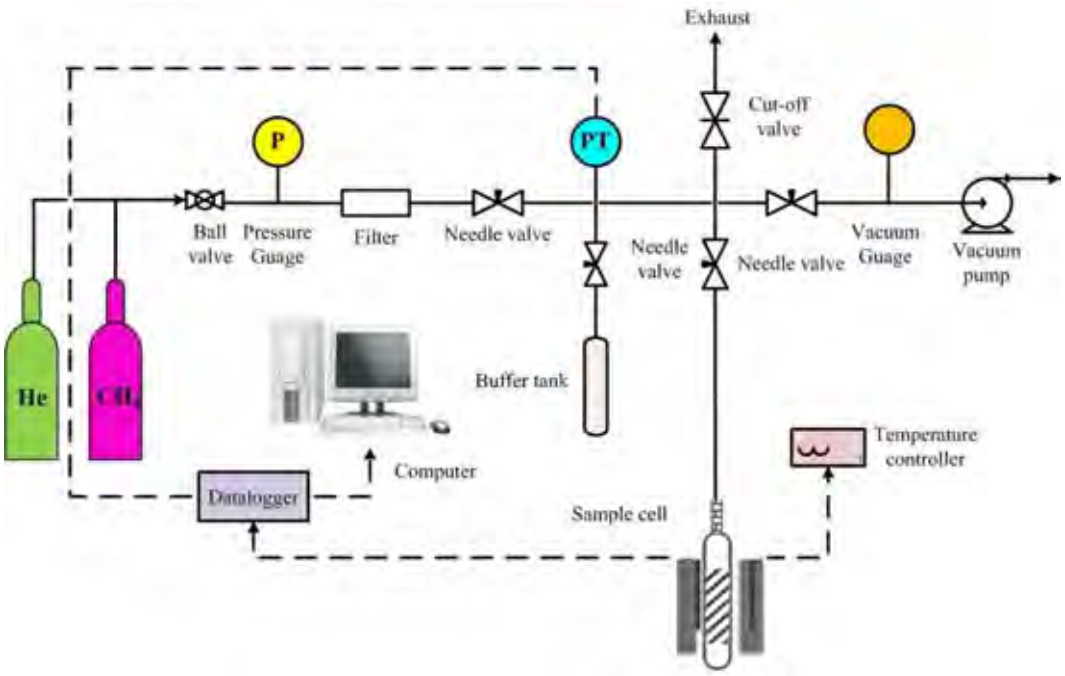

Figure 3.2 Schematic of the experimental set-up for the equilibrium adsorption of methane.

3.3.4 Gas Adsorption Calculation

The amount of methane and carbon dioxide adsorption was determined by using Equation 3.1.

$$n_i = \frac{1}{W}\left(\frac{P_1(V_1+V_2)}{ZRT} - \frac{P_2(V_1+V_2)}{ZRT}\right) \quad (3.1)$$

where n_i = Mole of adsorbed methane and carbon dioxide (mole)

P_1 = Pressure of the system before equilibrium (atm)

P_2 = Pressure of the system after equilibrium (atm)

V_1 = Volume of a manifold (cm^3)

V_2 = Volume of a cylinder with adsorbent (cm^3)

Z = Compressibility factor

R = 82.05 (cm^3atm/mol K)

T = Temperature of the sample (K)

W = Weight of adsorbent (g)

The pressure transducer was calibrated for every adsorption experiment. The vacuum pressure of -14.7 psi was used as the reference pressure. With this pressure, the relative was set to zero under vacuum condition.

3.3.4.1 Determination of the sample holder volume using helium

The volume of the sample holder was determined by helium expansion at 30°C, based on the assumption that no helium was adsorbed on the adsorbents. The pressures before and after each helium expansion were recorded.

To calculate the volume of instrument after helium expansion, V_2, Ideal Gas Law was used as followes Equation 3.2.

$$\frac{P_1V_1}{T_1} = \frac{P_2V_2}{T_2} \tag{3.2}$$

where P_1 = Pressure of helium before helium expansion

V_1 = Volume of the system excluding volume of sample holder

T_1 = Temperature before helium expansion

P_2 = Pressure of helium after helium expansion

V_2 = Total system volume = $V_1 + V_{\text{sample holder}}$

T_2 = Temperature after helium expansion

3.3.4.2 Determination of the methane and carbon dioxide adsorption on adsorbents

Determination of the methane and carbon dioxide adsorption was carried out at different constant temperatures; room temperature (33 °C) and pressure up to 100 psia for methane and carbon dioxide. Temperature was adjusted to room temperature (33 °C). At desired pressure, methane or carbon dioxide was introduced from a high pressure cylinder into a sample holder. During the experiment,

the time to reach the equilibrium of methane and carbon dioxide adsorption was within approximately 20 and 30 min, respectively. The methane and carbon dioxide pressures were recorded before and after each methane expansion.

The ideal gas law and conservation of mass were also used for determining the amount of methane and carbon dioxide adsorbed on the adsorbents. The amounts of methane and carbon dioxide adsorbed by Zr-baesd MOFs and Al-based MOFs can be obtained by the following Equation 3.3.

$$n_{ad} = n_{ad-1} + \frac{P_1(V_1)}{ZRT_1} - \frac{P_{f-1}(V_2)}{ZRT_{f-1}} - \frac{P_f\left(V_1/V_2\right)}{ZRT_f} \quad (3.3)$$

where n_{ad} = Total amount methane and carbon dioxide adsorbed by Zr-baesd MOFs and Al-based MOFs (mole)

n_{ad-1} = Amount methane and carbon dioxide adsorbed at previous stage (mole)

P_i = Initial pressure of methane and carbon dioxide before methane and carbon dioxide expansion into the sample holder (psia)

P_{f-1} = Final pressure of methane and carbon dioxide after methane and carbon dioxide expansion into the sample holder in the previous stage (psia)

P_f = Final pressure of methane and carbon dioxide after methane and carbon dioxide expansion into the sample holder (psia)

V_1 = Volume of manifold excluding volume of sample holder (cm^3)

V_2 = Volume of the sample holder (cm^3)

Z = Compressibility factor of methane and carbon dioxide

T_i = Initial temperature of methane and carbon dioxide before methane and carbon dioxide expansion into the sample holder (K)

T_f = Final temperature of methane and carbon dioxide before methane and carbon dioxide expansion into the sample holder (K)

T_{f-1} = Final temperature of methane and carbon dioxide before methane and carbon dioxide expansion into the sample holder in the previous stage (K)

R = Gas constant, 82.0578 atm·cm^3/mol·K

3.3.5 Modelling of Adsorption Isotherms

3.3.5.1 Langmuir isotherm

Langmuir isotherm which was primarily designed to describe gas-solid phase adsorption is also used to quantify and contrast the adsorptive capacity of various adsorbents. Langmuir isotherm accounts for the surface coverage by balancing the relative rates of adsorption and desorption. Adsorption is proportional to the fraction of the surface of the adsorbent that is open while desorption is proportional to the fraction of the adsorbent surface that is covered as shown in Equation 3.4.

$$q_e = \frac{QbP}{(1+bP)} \tag{3.4}$$

where q_e = Mole of adsorbate adsorbed per unit mass of Zr-baesd MOFs and Al-based MOFs (mmol/g)

Q = Maximum adsorbed phase concentration (mmol/g)

P = Equilibrium pressure (psia)

b = Langmuir constant

3.3.5.2 Freundlich isotherm

Freundlich Isotherm is applicable to adsorption processes that occur on heterogonous surfaces. As shown in Equation 3.5, this isotherm gives an expression which defines the surface heterogeneity and the distribution of active sites and their energies.

$$q_e = K_F P^{1/n} \tag{3.5}$$

where q_e = Mole of adsorbate adsorbed per unit mass of Zr-baesd MOFs and Al-based MOFs (mmol/g)

P = Equilibrium pressure (psia)

K_F = Freundlich constant

n_F = Freundlich exponent

3.3.5.3 Sips isotherm

Sips isotherm is a combination of the Langmuir and Freundlich isotherms and it is given as the following Equation 3.6.

$$q_e = \frac{Q(K_S P)^Y}{(1+(K_S P)^Y)} \tag{3.6}$$

where q_e = Mole of adsorbate adsorbed per unit mass of Zr-baesd MOFs and Al-based MOFs (mmol/g)

Q = Maximum adsorbed phase concentration (mmol/g)

P = Equilibrium pressure (psia)

K_S = Sips constant

Y = Sips exponent

CHAPTER IV
RESULTS AND DISCUSSION

4.1 Adsorbent Characterization

In this study, Zr-based MOFs and Al-based MOFs adsorbents, UiO-66, UiO-66-NH_2 25%, UiO-66-NH_2 50%, UiO-66-NH_2 75%, UiO-66-NH_2, MIL-53(Al), and MIL-53(Al)-NH_2 were used. Note that UiO-66-NH_2 indicates the change (100% loading) of organic linker from terephthalic acid to 2-aminoterepthalic acid, while 25%, 50%, and 75% after UiO-66-NH_2 are wt% of 2-aminoterepthalic acid used to replace terephthalic acid in the structure. The adsorbed crystalline structure was examined by an XRD diffractometer (D8 Advance-diffractometer Brucker) with Cu Kα radiation. A FTIR spectrometer (Nicolet 6700 FT-IR spectrometer) was used to confirm functional groups on Zr-based MOFs and Al-based MOFs crystalline structure. The spectrum was scanned from 400 to 4000 cm^{-1}. A SEM (Hitachi SU8230) was used to investigate the morphologies of the samples. Surface area and pore size of each sample were measured. All samples were degassed under vacuum overnight and then N_2 adsorption at -196 °C by Nova 2000e (Quantachrome Instrument) was carried out. The degassing of the adsorbents was previously performed at 200 °C for 12 h.

4.1.1 N_2 Adsorption-Desorption Isotherms

The specific surface area was calculated by the Brunauer, Emmet, and Teller (BET) method, the micropore volume and pore diameter was acquired by Dubinin-Radushkevich (DR) method. The total pore volume estimated from the adsorption of nitrogen at the relative pressure of 0.99.

As shown in Figure 4.1, the nitrogen adsorption and desorption isotherms at low relative pressure of UiO-66, UiO-66-NH_2 25%, UiO-66-NH_2 50%, UiO-66-NH_2 75%, and UiO-66-NH_2 exhibit permanent microporous structure, which corresponds to the type I isotherm, confirming to the classification of the IUPAC classification (Donohue and Aranovich, 1998).

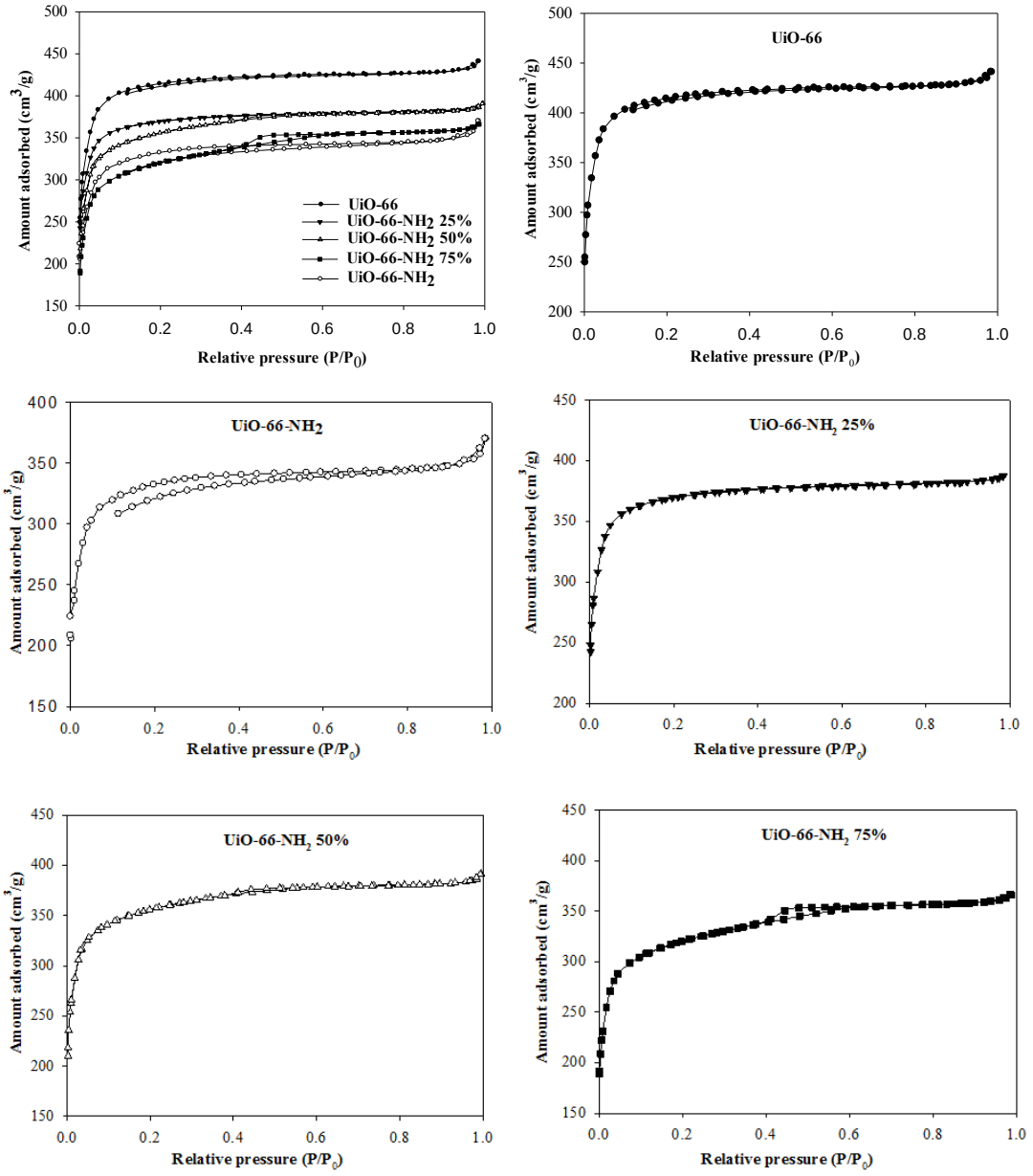

Figure 4.1 N_2 adsorption-desorption isotherms of Zr-based MOFs at -196 °C.

Both MIL-53(Al) and MIL-53(Al)-NH_2 exhibit nitrogen adsorption-desorption isotherms with micropores, mesopores, and hysteresis loops of type IV with increasing adsorption at high relative pressure (Meng and Park, 2012). This type of isotherm is obtained from the presence of mesoporous structure in the adsorbent. The hysteresis loop is related with the capillary condensation of the large pore attributing to the complete filling in the mesopores. At low relative pressure, the

isotherm is related to microporous materials, suggesting that mesostructured MOF materials are indeed micro crystalline MIL-53(Al). These results reveal that MIL-53(Al) and MIL-53(Al)-NH_2 form in the presence of the structure directing agent results in mesoporous materials, the walls of which are constructed from crystalline MIL-53(Al) and MIL-53(Al)-NH_2 (Dong *et al*., 2012).

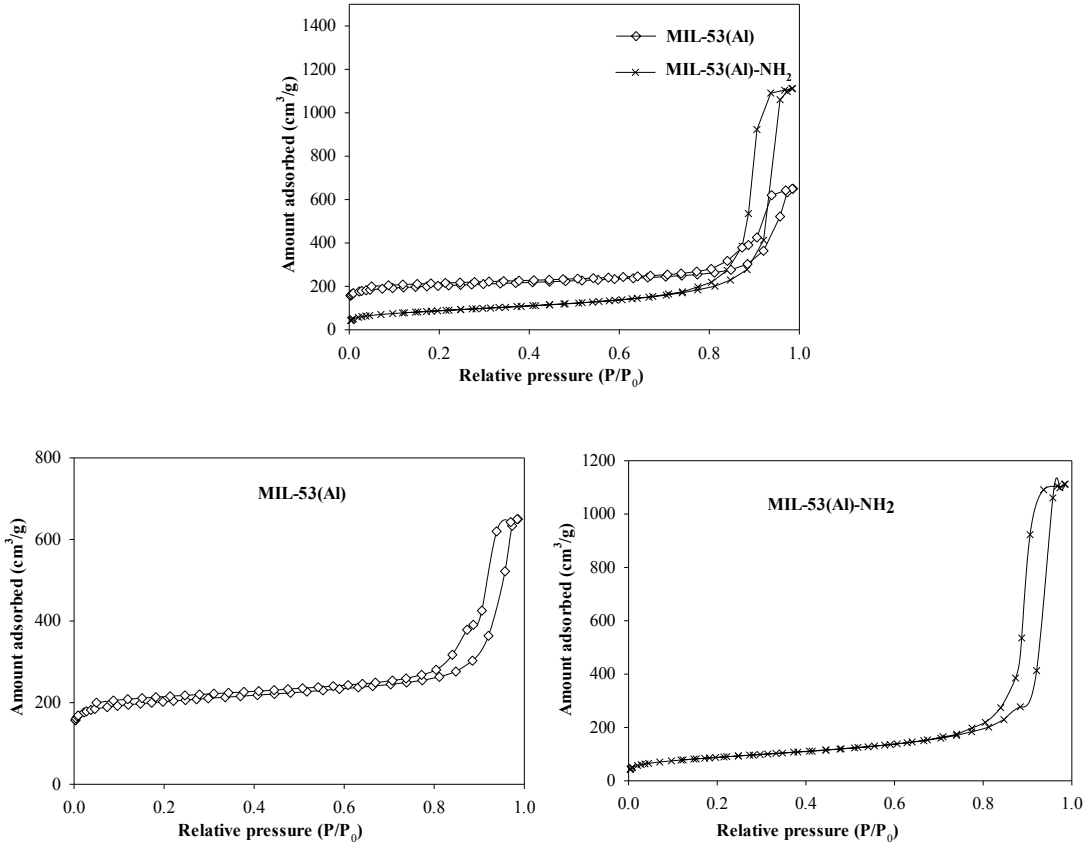

Figure 4.2 N_2 adsorption-desorption isotherms of Al-based MOFs at -196 °C.

The physical properties of samples are listed in Table 4.1. The BET surface area (S_{BET}), micropore volume (V_{micro}) calculated by Dubinin-Radushkevich (DR) method, total pore volume (V_{Total}), average pore diameter (D_{avg}), and the ratio of micropore volume to total pore volume were calculated and summarized. All adsorbents show that the higher surface area is consistent to the higher micropore volume. In contrast, the average pore diameter is narrower when increasing the surface area. UiO-66 has the highest surface area and micropore volume followed by

UiO-66-NH_2 25%, UiO-66-NH_2 50%, UiO-66-NH_2, UiO-66-NH_2 75%, MIL-53(Al), and MIL-53(Al)-NH_2. UiO-66 also has the smallest average pore diameter compared with the functionalized Zr-based MOFs. The surface area and micropore volume decrease with the increasing in the amino group. Besides, the addition of the amino group affects the average pore diameter. MIL-53(Al)-NH_2 has the lowest surface area and the largest average pore diameter beacause it has mesopore volume more than micropore volume. More specificly, 2-aminoterephtahlic acid linker (NH_2-BDC) has the larger structure than terephtahlic acid linker and segregates itself from the others because the linker can build hydrogen bonds with both NH_2-BDC itself and the solvent that leads to the decrease in the surface area and micropore volume (Rada *et al*., 2018).

Table 4.1 Physical properties of adsorbents

Adsorbent	S_{BET} (m^2/g)	V_{Total} (cm^3/g)	V_{Micro}, DR (cm^3/g)	D_{Avg} (nm)	V_{Micro}/V_{Total}
MIL-53 (Al)	722	1.01	0.30	6.77	0.30
MIL-53(Al)-NH_2	316	1.72	0.12	22.84	0.07
UiO-66	1,502	0.68	0.67	2.08	0.99
UiO-66-NH_2 25%	1,327	0.60	0.59	2.34	0.98
UiO-66-NH_2 50%	1,280	0.61	0.58	2.36	0.95
UiO-66-NH_2 75%	1,150	0.57	0.51	2.33	0.89
UiO-66-NH_2	1,204	0.57	0.52	2.42	0.91

As reported by Bagheri and Abedi (2011), adsorbed natural gas requires adsorbents with suitable characteristics. The high surface area, high micropore volume with no void or macropore volume, narrow average pore diameter are needed. The pore size should be greater than at least 0.78 nm (two times of methane molecules, methane kinetic diameter = 0.39 nm) (Mao and Sinnott, 2001). The appropriate pore size of adsorbent can support more attraction force of gas molecule and adsorbent, van der Waals forces, resulting in high methane storage

capacity. Thus, UiO-66, UiO-66-NH_2 25%, UiO-66-NH_2 50%, UiO-66-NH_2, UiO-66-NH_2 75%, MIL-53(Al), and MIL-53(Al)-NH_2 should have selective adsorption property owing to the high surface area and high micropore volume.

4.1.2 Fourier Transform Infrared Spectroscopy

As stated in Hao *et al*. (2013), the adsorbents with a higher hydrophobic property have higher methane adsorption capacity. Generally, the surface area of adsorbents contains hydrophobic and hydrophilic sites but the adsorption potential of methane prefers hydrophobic sites owing to the non-polar nature of methane. However, carbon dioxide molecule, a polar adsorbate, is the competition adsorbate in this experiment. The high hydrophilic sites on the adsorbent surface tend to increase the carbon dioxide adsorption capacity. All adsorbents have been checked by a FTIR spectrometer for intensity of functional group, which affects the methane and carbon dioxide adsorption. Figure 4.3 shows the Fourier transform infrared spectroscopy spectra of UiO-66 and functionalized UiO-66 with loading amino group (-NH_2) at different ratios. For UiO-66, the weak peak at 1,656 cm^{-1} is attributed to the symmetric stretching vibrations of C=O in carboxyl functional group (-COO^-) or carboxylic acid present in terephthalic acid (H_2-BDC). The characteristic bands represented the asymmetric stretching of O-C-O in H_2-BDC organic ligand is seen at 1,582 cm^{-1}. The small peak at 1,500 cm^{-1} also represents in a C=C of benzene ring, while the more intense peak at 1,386 cm^{-1} is linked to the asymmetric stretching of O-C-O in the carboxylate group of the H_2-BDC ligand. The peaks at 748 and 665 cm^{-1} are assigned to O-H and C-H vibration in the H_2-BDC ligand. For functionalization of UiO-66 with -NH_2 group, the benzene ring substituted with primary amine is observed via two peaks at 3,299 and 3,464 cm^{-1}, relating to the symmetric and asymmetric stretching of N-H bonding, respectively (Cao *et al*., 2015). Moreover, the two peaks are obviously detected in higher loading of -NH_2 to UiO-66 as UiO-66-NH_2 75% and UiO-66-NH_2. However, the amine peaks are faded when the loading of -NH_2 decreases.

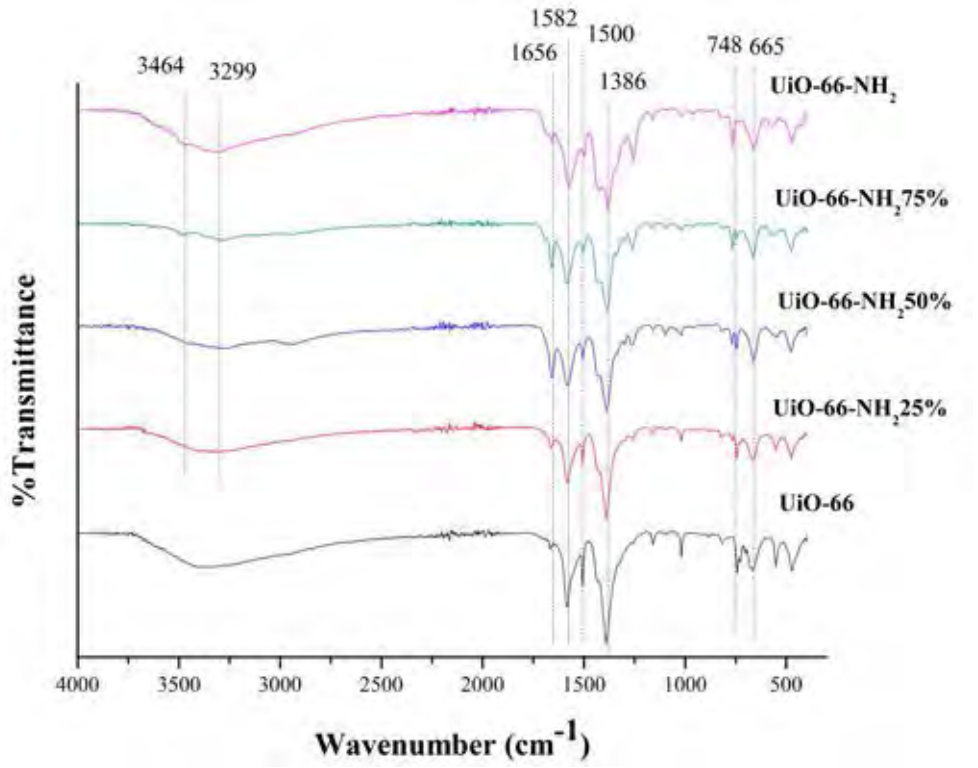

Figure 4.3 Fourier transform infrared spectroscopy of UiO-66, UiO-66-NH_2 25%, UiO-66-NH_2 50%, UiO-66-NH_2 75%, and UiO-66-NH_2.

MIL-53(Al) and MIL-53(Al)-NH_2 are metal organic framework using aluminum nitrate as the aluminium source connected with 1,4-benzenedicarboxylic acid (H_2-BDC) or as the organic ligand. The characteristics of MIL-53(Al) and MIL-53(Al)-NH_2 are shown in Figure 4.4. The IR spectra of both Al-based MOFs are in agreement with the vibration bands characteristic at 1,535 cm^{-1} and 1,461 cm^{-1}, which could be attributed to C-O asymmetric stretching confirming the presence of dicarboxylate group. The band at 1,461 cm^{-1} also confirms symmetric carboxylate O-C-O stretching vibrations of benzene ring, which is consistent with the presence of C-O incorporated bridging hydroxyl ions that link to aluminum into infinite chain (Dong *et al*., 2011). The peak at 1,500 cm^{-1} also shows in C=C of benzene ring. In addition, the spectra evidence increasing intensities of bands at 3,600 and 3,400 cm^{-1}, characteristic of the stretching mode of N-H bond (Martinez *et al*., 2017). The low intensity of the primary amino band may be attributed to the

strong interconecting between amino group on the coordinated linker and bridging hydroxyl group on the metal center (Rada *et al*., 2015). The characteristic spectra of MIL-53(Al) are similar to the characteristic spectra of UiO-66 spectrum due to the same organic ligand (Yan *et al*., 2015).

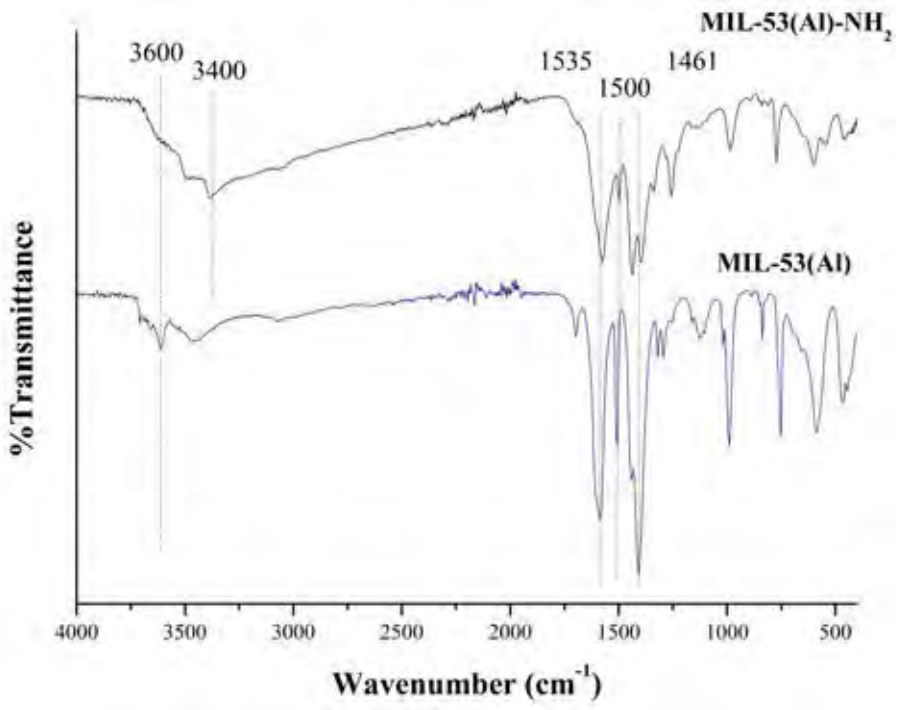

Figure 4.4 Fourier transform infrared spectroscopy of MIL-53(Al) and MIL-53(Al)-NH_2.

4.1.3 Scanning Electron Microqscopy

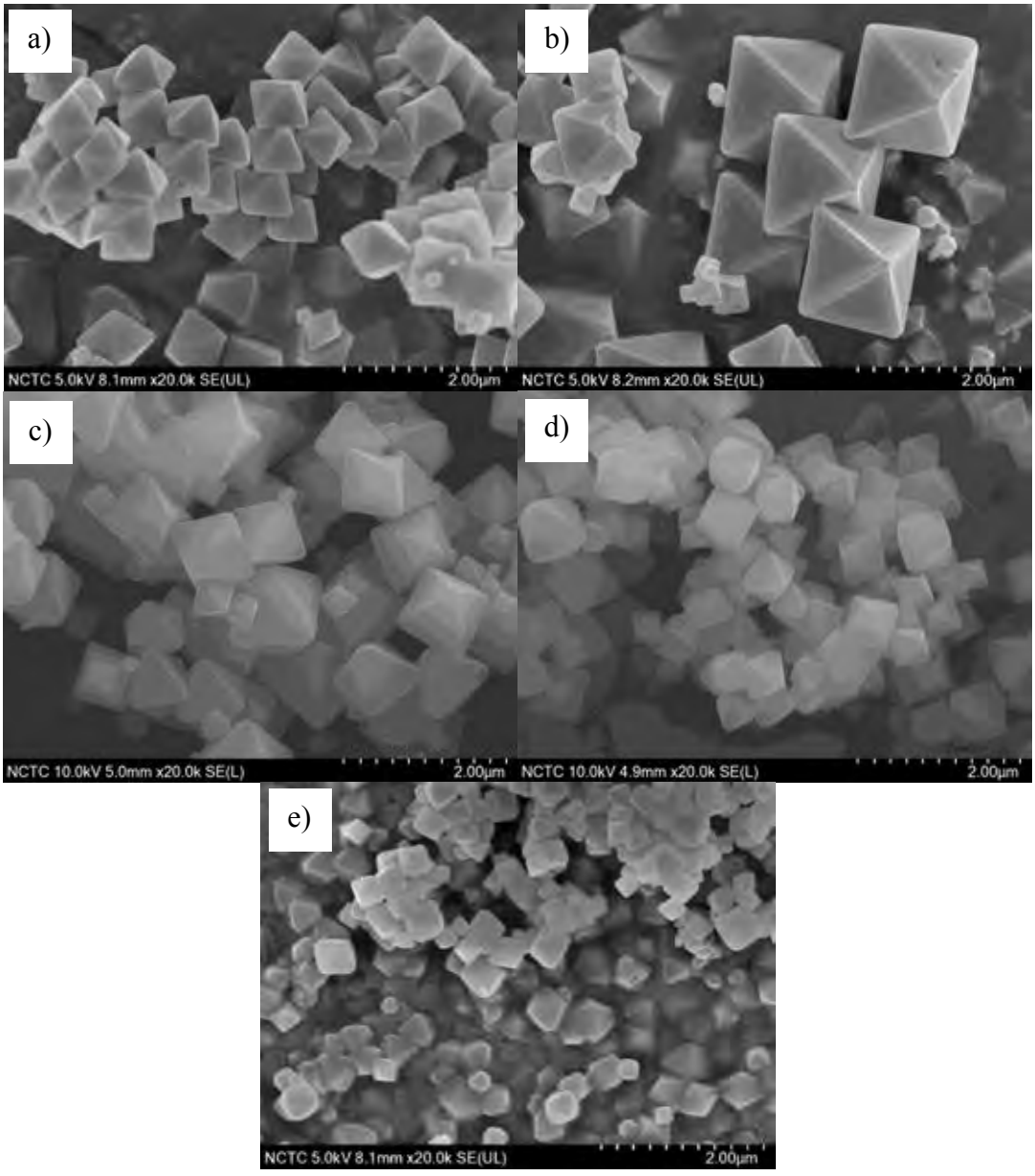

Figure 4.5 Scanning electron micrographs of (a) UiO-66, (b) UiO-66-NH_2 25%, (c) UiO-66-NH_2 50%, (d) UiO-66-NH_2 75%, and (e) UiO-66-NH_2.

Figure 4.5 shows SEM micrographs of UiO-66, UiO-66-NH_2 25%, UiO-66-NH_2 50%, UiO-66-NH_2 75%, and UiO-66-NH_2. All samples present similar crystalline structure as asymmetrical crystal with triangular base pyramid shape at different sizes (Abid *et al*., 2013). UiO-66-NH_2 has smaller crystal size and aggregated crystal than the other MOFs. The morphology of MIL-53(Al) and MIL-53(Al)-NH_2 are rod-like structure, as shown in Figure 4.6. This figure corresponds to the report by Chen *et al*. (2018).

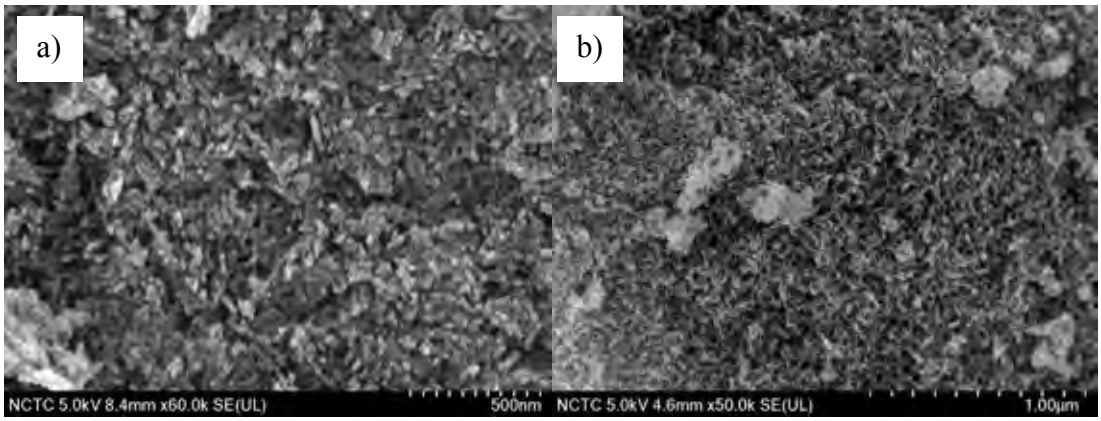

Figure 4.6 Scanning electron micrographs of (a) MIL-53(Al) and (b) MIL-53(Al)-NH_2.

4.1.4 X-ray Diffraction Analysis

The structural stability cystallinity and the successful synthesis procedure of UiO-66 and functionalized UiO-66 are confirmed by comparing XRD patterns illustrated in Figure 4.7 with characteristic peaks of UiO-66 at $2\theta = 7.35^{o}$, 8.49^{o}. XRD patterns of UiO-66 and functionalized UiO-66 with -NH_2 at different ratios cleary show that the crystalline structures match the pattern as reported in previous study (Luu *et al.,* 2015). As a result, all functionalized UiO-66 samples are almost identical to that of UiO-66, indicating that functionalization of UiO-66 with -NH_2 group are also well-developed.

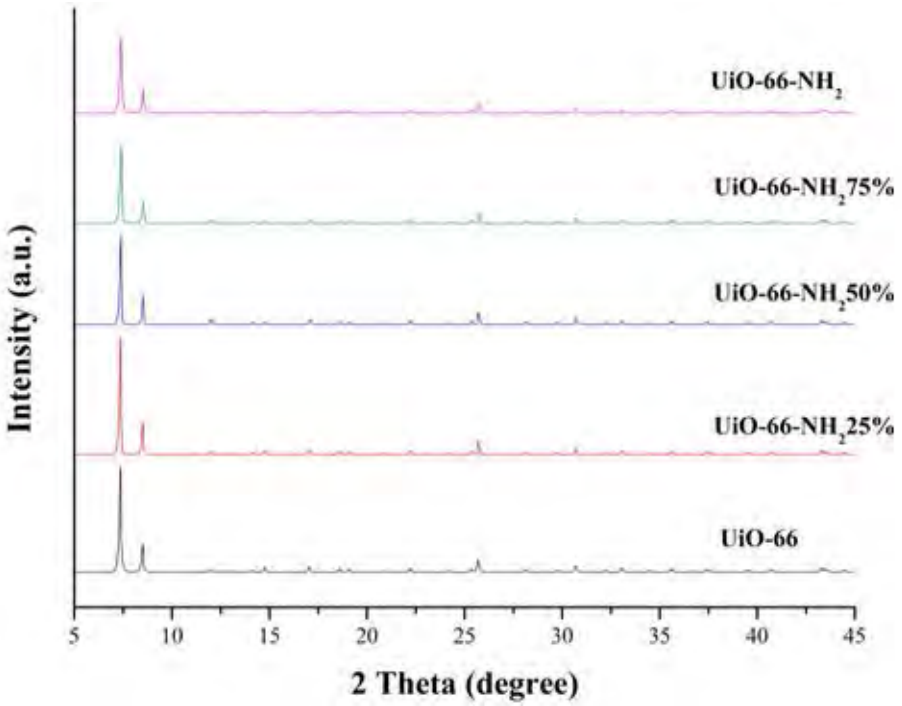

Figure 4.7 X-ray diffraction (XRD) patterns of UiO-66, UiO-66-NH_2 25%, UiO-66-NH_2 50%, UiO-66-NH_2 75%, and UiO-66-NH_2.

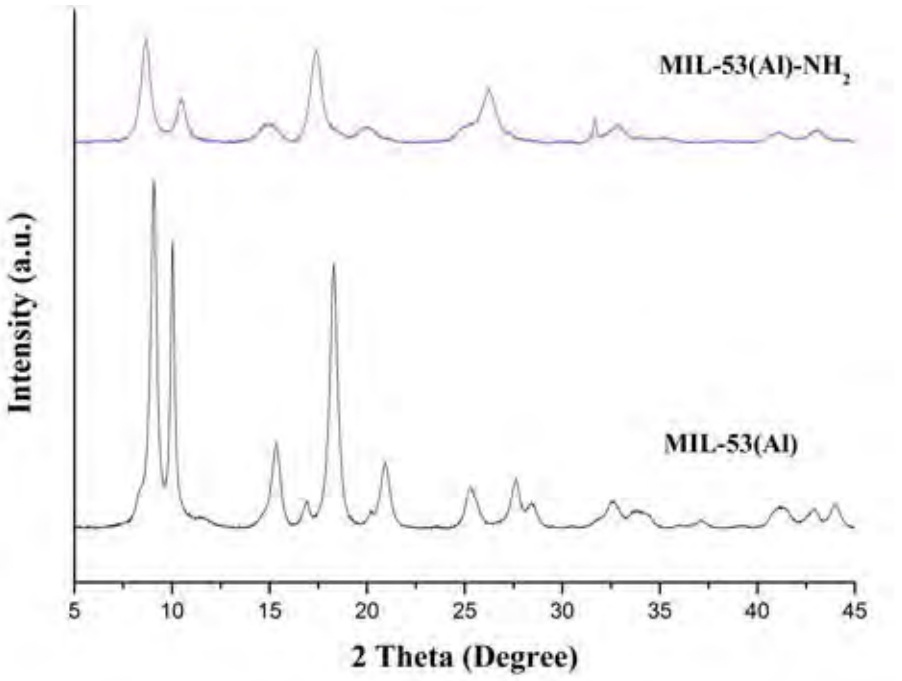

Figure 4.8 X-ray diffraction (XRD) patterns of MIL-53(Al) and MIL-53(Al)-NH_2.

XRD patterns in Figure 4.8 are clearly identified as the microstructured MOFs constructed from MIL-53(Al) crystals. Diffraction peaks of MIL-53(Al)-NH_2 are rather broader than those of MIL-53(Al), because the MIL-53(Al) crystals, while build up the microstructured walls, are small crystals with crystal sizes on the nanoscale. Small changes in the diffraction patterns among the samples are attributed to variations in the guest molecules remaining inside the pores. The presence of NH_2 has only minor influence on the structure of MIL-53(Al), and both Al-based MOFs show very similar powder diffraction 2θ = 9.0, 10.5, 15.3, and 18.2 (Kim *et al.,* 2012).

4.2 Equilibrium Adsorption of Methane

Methane adsorption isotherms (at 33 °C within a pressure range of 0-100 psia) on UiO-66, UiO-66-NH_2 25%, UiO-66-NH_2 50%, UiO-66-NH_2 75%, UiO-66-NH_2, MIL-53(Al), and MIL-53(Al)-NH_2 are presented in Figures 4.9 and 4.10. Each experiment was repeated at least five times to ensure its reproducibility.

Comparison among the Zr-based MOFs, UiO-66-NH_2 shows the highest methane adsorption followed by UiO-66-NH_2 25%, UiO-66-NH_2 75%, UiO-66-NH_2 50%, and UiO-66. The results present that the increase in the pressure increases the methane adsorption. As reported by Bagheri and Abedi (2011), the higher pressure induces more van der Waals attraction forces between the surface of adsorbent and the methane molecule. It clearly indicates that the addition of amino group results in higher methane adsorption than UiO-66, although the surface area and micropore volume of amino-functionalization on the Zr-based samples are lower than UiO-66. It can be deduced that the presence of -NH_2 increases affinity toward methane, which may play more important role on the adsorption of methane than specific area and pore volume (Luu *et al*., 2015). Even though UiO-66, UiO-66-NH_2 25%, UiO-66-NH_2 50%, UiO-66-NH_2 75%, and UiO-66-NH_2 have approximately similar surface area, micropore volume, the average pore diameter, and the ratio of micropore volume to total pore volume, UiO-66-NH_2 25% adsorbs methane as well as UiO-66-NH_2 does. This may be described by their surface amino functional group contribution on the methane uptake. However, in the case of UiO-66-NH_2 50%,

UiO-66-NH_2 75%, and UiO-66-NH_2, which have similar nitrogen weight in the structure from amino group, the effects of surface area on methane adsorption are more prominent than the effect of amino group.

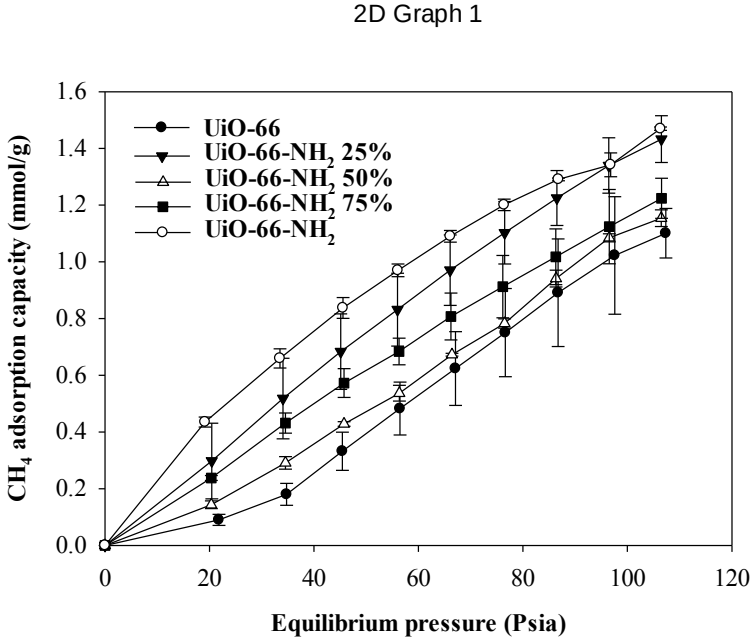

Figure 4.9 Methane adsorption on UiO-66, UiO-66-NH_2 25%, UiO-66-NH_2 50%, UiO-66-NH_2 75%, and UiO-66-NH_2 at 33 ^oC.

In case of different metal clusters, MIL-53(Al) has higher methane adsorption than UiO-66 even through MIL-53(Al) has lower surface area than UiO-66. This can be explained by breathing of frameworks as reported by Boutin *et al*. (2010). MIL-53(Al) is a flexible MOF, and its structure can contract and stretch by the change in the temperature and pressure. In this experimental condition, MIL-53(Al) has large pore structure with diamond shape, as shown in Figure 4.11. Comparing the diamond shape of MIL-53(Al) and the face center unit (fcu) of UiO-66, MIL-53(Al) framework is easier to expand than the stable rigid framework of UiO-66. As the result, more gas molecules can fill in MIL-53(Al). Moreover, MIL-53(Al) adsorbs methane approximately equal to UiO-66-NH_2 even though both adsorbents have significantly different surface area, micropore volume, tota pore volume, average pore diameter, and micropore volume to total pore volume ratios, as shown in Table 4.1. This can be described by their different open metal sites but

similar structure, as shown in Figure 4.11. The open metal sites may induce a different interaction toward methane and methane adsorption. Since Al atom in MIL-53(Al) is larger interaction than Zr atom in UiO-66-NH_2, MIL-53(Al) shows a bit higher methane adsorption than UiO-66-NH_2, even though MIL-53(Al) has much lower surface area than UiO-66-NH_2. Furthermore, UiO-66 has higher methane adsorption than MIL-53(Al)-NH_2 because its surface area is five times higher than UiO-66. UiO-66 also has higher micropore volume to total pore volume ratios (0.99) than MIL-53(Al)-NH_2 (0.30), which means UiO-66 has high micropore volume in the structure. In other words, UiO-66 has relatively low mesopore volume. The result is in agreement with the report by Bagheri and Abedi (2011), who reported that methane is more favourable to fill in micropores than in macropores and mesopores. For further clarification, Mosher *et al*. (2013) described that the opposing wall, where the distance between pores is close enough, will have the high force field and contributes to the higher adsorption. The mesopore volume of MIL-53(Al)-NH_2 leads to large pore size diameter of MIL-53(Al)-NH_2. The result shows that not only the surface area, micropore volume, and functionalized MOFs affect the methane adsorption but also the ratio of micropore volume to total pore volume

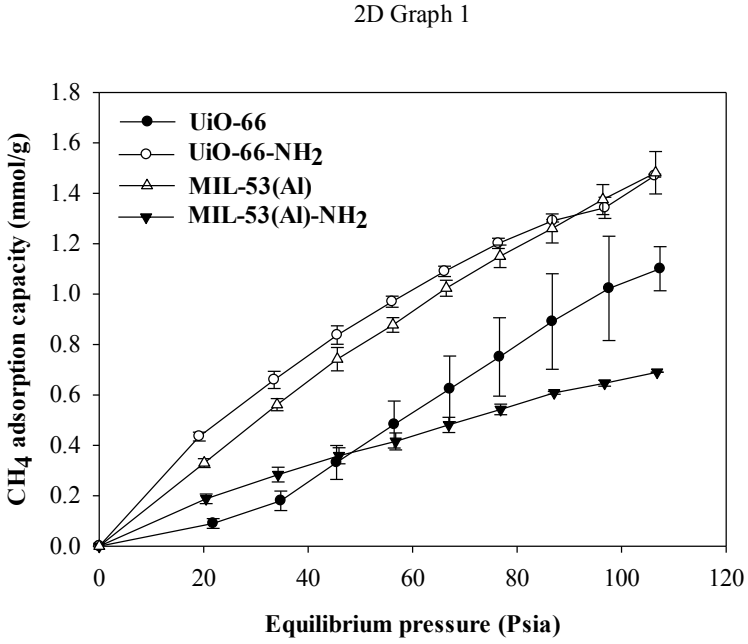

Figure 4.10 Methane adsorption on UiO-66, UiO-66-NH_2, MIL-53(Al), and MIL-53(Al)-NH_2 at 33 ^oC.

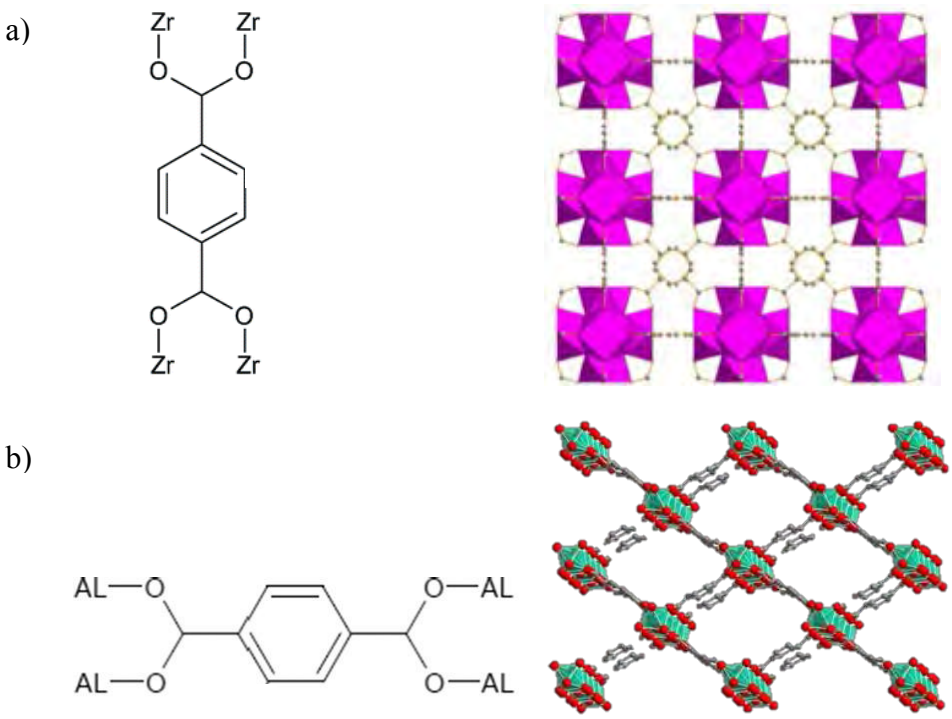

Figure 4.11 Structure of (a) UiO-66 and (b) MIL-53(Al) (Boutin *et al*., 2010).

The Langmuir, Fruendlich, and Sips isotherm models were fitted to the experimental data. The results are in Figures 4.12 to 4.18. The isotherms from the models along with theory from measured methane adsorption on UiO-66, UiO-66-NH_2 25%, UiO-66-NH_2 50%, UiO-66-NH_2 75%, UiO-66-NH_2, MIL-53(Al), and MIL-53(Al)-NH_2 are compared in the figures. Although the three models can correlate the data satisfactorily, the Sips model provides the best fit for UiO-66, which can be confirmed by the value of regression (R^2) with three adjustable parameters. The Sips model is suitable for predicting adsorption on heterogeneous surfaces, thereby avoiding the limitation of increased adsorbate concentration normally associated with the Freundlich model (Ayawei *et al*., 2017). At low adsorbate concentration, this model reduces to the Freundlich model, but at high concentration of adsorbate, it predicts the Langmuir model (monolayer adsorption). The parameters of the Sips isotherm model are concentration dependent, isotherm exponent, and isotherm constants. The Langmuir adsorption isotherm describes the homogeneous surface, assuming that there is no lateral interaction between adjacent adsorbed molecules when the single molecule occupies the single surface site.

Freundlich isotherm only approximately explains the behaviour of adsorption on
2D Graph 1
heterogeneou · the
prediction of o fit
the adsorptio d.

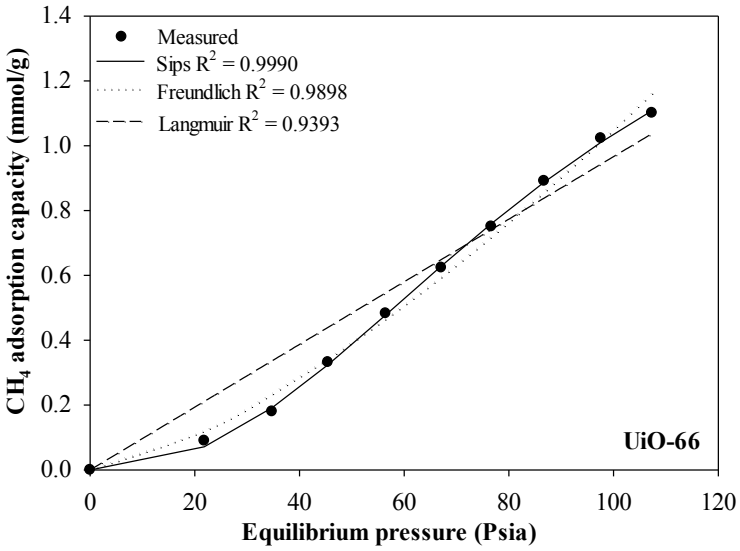

Figure 4.12 Equilibrium isotherm modelling for methane adsorption on UiO-66 at 33 ºC.

Pressure vs Measured
Pressure vs Sips
2D Graph 3

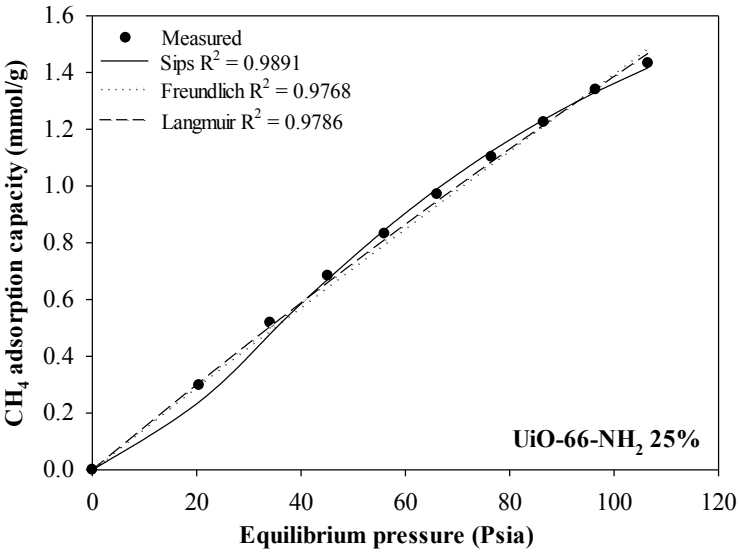

Figure 4.13 Equilibrium isotherm modelling for methane adsorption on UiO-66-NH_2 25% at 33 ºC.

Pressure vs real
Pressure vs fit
Pressure vs F
Pressure vs L

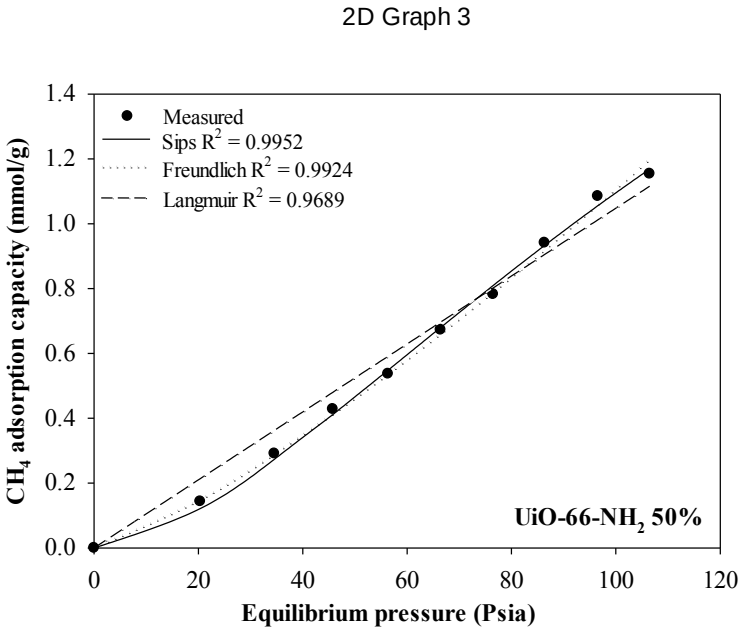

Figure 4.14 Equilibrium isotherm modelling for methane adsorption on UiO-66-NH_2 50% at 33 °C.

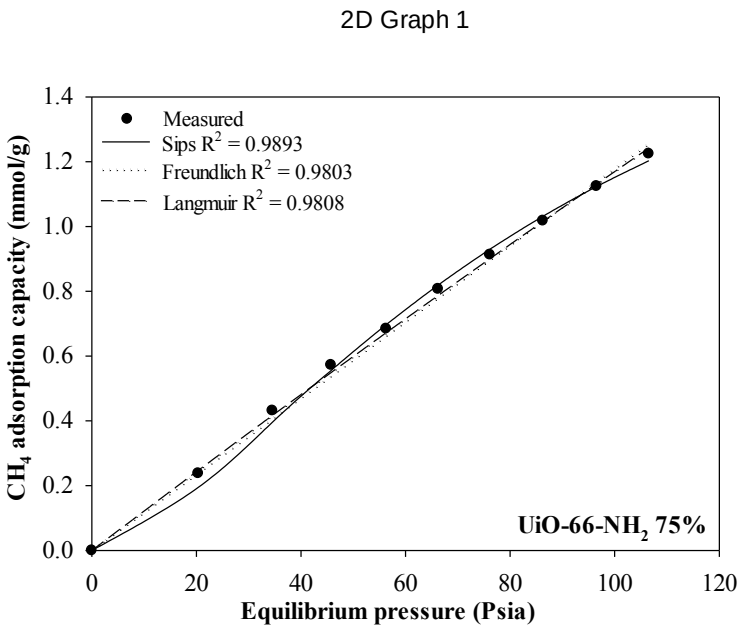

Figure 4.15 Equilibrium isotherm modelling for methane adsorption UiO-66-NH_2 75% at 33 °C.

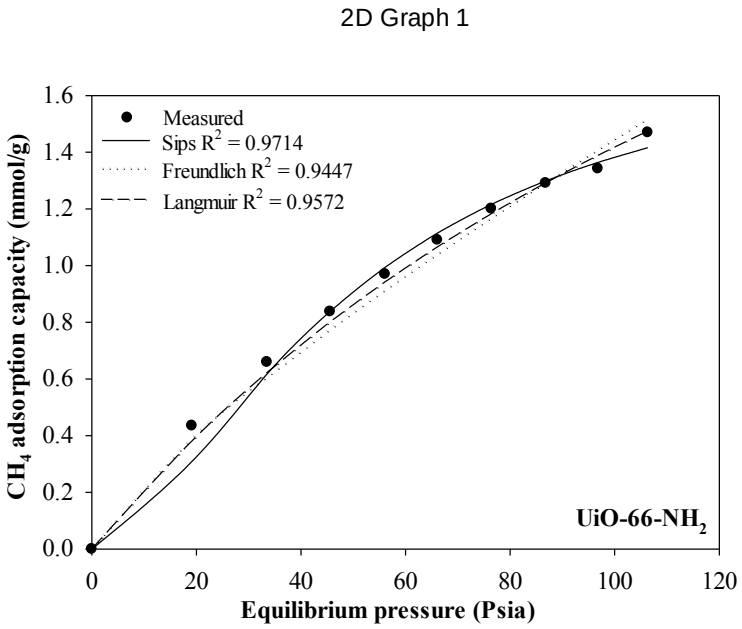

Figure 4.16 Equilibrium isotherm modelling for methane adsorption on UiO-66-NH_2 at 33 ºC.

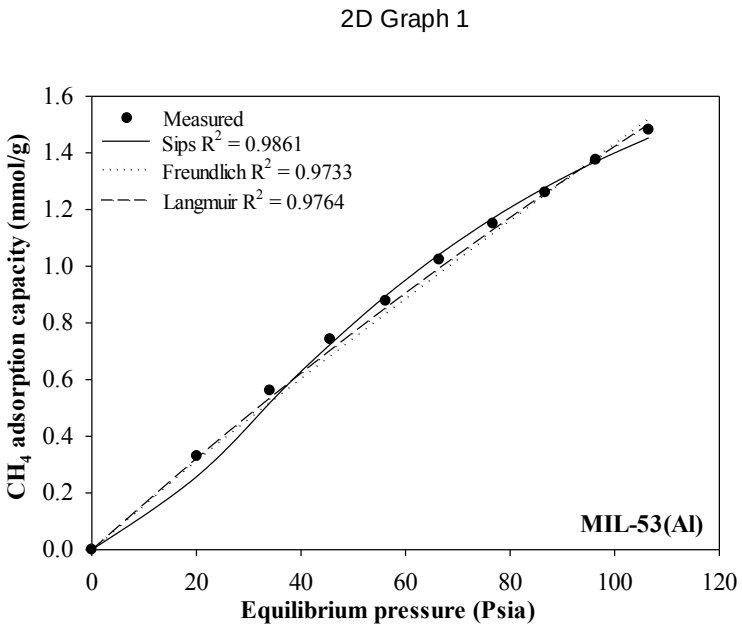

Figure 4.17 Equilibrium isotherm modelling for methane adsorption on MIL-53(Al) at 33 ºC.

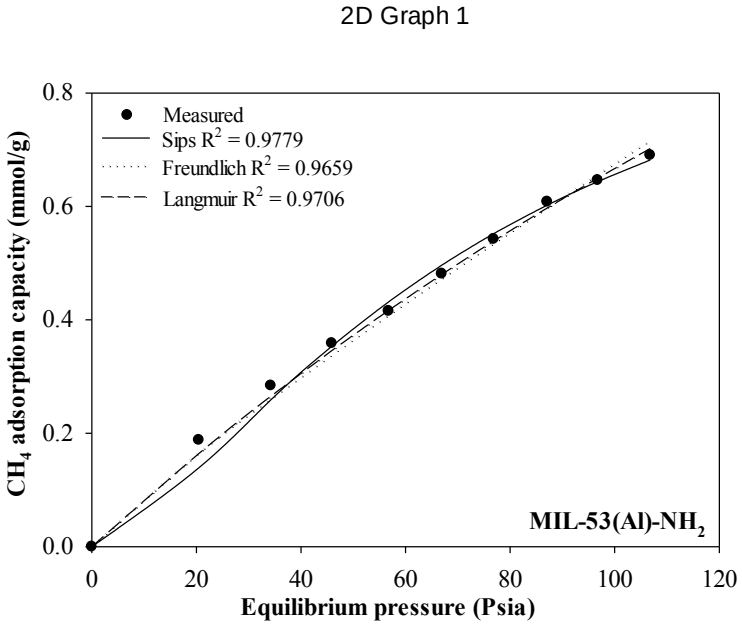

Figure 4.18 Equilibrium isotherm modelling for methane adsorption on MIL-53(Al)-NH_2 at 33 ºC.

4.3 Equilibrium Adsorption of Carbon Dioxide

Carbon dioxide adsorption on adsorbents can be enhanced with many methods. Three strategies have been proposed to enhance the carbon dioxide binding energy on MOFs, including the developments of MOFs with open metal sites, ultra mircoporous MOFs with high surface area, and amine-functionalized MOFs (Liu *et al*., 2019). This work studied on open metal site (Al atom and Zr atom) and amino-functionalized on Al-based and Zr-based MOFs.

The carbon dioxide adsorption capacity on UiO-66, UiO-66-NH_2 25%, UiO-66-NH_2 50%, UiO-66-NH_2 75%, and UiO-66-NH_2 are in Figure 4.19. Generally, the carbon dioxide uptake increases with the increasing pressure along the experimental comdition. It can be observed that the carbon dioxide adsorption on UiO-66-NH_2 is the highest followed by UiO-66-NH_2 25%, UiO-66-NH_2 75%, UiO-66-NH_2 50%, and UiO-66. Although UiO-66-NH_2 25%, UiO-66-NH_2 50%, UiO-66-NH_2 75%, and UiO-66-NH_2 have lower the surface area micropore volume than UiO-66, the amino funtionalization on Zr-based always show higher carbon dioxide capacity than that UiO-66. This could be attributed to the presence of -NH_2 in the porous structure. The

explanation of this result is the effect of Lewis base center of NH_2 group in the framework that may lead to the increase in the interaction with carbon dioxide molecule. Consequently, adding the amino group to UiO-66 increases the gas uptake.

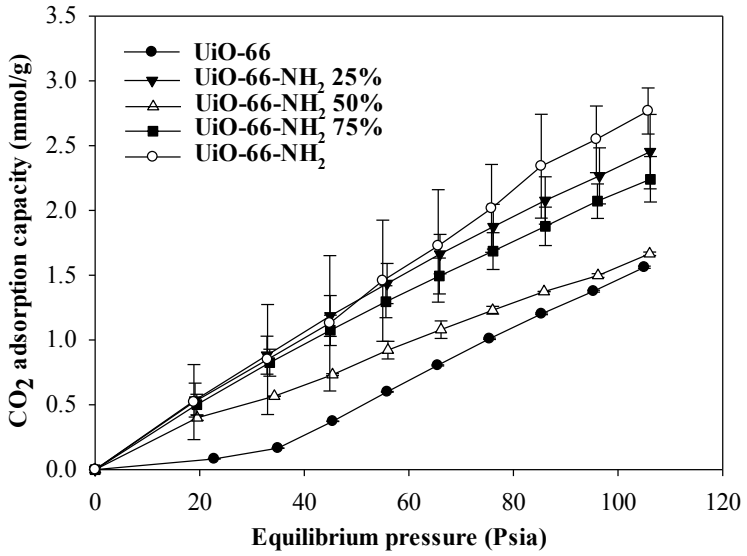

Figure 4.19 Carbon dioxide adsorption on UiO-66, UiO-66-NH_2 25%, UiO-66-NH_2 50%, UiO-66-NH_2 75%, and UiO-66-NH_2 at 33 ºC.

The effects of the surface area, micropore volume, and the open metal sites on the carbon dioxide adsorption are shown in Figures 4.20. The higher the surface area and micropore volume, the higher the carbon dioxide adsorption. Apart from the surface area and micropore volume, the open metal sites and organic ligands can facilitate interaction with polarizable carbon dioxide molecules and enhance carbon dioxide adsorption since they allow close approach of carbon dioxide to the pore surface as described by Sumida *et al*. (2012). It can be seen that UiO-66, UiO-66-NH_2, MIL-53(Al), and MIL-53(Al)-NH_2 have different bridging ligands and open metal sites. Canepa *et al*. (2013) stated that different metal atoms showed different carbon dioxide interaction to MOFs and also depended on the amount of open metal sites. It can be observed that Al atom has much larger interaction to oxygen atom from carbon dioxide molecules than Zr atom even MIL-53(Al) has lower surface

area than UiO-66-NH_2. Correspondingly, MIL-53(Al) consisting of Al atoms has approximately the same carbon dioxide adsorption as UiO-66-NH_2.

In addition, Liu *et al*. (2012) explained that the oxygen atom in carbon dioxide molecule mainly interacts to delocalized aromatic π system of UiO-66. The different interactions determine the magnitude of force inducing the carbon dioxide adsorption. The lowest carbon dioxide adsorption of MIL-53(Al)-NH_2 is consistent with its low surface area and micropore volume. MIL-53(Al)-NH_2 highly composes of mesopores more than micropores. In spite of Al atom with amino functionalization effect in MIL-53(Al)-NH_2, the surface area and micropore volume has more effect on the carbon di

2D Graph 2

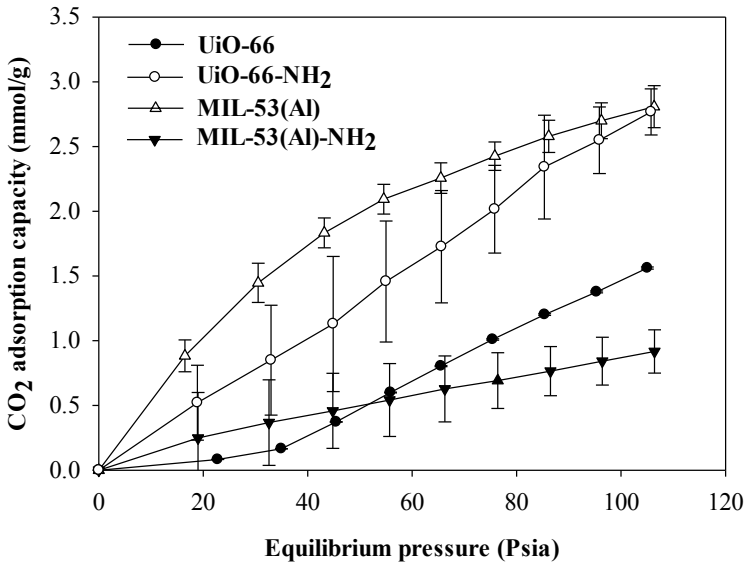

Figure 4.20 Carbon dioxide adsorption on UiO-66, UiO-66-NH_2, MIL-53(Al), and MIL-53(Al)-NH_2 at 33 ^oC.

Pressure vs capacity- Mil-53
Pressure vs capacity- Mil-53: 43.17
Col 4 vs capacity-MIL-53-NH2
Col 4 vs capacity-MIL-53-NH2: 76.39
Col 7 vs capacity UiO-66
Col 10 vs capacity UiO-66-NH2

However, the difference structure of adsorbents plays a more important role on the carbon dioxide adsorption than the micropore volume to total pore volume ratio as in the case of UiO-66 and MIL-53(Al). The breathing structural effect of MIL-53(Al) can result in large pore structure and enhance more carbon dioxide molecules than the rigid structure of UiO-66. Thus, the appropriate metal site and organic ligand should result in higher carbon dioxide adsorption.

Figures 4.21 to 4.27 present the conparison amoung the Langmuir, Fruendlich and Sips isotherm models with the experimental data. The results illustrate that Langmuir, Fruendlich and Sips model appropriate to fit all the measured data on all adsorbents. But, the Sips model the shows the best fit carbon dioxide adsorption for UiO-66. Moreover, the Sips model has three adjustable parameters and the highest value of regression (R^2) which confirms to correlate the data more satisfactory than the other models. Due to the limitation of the two adjustable parameter and empirical equation on Langmuir and Freundlich isotherms models, theses reasons lead to the models suitable for nonideal adsorption on homogenouse and heterogeneous surface as well as monolayer adsorption. However, Langmuir and Fruendlich models are also enough to fit the equilibrium data within the temperature and pressure ranges studied for UiO-66-NH_2 25%, UiO-66-NH_2 50%, UiO-66-NH_2 75%, UiO-66-NH_2 and MIL-53(Al), and MIL-53(Al)-NH_2. Because the via chemisorptio

2D Graph 1

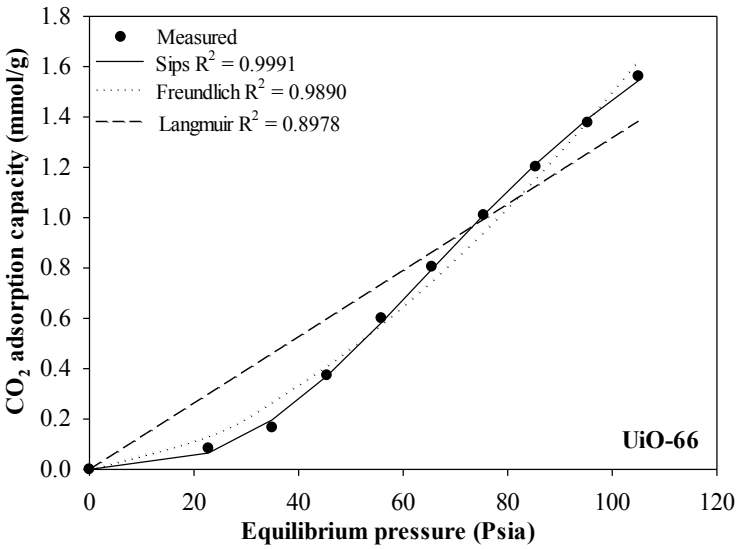

Figure 4.21 Equilibrium isotherm modelling for carbon dioxide adsorption on UiO-66 at 33 ºC.

pressure vs real
pressure vs fit
pressure vs F
pressure vs L

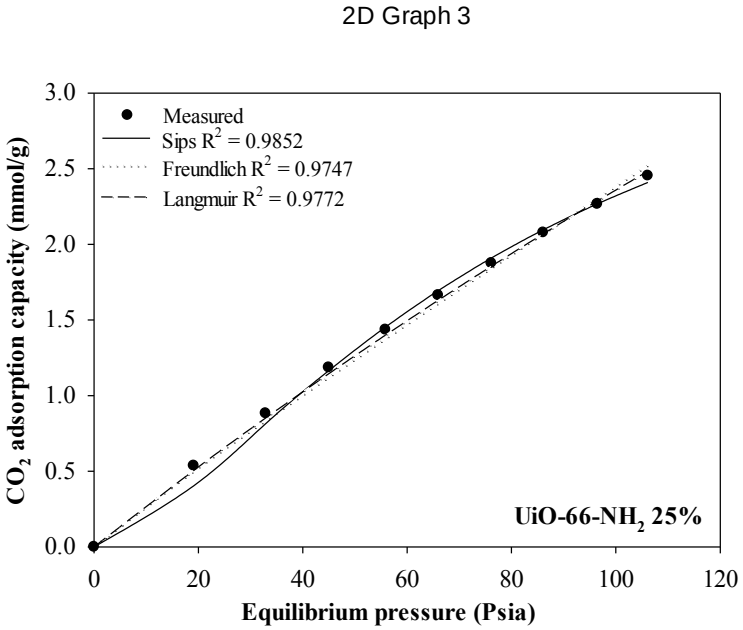

Figure 4.22 Equilibrium isotherm modelling for carbon dioxide adsorption on UiO-66-NH_2 25% at 33 °C

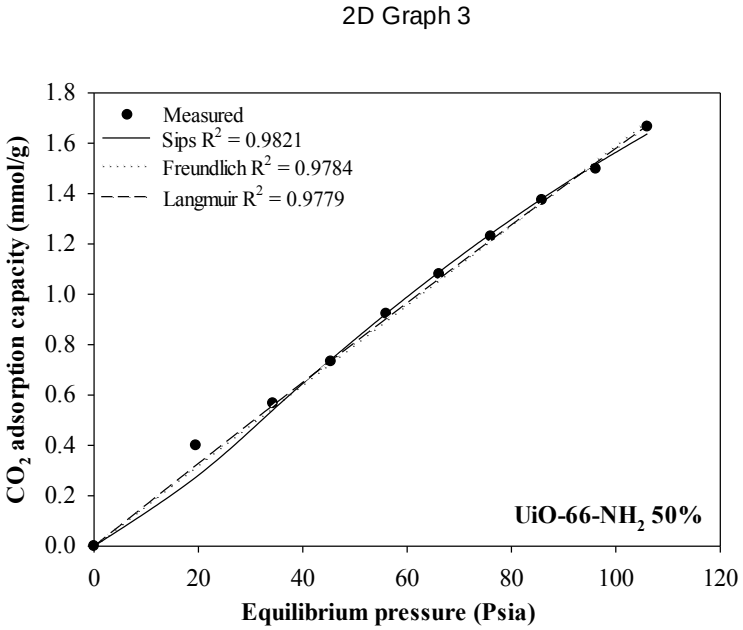

Figure 4.23 Equilibrium isotherm modelling for carbon dioxide adsorption on UiO-66-NH_2 50% at 33 °C

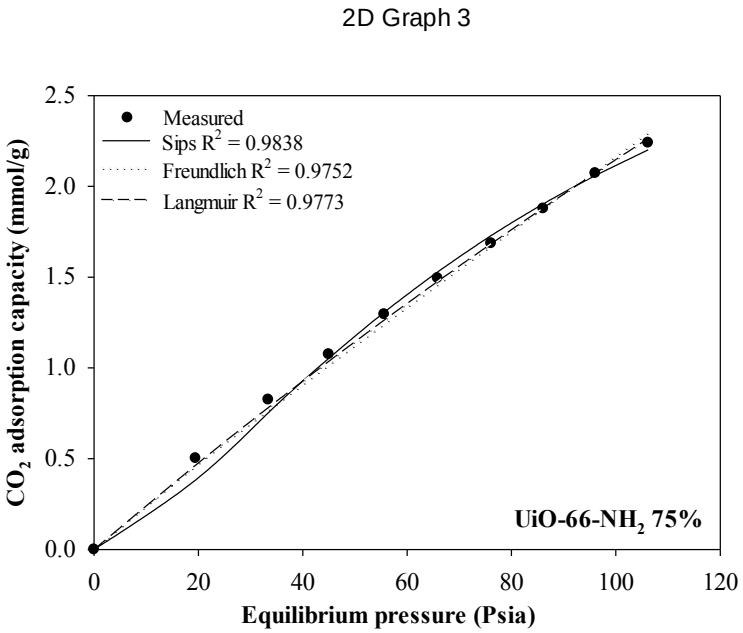

Figure 4.24 Equilibrium isotherm modelling for carbon dioxide adsorption on UiO-66-NH_2 75% at 33 ^oC.

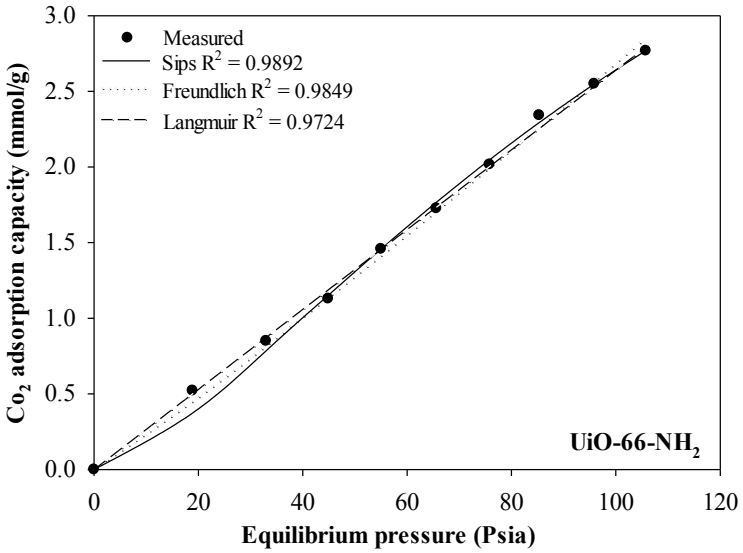

Figure 4.25 Equilibrium isotherm modelling for carbon dioxide adsorption on UiO-66-NH_2 at 33 ^oC.

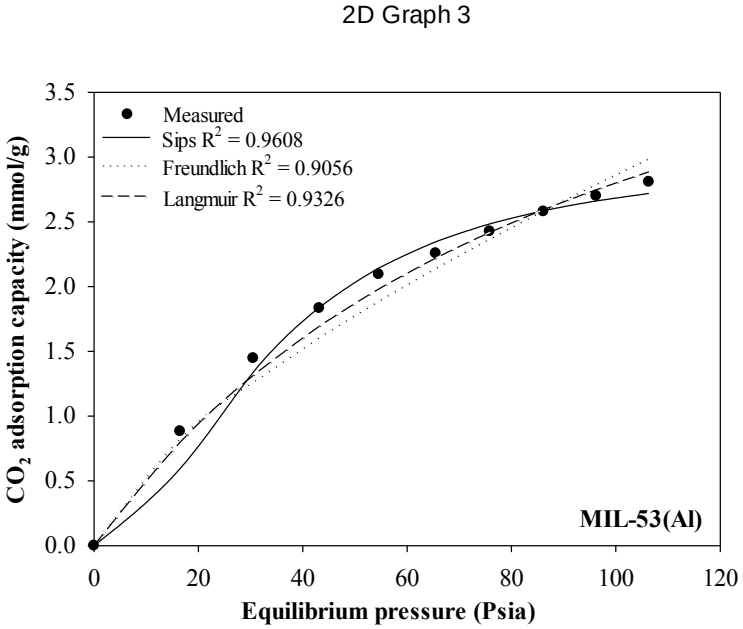

Figure 4.26 Equilibrium isotherm modelling for carbon dioxide adsorption on MIL-53(Al) at 33 ºC.

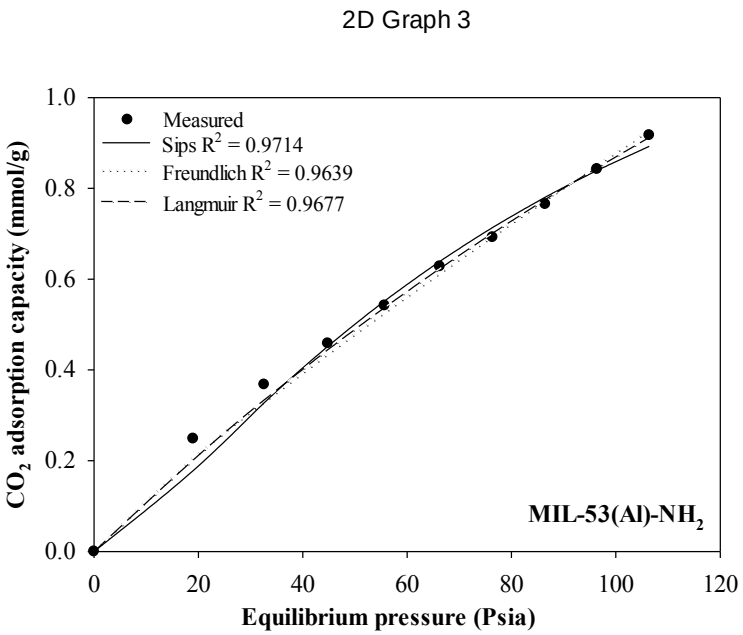

Figure 4.27 Equilibrium isotherm modelling for carbon dioxide adsorption on MIL-53(Al)-NH_2 at 33 ºC.

4.4 Comparative Adsorption of Methane and Carbon Dioxide

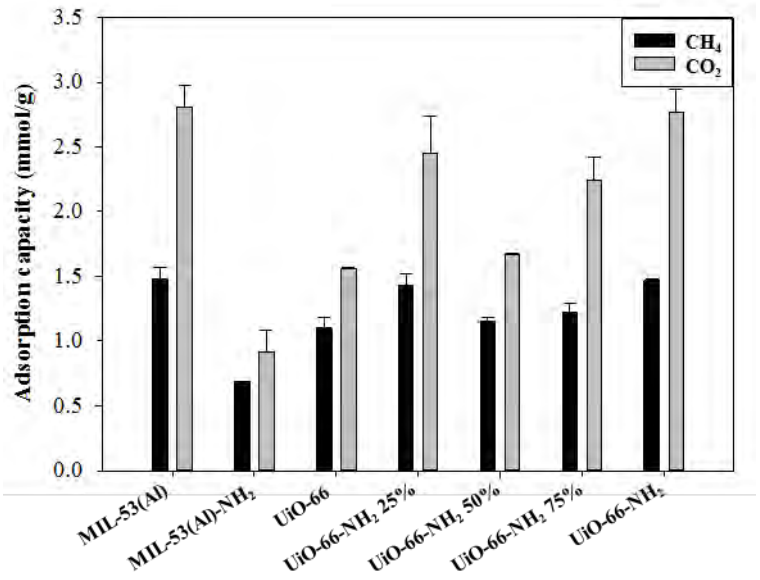

Figure 4.28 Adsorption of methane and carbon dioxide on UiO-66, UiO-66-NH_2 25%, UiO-66-NH_2 50%, UiO-66-NH_2 75%, UiO-66-NH_2, MIL-53(Al), and MIL-53(Al)-NH_2 at 100 psi and 33 °C.

Accordingly, the comparison between methane and carbon dioxide adsorption is illustrated in Figure 4.28. In general, it can be seen that the carbon dioxide adsorption on all adsorbents is higher than the methane adsorption. The carbon dioxide molecule is selectively adsorbed on the adsorbents owing to its properties. Carbon dioxide is a nonpolar linear molecule, in which the carbon atom adopts sp hybridization combined with oxygen atoms. Electrons from C and O atoms form strong π dislocated bonds. The remaining electrons from O atoms contribute to the antibond orbital of the carbon dioxide molecule. Here, O atoms present electronegativity, and C atoms show electropositivity (Liu *et al*., 2019). Therefore, functional groups with special adsorptive sites that can accept electrons or donate electrons would have strong affinity to carbon dioxide. Al-based and Zr-based MOFs constructed by organic ligands and metal ions through coordinative bonds could exhibit large surface area and high porosity. Moreover, carbon dioxide has higher critical temperature (T_c) than methane (T_c, CO_2 = 31.21 °C, T_c, CH_4 = -82 °C). Then,

carbon dioxide behaves like a condensate stream or less volatile resulting in more opportunity to be adsorbed on the adsorbents. Meanwhile, the weaker octopole of methane is expected to play a far less important part in relation to dispersion forces reported by Nicholson and Gubbins (1996). UiO-66, UiO-66-NH_2 25%, UiO-66-NH_2 50%, UiO-66-NH_2 75%, UiO-66-NH_2, MIL-53(Al), and MIL-53(Al)-NH_2 compose of benzene rings which interact with quadrupole of carbon dioxide are dominated by the π–π interactions (Chen *et al*., 2013). Thus, the adsorbents can interact with carbon dioxide via van der Waals forces and also the π interaction effect. On the other hand, methane with no quadrupole moment to interact to the adsorbent, by van der Waal forces. Moreover, the amount of open metal sites on the adsorbent surface could enhance the carbon dioxide adsorption compared with the methane adsorption. These reasons contribute to the higher carbon dioxide adsorption capacity on the adsorbents.

Comparative adsorption on Al-based and functionalized Al-based MOFs, MIL-53(Al)-NH_2 shows weakly adsorbed methane and carbon dioxide uptakes, which are much lower than those on MIL-53(Al). This is due to the different surface areas. The adsorption of methane and carbon dioxide on Zr-based and functionalized Zr-based MOFs increases with the amount of amino functionalized on organic ligand. In the case of UiO-66-NH_2 25%, it is the only adsorbent that has methane and carbon dioxide adsorption as same as UiO-66-NH_2. Thus, UiO-66-NH_2 25% is the suitable adsorbent for methane and carbon dioxide adsorption. It can be seen that methane and carbon dioxide adsorption also prefers high surface area, high porosity, and functionalized organic linker to increase the interaction on both gas molecules.

CHAPTER V
CONCLUSIONS AND RECOMMENDATIONS

5.1 Conclusions

The methane and carbon dioxide adsorption on UiO-66, UiO-66-NH_2 25%, UiO-66-NH_2 50%, UiO-66-NH_2 75%, UiO-66-NH_2, MIL-53(Al), and MIL-53(Al)-NH_2 at 33 °C and up to 100 psi was studied. The effects of the addition of amino group on the organic ligand with UiO-66 and MIL-53(Al) were also investigated. All adsorbents adsorbed higher carbon dioxide than methane. MIL-53(Al) had the highest methane adsorption followed by UiO-66-NH_2, UiO-66-NH_2 25%, UiO-66-NH_2 75%, UiO-66-NH_2 50%, UiO-66, and MIL-53(Al)-NH_2. The results showed that not only was the surface area, micropore volume, and the open metal site important for the methane adsorption, but also the addition of amino functionalized on organic ligand. The carbon dioxide adsorption was also governed by the surface area, micropore volume, amino-functionalized linker, and open metal site. Similar results in the methane adsorption, MIL-53(Al) also has the highest carbon dioxide adsorption followed by UiO-66-NH_2, UiO-66-NH_2 25%, UiO-66-NH_2 75%, UiO-66-NH_2 50%, UiO-66, and MIL-53(Al)-NH_2. In summary, the appropriate adsorbent with the suitable physical and chemical properties such as high surface area, high micropore volume, narrow average pore size, proper open metal site, and functionalized organic linker played important roles for more methane and carbon dioxide adsorption.

5.2 Recommendations

5.2.1 Different organic ligands with various metal organic frameworks should be studied to increase the methane adsorption and carbon dioxide adsorption.

5.2.2 The methane and carbon dioxide adsorption on Al-based and Zr-based MOFs should be studied on the dynamic process.

REFERENCES

Abid, H.R., Shang, J., Ang, H-ming., and Wang, S. (2013) Amino-functionalized Zr-MOF nanoparticles for adsorption of CO_2 and CH_4. International Journal of Smart and Nano Materials 4(1), 72-82.

Ayawei, N., Ebelegi, A. N., and Wankasi, D. (2017) Modelling and Interpretation of Adsorption Isotherms. Journal of Chemistry, 1-11.

Bagheri, N., and Abedi, J. (2011) Adsorption of methane on corn cobs based activated carbon. Chemical Engineering Research and Design 89(10), 2038-2043.

Bansal, C.R., and Goyal, M. (2005) Chapter 1-activated carbon and its surface structure. Activated Carbon Adsorption, 1-65.

Beckner, M., and Dailly, A. (2016) A pilot study of activated carbon and metal-organic frameworks for methane storage. Applied Energy 162, 506-514.

Binh, N.T., Thang, H.V., Chen, X.Y., Rodrigue D., and Kaliaguine, S. (2015) Polymer functionalization to enhance interface quality of mixed matrix membranes for high CO_2/CH_4 gas separation. Journal of Materials Chemistry A. 3, 15202-15213.

Blanco, A.A.G., Vallone, A.F., Korili, S.A., Gil, A., and Sapag, K. (2016) A comparative study of several microporous materials to store methane by adsorption. Microporous and Mesoporous Materials 224, 323-331.

Boutin, A., Coudert, F.X., Huet, M.A.S., Neimark, A.V., Ferey, G., and Fuchs, A.H. (2010) The behavior of flexible MIL-53(Al) upon CH_4 and CO_2 adsorption. Journal of Physical Chemistry C. 114, 22237-22244.

Canepa, P., Arter, C.A., Conwill, E.M., Johnson, D.H., Shoemaker, B.A., Soliman, K.Z., and Thonhauser, T. (2013) High-throughput screening of small-molecule adsorption in MOF. Journal of Materials Chemistry A. 1, 13597-13604

Cao, Y., Zhao, Y., Lv, Z., Song, F., and Zhong, Q. (2015) Preparation and enhanced CO_2 adsorption capacity of UiO-66/graphene oxide composites. Journal of Industrial and Engineering Chemistry 27, 102-107.

Cavka, J.H., Jakobsen, S., Olsbye, U., Guillou, N., Lamberti, C., Bordiga, S., and Lillerud, K.P. (2008) A new zirconium inorganic building brick forming

metal organic frameworks with exceptional stability. Journal of American Chemical Society 130, 13850–13851.

Chen, L., Cao, F., and Sun, H. (2013) Ab initio study of the p–p interactions between CO_2 and benzene, pyridine, and pyrrole. International Journal of Quantum Chemistry 113, 2261–2266.

Chen, S.Q., Wegrzyn, J., and Prasad, V. (2004) Analysis of temperature and pressure changes in liquefied natural gas (LNG) cryogenic tanks. Cryogenic 44, 701-709.

Chen, Y., Zhang, F., Wang, Y., Tang, C., Yang, J., and Li, J. (2018) Recyclable ammonia uptake of a MIL series of metal-organic frameworks with high structural stability. Microporous and Mesoporous Materials 258, 170-177.

Curran, S.J., Wagner, R.M., Graves, R.L., Keller, M., and Green, J.B. (2014) Well to-wheel analysis of direct and indirect use of natural gas in passenger vehicles. Energy 75, 194-203.

Demirbas, A. (2002) Fuel Properties of Hydrogen, Liquefied Petroleum Gas (LPG), and Compressed Natural Gas (CNG) for Transportation. Energy Sources 24 (7), 601-610.

Demirbas, A. (2010) Methane Gas Hydrate. Green Energy and Technology, 57-75.

Djeridi, W., Mansour, B.N., Ouederni, A., Llewellyn, P.L., and El Mir, L. (2017) Study of methane and carbon dioxide adsorption capacity by synthetic nanoporous carbon based on pyrogallol-formaldehyde. International Journal of Hydrogen Energy 42(13), 8905-8913.

Dong, X.D., Thang, H. V., and Kaliaguine, S. (2011) MIL-53(Al) mesostructured metal-organic frameworks. Microporous and Mesoporous Materials 141, 135-139.

Donohue, M.D. and Aranovich, G.L. (1998) Classification of Gibbs adsorption isotherms. Advances in Colloid and Interface Science 76-77, 137-152.

Fletcher, A.J., Yüzak, Y., and Thomas, K.M. (2006) Adsorption and desorption kinetics for hydrophilic and hydrophobic vapors on activated carbon. Carbon 44(5), 989-1004.

Hao, S., Wen, J., Yu, X., and Chu, W. (2013) Effect of the surface oxygen groups on methane adsorption on coals. Applied Surface Science 264, 433-442.

Jeong, Y., Fan, M., Singh, S., Chuang, C.-L., Saha, B., and Hans van Leeuwen, J. (2007) Evaluation of iron oxide and aluminum oxide as potential arsenic(V) adsorbents. Chemical Engineering and Processing: Process Intensification 46(10), 1030-1039.

Jiao, Y., Li, Z., Ma, Y., Zhou, G., and Lu, G. (2017) The studies on gas adsorption properties of MIL-53 series MOFs materials. AIP Advances 7, 1-9.

Kandiah, M., Nilsen, M.H., Usseglio, S., Jakobsen, S., Olsbye, U., Tilset, M., Larabi, C., Quadrelli, E.A., Bonino, F., and Lilerud, K.P. (2010) Synthesis and stability of tagged UiO-66 Zr-MOF. Chemistry Materials 22, 6632–6640.

Kim, J., Kim, Y.W, and Ahn, W.-S. (2012) Amine-functionalized MIL-53(Al) for CO_2/N_2 separation: Effect of textural properties. Fuel 102, 574-579.

Kumar, A. (2011) Adsorption of methane activated carbon by volumetric method. National Institute of Technology.

Kumar, P., Deep, A., and Kim, K.-H. (2015) Metal organic frameworks for sensing applications. TrAC Trends in Analytical Chemistry 73, 39-53.

Li, B., Wen, H.-M., Zhou, W., Xu, Jeff Q., and Chen, B. (2016) Porous Metal organic frameworks: promising materials for methane storage. Chemistry 1(4), 557-580.

Liu, Y., Liu, J., Chang, M., and Zheng, C. (2012) Theoretical studies of CO_2 adsorption mechanism on linkers of metal–organic frameworks. Fuel 95, 521-527.

Liu, J., Wei, Y., and Zhao, Y. (2019) Trace carbon dioxide capture by metal-organic frameworks for methane storage. ACS sustainable chemistry & engineering 7, 82-93.

Lozano-Castelló, D., Alcañiz-Monge, J., de la Casa-Lillo, M.A., Cazorla-Amorós, D., and Linares-Solano, A. (2002) Advances in the study of methane storage in porous carbonaceous materials. Fuel 81(14), 1777-1803.

Luu, C., Nguyen, T., and Hoang, T. (2015) Synthesis, Characterization and adsorption ability of UiO-6-NH2. Advances in Natural Sciences: Nanoscience and Nanotechnology, 1-6.

Mao, Z. and Sinnott, S. B. (2001) Separation of Organic Molecular Mixtures in Carbon Nanotubes and Bundles: Molecular Dynamics Simulations. Journal of Physics and Chemistry 105, 6916-6924.

Mason, A.J., Veenstra, M., and Long, J., R. (2014) Evaluating metal–organic frameworks for natural gas. Chemicals Science 5, 32-51.

Martinez, F, Orcajo, G., Briones, D., Leo, P., and Calleja, G. (2017) Catalytic advantages of NH_2-modified MIL-53(Al) materials for Knoevenagel condensation reaction. Microporous and Mesoporous Materials 246, 43-50.

Meng, L and Park, S. (2012) Investigation of narrow pore size distribution on carbon dioxide capture of nanoporous carbons. Bulletin of the Korean Chemical Society 33(11), 3749-3754.

Middleton, R.A., and Eccles, J.K. (2013) The complex future of CO_2 capture and storage: Variable electricity generation and fossil fuel power. Applied Energy 108, 66-73.

Mota, J.P.A., Martins, D., Lopes, D., Catarino, I., and Bonfait, G. (2017) Structural Transitions in the MIL-53(Al) Metal–Organic Framework upon Cryogenic Hydrogen Adsorption. Journal of Physics and Chemistry 121(43), 24253-24263.

Mosher, K., He, J., Liu, Y., Rupp, E., and Wilcox, J. (2013) Molecular simulation of methane adsorption in micro- and mesoporous carbons with applications to coal and gas shale systems. International Journal of Coal Geology 109-110, 36-44.

Nawrocki, J., Rigney, M.P., McCormik, A., and Carr, P.W. (1993) Chemistry of zirconia and its use in chromatography. Journal of Chromatography A. 657, 229–282.

Nicholson, D. and Gubbins, K. E. (1996) Separation of carbon dioxide-methane mixtures by adsorption: Effects of geometry and energetics on selectivity. The Journal of chemical physics 104(20), 8126-8134.

Rada, Z.H., Abid, H.R., Shang, J., He, Y., Webley, P., Liu, S., Sun, H., and Wang, S. (2015) Effects of amino functionality on uptake of CO_2, CH_4 and selectivity of CO_2/CH_4 on titanium based MOFs. Fuel 160, 318-327.

Rada, Z.H., Abid, H.R., Sun, H., Shang, J., Li, J., He, Y., Liu, S., and Wang, S. (2018) Effects of $-NO_2$ and $-NH_2$ functional groups in mixed-linker Zr-based MOFs on gas adsorption of CO_2 and CH_4. Progress in Natural Science: Materials International 28, 160-167.

Shan, Y., Guan, D., Liu, J., Mi, Z., Schroeder, H., Cai, B., Chen. Y., Shao, S., and Zhang, Q. (2017) Methodology and applications of city level CO_2 emission accounts in China. Journal of Cleaner Productions 161, 1215-1225.

Shen, J., Sulkowski, J., Beckner, M., and Dailly, A. (2015) Effects of textural and surface characteristics of metal-organic frameworks on the methane adsorption for natural gas vehicular application. Microporous and Mesoporous Materials 212, 80-90.

Silva, C.G., Luz, I., Xamena, F.X.L., Corma, A., and Garcia, H. W. (2010) stable Zr-benzenedicarboxylate metal-organic frameworks as photocatalysts for hydrogen generation. Chemistry European Journal 16, 11133–11138.

Solar, C., Garcia, A., Vallone, A., and Sapag, K. (2010) Adsorption of methane in porous materials as the basis for the storage of natural gas. Natural Gas, 978-953-307-112-971.

Sumida, K., Rogow, D.L., Mason, J.A., McDonald, T.M., Bloch, E.D., Herm, Z.R. Bae, T., and Long, J.R. (2012) Carbon dioxide capture in metal organic frameworks. Chemical Reviews 112, 724-781.

Vandenbrande, S., Verstraelen, T., Sevillano, J., Waroquier, M., and Speybroeck, V. (2017) Methane adsorption in Zr-Based MOFs: comparison and critical evaluation of force fields. The Journal of Physical Chemistry 121, 25309-25322.

Vasiliev, L.L., Kanonchik, L.E., Mishkinis, D.A., and Rabetsky, M.I. (2000). Adsorbed natural gas storage and transportation vessels. International Journal of Thermal Sciences, 39(9–11), 1047-1055.

Vermmortele, F., Ameloot, R., Vimont, A., Serre, C., and Vos, D.D. (2011) An amino-modified Zr-terephthalate metal-organic framework as an acid–base catalyst for cross-aldol condensation. Chemistry Community 47, 1521–1523.

Yan, J., Jiang, S., Ji, S., Shi, D., and Cheng, H. (2015) Metal-organic framework MIL-53(Al): synthesis, catalytic performance for the Friedel-Crafts acylation, and reaction mechanism. Chemistry 58(10), 1544-1552.

Yang, Q., Jobic, H., Salles, F., Kolokolov, D., Guilerm, V., Serre, C. and Maurin, G. (2011) Probing the dynamics of CO_2 and CH_4 within the porous zirconium terephthalate UiO-66(Zr). Chemistry Europuen Journal 17, 8882-8889.

Yeon, S.H., Knoke, I., Gogotsi, Y., and Fisher, J.E. (2010) Enhanced volumetric hydrogen and methane storage capacity of monolithic carbide-derived carbon Microporous and Mesoporous Materials 131, 423-428.

Zakaria, Z., and George, T. (2011) The performance of commercial activated carbon adsorbent for adsorbed natural gas storage. International Journal of Recent Research and Applied Studies 9(2), 225-230.

Zheng, Z., Li, Q., Yuan, C., Tao, Q., Zhao, Y., Zhang, G., Liu, J., and Qi, G. (2018) The Thermodynamic analysis of high-pressure methane adsorption on coal-based activated carbon. Fuel 230, 172-184.

The Editors of Encyclopaedia Britannica. Adsorption Surface Phenomenon. www.britannica.com/science/adsorption, last visited on 15 July 2018.

International Energy Agency. World Energy Outlook 2016. www.eia.gov/outlooks/ieo/pdf/nat_gas, last visited on 25 June 2018.

International Energy Agency. World Energy Outlook 2018. www.eia.gov/outlooks/ieo/, last visited on 20 June 2018.

Kavalov, B. (2011). Techno-economic analysis of natural gas application as an energy source for road transport in the EU. www.edis.sk/ekes/eur21last, last visited on 1 June 2017.

Red & White International Industrial Chemicals Suppliers. www.redwhitechem.com /activated-carbon-manufacturers, last visited on 1 June 2018.

U.S. Energy information administration. International Energy Outlook 1998. www.eia.gov/outlooks/ieo/, last visited on 1 June 2018.

U.S. Energy information administration. Natural gas explain. www.eia.gov/energy explained/?page=natural_gas_home, last visited on 1 June 2018.

Union Gas. About Natural Gas. https://www.uniongas.com/about-us/about-natural-gas, last visited on 1 June 2018.

APPENDICES

Appendix A Dubinin-Astakhov (DA) pore size distribution

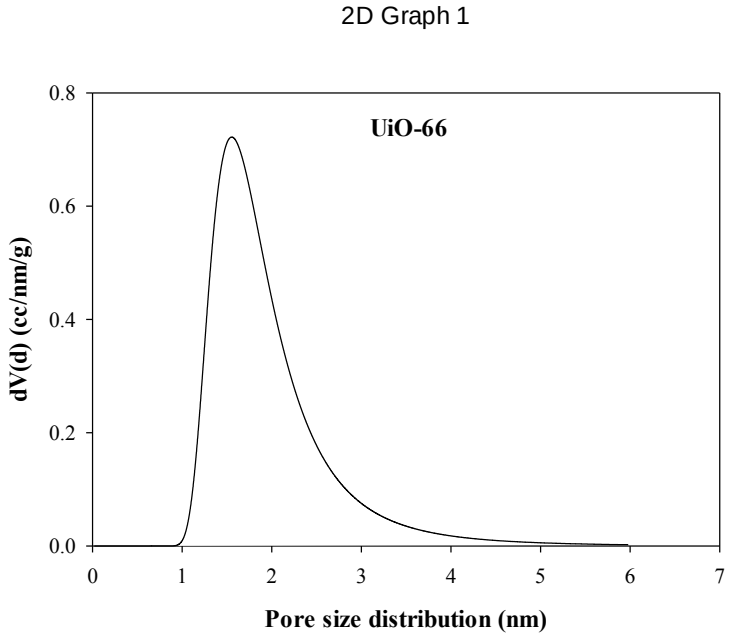

Figure A1 Micropore size distribution of UiO-66.

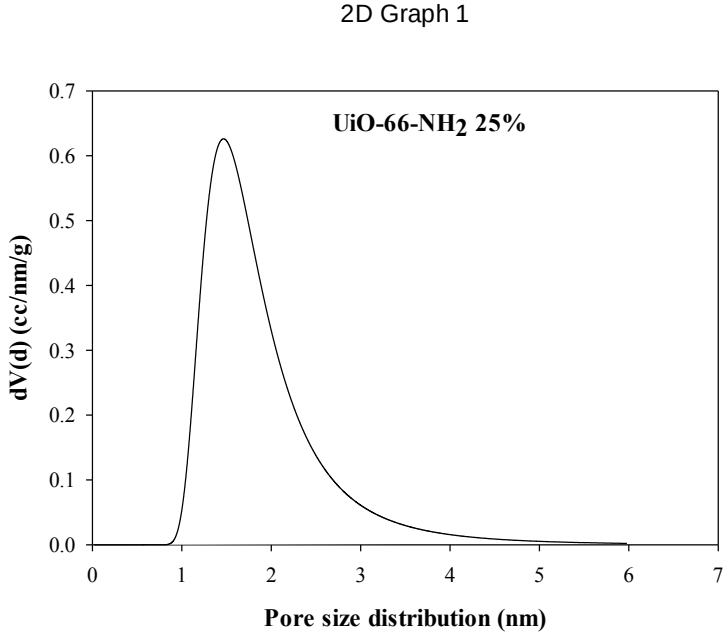

Figure A2 Micropore size distribution of UiO-66-NH_2 25%.

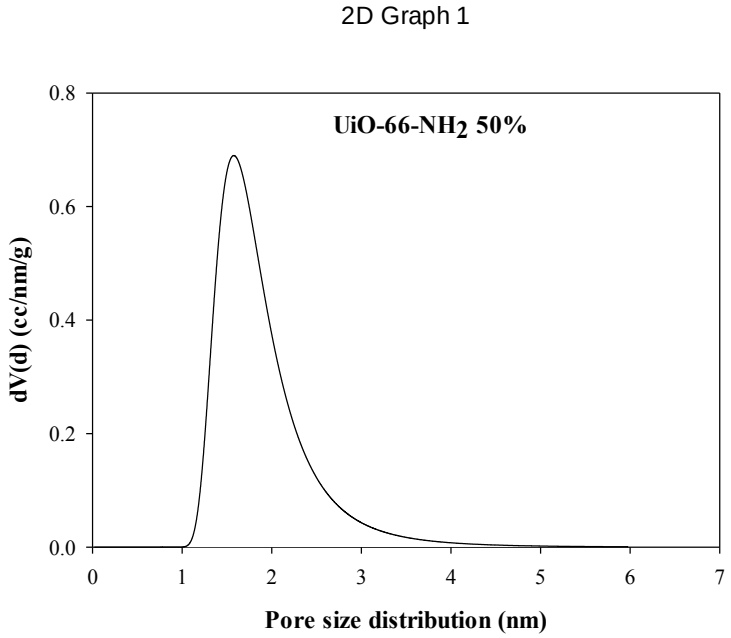

Figure A3 Micropore size distribution of UiO-66-NH_2 50%.

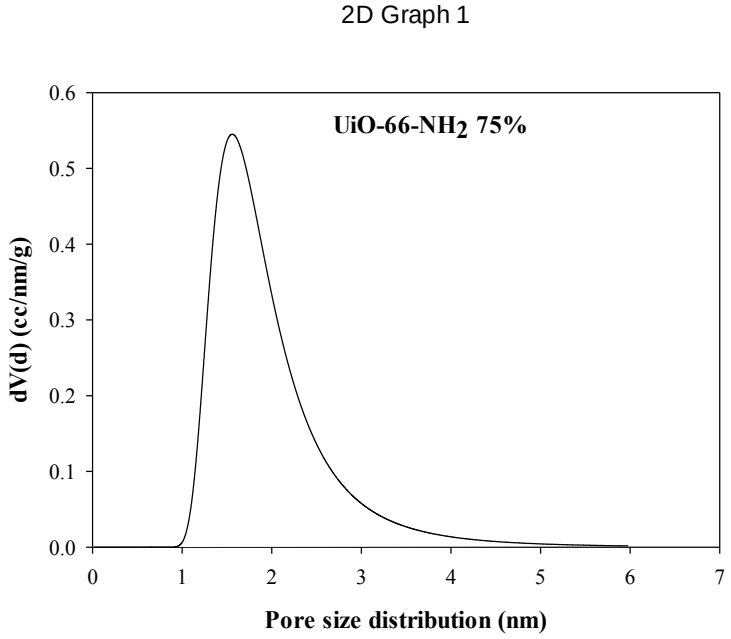

Figure A4 Micropore size distribution of UiO-66-NH_2 75%.

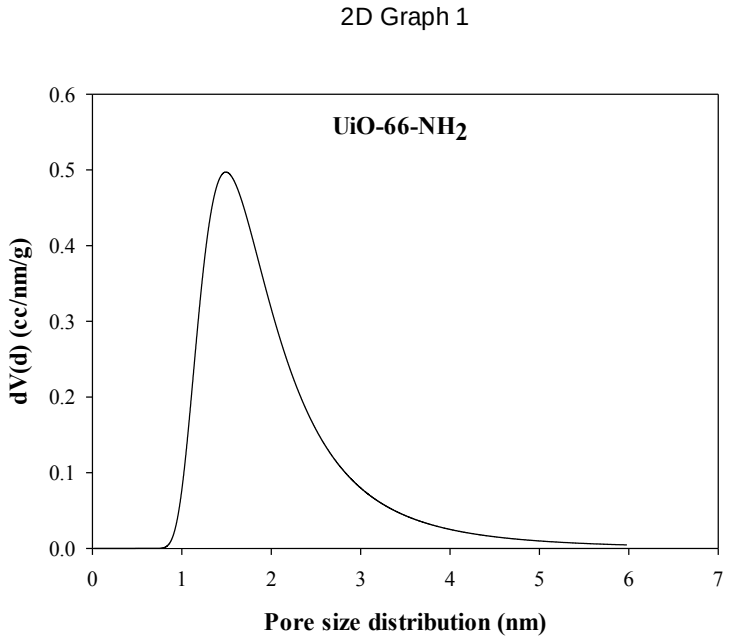

Figure A5 Micropore size distribution of UiO-66-NH_2.

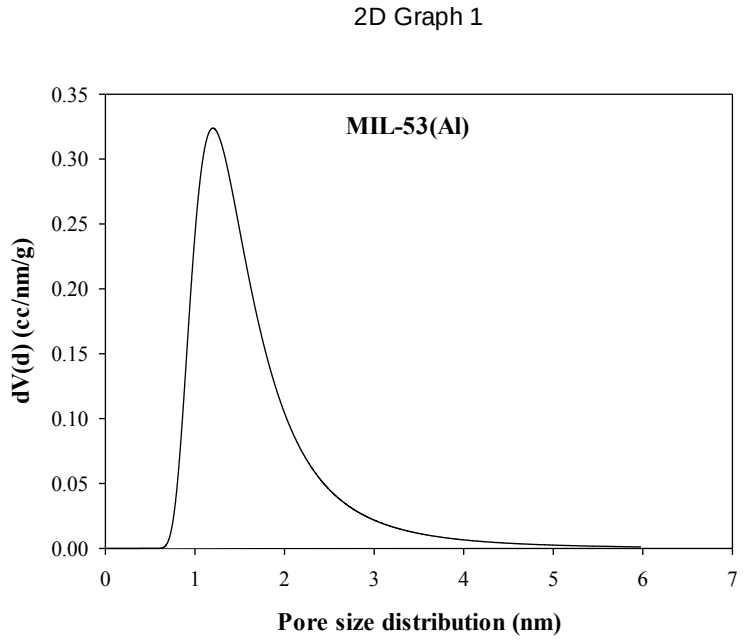

Figure A6 Micropore size distribution of MIL-53(Al).

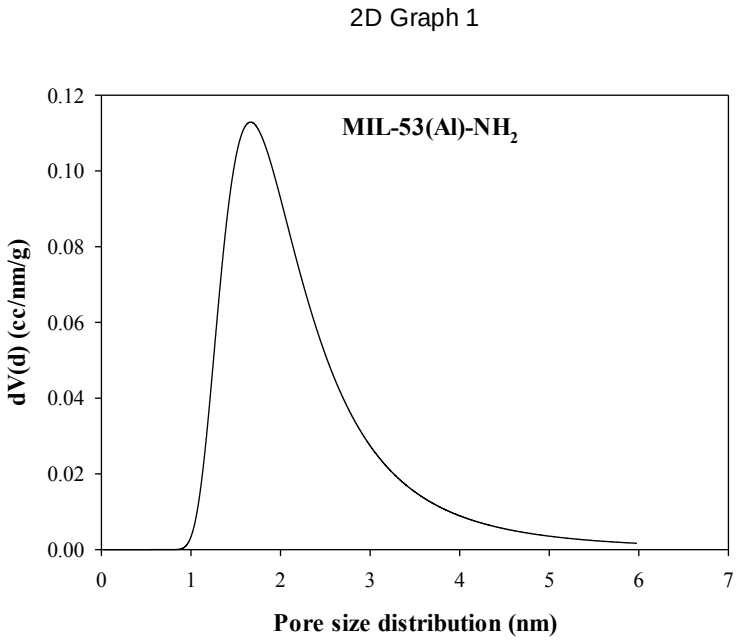

Figure A7 Micropore size distribution of MIL-53(Al)-NH_2.

Appendix B Methane Adsorption on Different Adsorbents at 33 °C

Table B1 The amount of methane adsorption capacity on UiO-66

Equilibrium pressure (psia)	Methane adsorption (mmol/g)	Langmuir (mmol/g)	Freundilch (mmol/g)	Sips (mmol/g)
13.00	0.00	0.13	0.06	0.02
21.82	0.09	0.21	0.12	0.07
34.76	0.18	0.34	0.23	0.19
45.45	0.33	0.44	0.34	0.32
56.48	0.48	0.55	0.46	0.48
67.10	0.62	0.65	0.59	0.63
76.63	0.75	0.74	0.72	0.76
86.73	0.89	0.84	0.86	0.89
97.57	1.02	0.94	1.01	1.01
107.35	1.10	1.04	1.16	1.11

Table B2 The amount of methane adsorption capacity on UiO-66-NH_2 25%

Equilibrium pressure (psia)	Methane adsorption (mmol/g)	Langmuir (mmol/g)	Freundilch (mmol/g)	Sips (mmol/g)
13.00	0.00	0.20	0.19	0.12
20.44	0.30	0.31	0.30	0.24
34.07	0.52	0.50	0.49	0.48
45.13	0.68	0.66	0.65	0.67
56.01	0.83	0.81	0.80	0.85
66.07	0.97	0.95	0.93	0.99
76.51	1.10	1.09	1.08	1.12
86.51	1.23	1.22	1.21	1.23
96.44	1.34	1.34	1.35	1.33
106.51	1.43	1.47	1.49	1.42

Table B3 The amount of methane adsorption capacity on UiO-66-NH_2 50%

Equilibrium pressure (psia)	Methane adsorption (mmol/g)	Langmuir (mmol/g)	Freundilch (mmol/g)	Sips (mmol/g)
13.00	0.00	0.14	0.08	0.06
20.36	0.14	0.21	0.15	0.12
34.54	0.29	0.36	0.29	0.27
45.76	0.43	0.48	0.41	0.41
56.34	0.54	0.59	0.54	0.55
66.41	0.67	0.70	0.66	0.68
76.48	0.78	0.80	0.79	0.81
86.34	0.94	0.91	0.92	0.93
96.54	1.08	1.01	1.06	1.06
106.47	1.15	1.12	1.20	1.17

Table B4 The amount of methane adsorption capacity on UiO-66-NH_2 75%

Equilibrium pressure (psia)	Methane adsorption (mmol/g)	Langmuir (mmol/g)	Freundilch (mmol/g)	Sips (mmol/g)
13.00	0.00	0.16	0.15	0.10
20.36	0.24	0.25	0.24	0.19
34.54	0.43	0.42	0.41	0.40
45.76	0.57	0.55	0.54	0.56
56.29	0.68	0.67	0.66	0.70
66.21	0.81	0.79	0.78	0.82
76.16	0.91	0.90	0.90	0.93
86.29	1.02	1.02	1.02	1.03
96.54	1.12	1.13	1.14	1.12
106.53	1.22	1.24	1.26	1.20

Table B5 The amount of methane adsorption capacity on UiO-66-NH_2

Equilibrium pressure (psia)	Methane adsorption (mmol/g)	Langmuir (mmol/g)	Freundilch (mmol/g)	Sips (mmol/g)
13.00	0.00	0.27	0.29	0.18
19.17	0.43	0.38	0.39	0.31
33.51	0.66	0.62	0.61	0.62
45.57	0.84	0.80	0.78	0.84
56.07	0.97	0.94	0.91	0.99
66.10	1.09	1.07	1.04	1.11
76.41	1.20	1.18	1.17	1.22
86.79	1.29	1.29	1.29	1.30
96.79	1.34	1.39	1.41	1.36
106.32	1.47	1.48	1.52	1.42

Table B6 The amount of methane adsorption capacity on MIL-53(Al)

Equilibrium pressure (psia)	Methane adsorption (mmol/g)	Langmuir (mmol/g)	Freundilch (mmol/g)	Sips (mmol/g)
13.00	0.00	0.21	0.21	0.14
20.10	0.33	0.32	0.32	0.26
34.07	0.56	0.54	0.52	0.52
45.60	0.74	0.70	0.69	0.72
56.23	0.88	0.85	0.84	0.90
66.45	1.02	0.99	0.98	1.04
76.73	1.15	1.13	1.12	1.17
86.70	1.26	1.26	1.26	1.28
96.42	1.38	1.38	1.39	1.37
106.51	1.48	1.50	1.52	1.45

Table B7 The amount of methane adsorption capacity on MIL-53(Al)-NH_2

Equilibrium pressure (psia)	Methane adsorption (mmol/g)	Langmuir (mmol/g)	Freundilch (mmol/g)	Sips (mmol/g)
13.00	0.00	0.11	0.11	0.08
20.48	0.19	0.16	0.16	0.14
34.26	0.28	0.27	0.26	0.26
45.92	0.36	0.35	0.34	0.35
56.76	0.42	0.42	0.41	0.43
66.92	0.48	0.48	0.47	0.50
76.85	0.54	0.54	0.53	0.55
87.10	0.61	0.60	0.60	0.60
96.76	0.65	0.65	0.66	0.64
106.79	0.69	0.70	0.72	0.68

Appendix C Carbon Dioxide Adsorption on Different Adsorbents at 33 °C

Table C1 The amount of carbon dioxide adsorption capacity on UiO-66-NH_2

Equilibrium pressure (psia)	Methane adsorption (mmol/g)	Langmuir (mmol/g)	Freundilch (mmol/g)	Sips (mmol/g)
13.00	0.00	0.17	0.05	0.01
22.76	0.08	0.30	0.13	0.06
34.95	0.17	0.46	0.27	0.20
45.45	0.37	0.60	0.41	0.37
55.85	0.60	0.73	0.58	0.58
65.51	0.80	0.86	0.75	0.80
75.42	1.01	0.99	0.94	1.01
85.35	1.20	1.12	1.16	1.21
95.32	1.38	1.25	1.39	1.39
105.01	1.56	1.38	1.63	1.54

Table C2 The amount of carbon dioxide adsorption capacity on UiO-66-NH_2 25%

Equilibrium pressure (psia)	Methane adsorption (mmol/g)	Langmuir (mmol/g)	Freundilch (mmol/g)	Sips (mmol/g)
13.00	0.00	0.35	0.35	0.24
19.10	0.54	0.51	0.50	0.40
32.85	0.88	0.85	0.83	0.81
44.95	1.19	1.14	1.12	1.16
55.82	1.44	1.40	1.37	1.45
65.95	1.66	1.63	1.61	1.69
76.14	1.87	1.86	1.84	1.91
86.07	2.08	2.07	2.07	2.10
96.45	2.27	2.29	2.30	2.27
106.13	2.45	2.48	2.52	2.41

Table C3 The amount of carbon dioxide adsorption capacity on UiO-66-NH_2 50%

Equilibrium pressure (psia)	Methane adsorption (mmol/g)	Langmuir (mmol/g)	Freundilch (mmol/g)	Sips (mmol/g)
13.00	0.00	0.21	0.21	0.16
19.52	0.40	0.32	0.31	0.27
34.27	0.57	0.56	0.55	0.54
45.41	0.73	0.74	0.73	0.74
56.01	0.92	0.90	0.90	0.92
66.14	1.08	1.06	1.06	1.09
76.03	1.23	1.22	1.21	1.24
85.86	1.37	1.37	1.37	1.38
96.16	1.50	1.52	1.53	1.52
106.04	1.67	1.67	1.69	1.64

Table C4 The amount of carbon dioxide adsorption capacity on UiO-66-NH_2 75%

Equilibrium pressure (psia)	Methane adsorption (mmol/g)	Langmuir (mmol/g)	Freundilch (mmol/g)	Sips (mmol/g)
13.00	0.00	0.31	0.31	0.22
19.45	0.50	0.46	0.46	0.38
33.39	0.82	0.78	0.77	0.75
44.98	1.08	1.04	1.02	1.05
55.60	1.30	1.26	1.24	1.31
65.82	1.49	1.48	1.46	1.53
76.10	1.69	1.68	1.67	1.73
86.10	1.88	1.88	1.88	1.90
96.07	2.07	2.07	2.09	2.06
106.20	2.24	2.26	2.29	2.20

Table C5 The amount of carbon dioxide adsorption capacity on UiO-66-NH_2

Equilibrium pressure (psia)	Methane adsorption (mmol/g)	Langmuir (mmol/g)	Freundilch (mmol/g)	Sips (mmol/g)
13.00	0.00	0.34	0.30	0.22
18.88	0.52	0.50	0.45	0.37
32.98	0.85	0.87	0.82	0.78
44.88	1.13	1.19	1.14	1.15
55.01	1.46	1.45	1.41	1.46
65.60	1.73	1.73	1.71	1.77
75.80	2.02	2.00	1.99	2.05
85.32	2.34	2.25	2.26	2.29
95.85	2.55	2.53	2.56	2.55
105.76	2.77	2.79	2.85	2.77

Table C6 The amount of carbon dioxide adsorption capacity on MIL-53(Al)

Equilibrium pressure (psia)	Methane adsorption (mmol/g)	Langmuir (mmol/g)	Freundilch (mmol/g)	Sips (mmol/g)
13.00	0.00	0.65	0.71	0.41
16.51	0.88	0.80	0.83	0.60
30.51	1.45	1.31	1.27	1.34
43.17	1.83	1.69	1.61	1.84
54.57	2.09	1.98	1.89	2.14
65.48	2.26	2.22	2.14	2.35
75.82	2.43	2.42	2.37	2.48
86.13	2.58	2.59	2.59	2.59
96.23	2.70	2.75	2.79	2.66
106.32	2.81	2.89	2.99	2.72

Table C7 The amount of carbon dioxide adsorption capacity on MIL-53(Al)-NH_2

Equilibrium pressure (psia)	Methane adsorption (mmol/g)	Langmuir (mmol/g)	Freundilch (mmol/g)	Sips (mmol/g)
13.00	0.00	0.14	0.15	0.11
19.01	0.25	0.20	0.21	0.18
32.60	0.37	0.33	0.33	0.33
44.82	0.46	0.44	0.43	0.45
55.69	0.54	0.54	0.53	0.55
66.26	0.63	0.62	0.61	0.64
76.39	0.69	0.70	0.69	0.71
86.48	0.77	0.78	0.77	0.78
96.42	0.84	0.85	0.85	0.84
106.42	0.92	0.91	0.93	0.89

Appendix D Methane and Carbon dioxide Adsorption on Different Adsorbents VS BET Surface Area at 33 °C

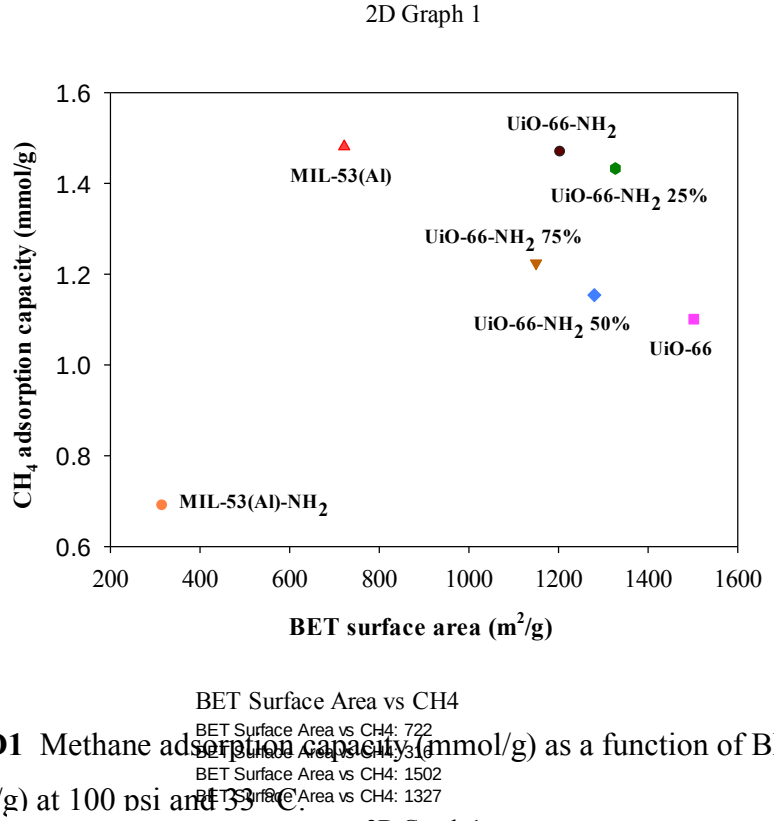

Figure D1 Methane adsorption capacity (mmol/g) as a function of BET surface area (m^2/g) at 100 psi and 33 °C.

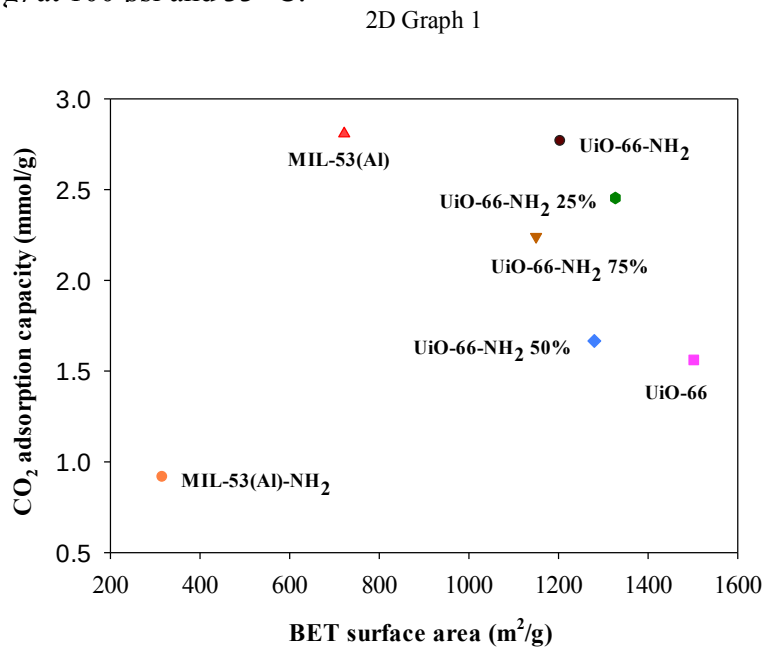

Figure D2 Carbon dioxide adsorption capacity (mmol/g) as a function of BET surface area (m^2/g) at 100 psi and 33 °C.

Appendix E Methane and Carbon dioxide Adsorption on Different Adsorbents VS Micropore Volume at 33 °C

2D Graph 1

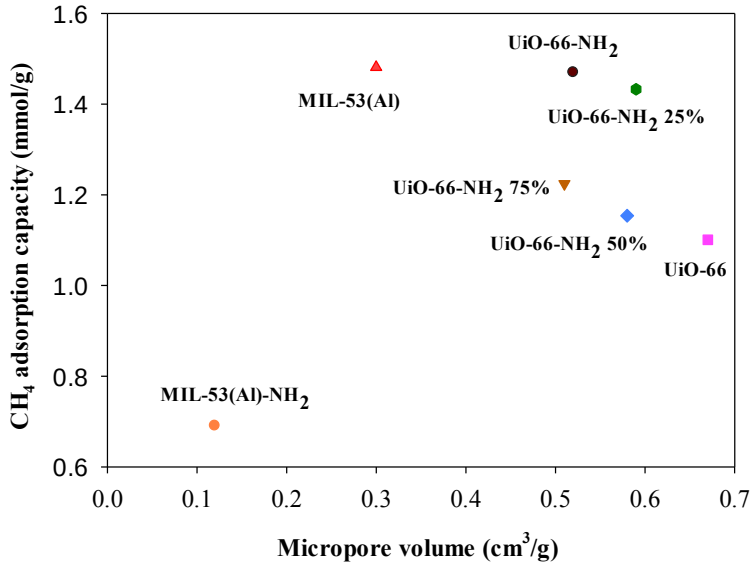

Micropore vs CH4
Micropore vs CH4: 0.3
Micropore vs CH4: 0.12
Micropore vs CH4: 0.67
Micropore vs CH4: 0.59

Figure E1 Methane adsorption capacity (mmol/g) as a function of micropore volume (cm^3/g) at 100 psi and 33 °C

2D Graph 1

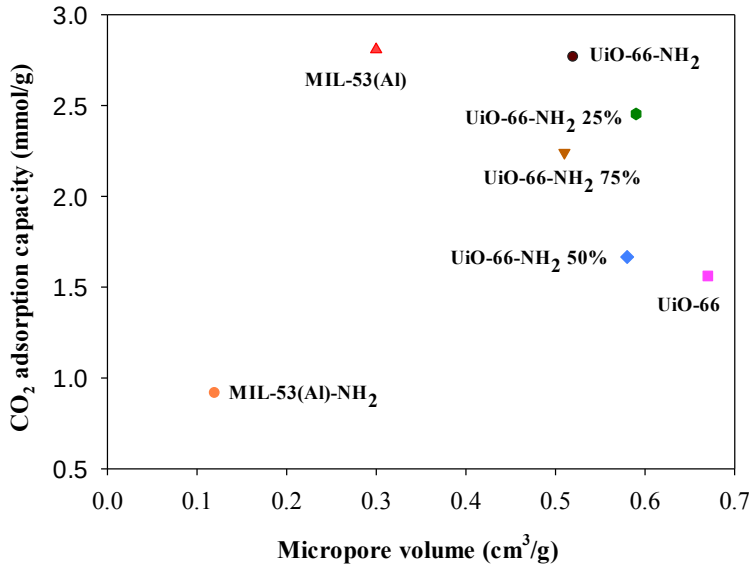

Micropore vs CO2: 0.3
Micropore vs CO2: 0.12
Micropore vs CO2: 0.67
Micropore vs CO2: 0.59
Micropore vs CO2: 0.58
Micropore vs CO2: 0.51
Micropore vs CO2: 0.52

Figure E2 Carbon dioxide adsorption capacity (mmol/g) as a function of micropore volume (cm^3/g) at 100 psi and 33 °C

CURRICULUM VITAE

Name: Ms. Orawee Lamoonkit

Date of Birth: September 13, 1992

Nationality: Thai

University Education:

2013–2017 Chulalongkorn University, Faculty of Science, Department of Chemical Technology, Bangkok, Thailand

Work Experience:

2016-2016 Position: Technical Trainee
Company name: TSCL PTT Global Chemical Public Company Limited, Thailand

Presentations:

1. Lamoonkit, O., Kulpratipunja, S., Ratanatawanate, C., Rangsunvigit, P. (2019, July 24-26) Effects of amino functionalization on Zr-based MOFs for methane and carbon dioxide adsorption. Poster Presentation at The 19th International Conference on Green Energy and Environmental Technology, Paris, France.
2. Lamoonkit, O., Kulpratipunja, S., Ratanatawanate, C., Rangsunvigit, P. (2019, May 30) Methane and Carbon Dioxide on Aluminium Based MOFs and Zirconium Based MOFs. Proceeding at The 25th PPC Symposium on Petroleum, Petrochemicals, and Polymers and The 10th Research Symposium on Petrochemical and Materials Technology, Bangkok, Thailand.
3. Lamoonkit, O., Kulpratipunja, S., Ratanatawanate, C., Rangsunvigit, P. (2018, November 8-9) Synthesis of UiO-66 (Zr) and Its Adsorption on Methane and Carbon Dioxide. Poster Presentation at The 8th International TIChE Conference, Pattaya, Thailand.